Metal Halide Perovskites: Photophysics and Inkjet Printing of Solar Cells

Dissertation

zur Erlangung des akademischen Grades

Doctor rerum naturalium

(Dr. rer. nat.)

im Fach Physik eingereicht an der

Mathematisch-Naturwissenschaftlichen Fakultät

der Humboldt-Universität zu Berlin

von

Herr M.Sc. Edgar Ricardo Nandayapa Bermúdez

Präsidentin der Humboldt-Universität zu Berlin

Prof. Dr.-Ing. Dr. Sabine Kunst

Dekan der Mathematisch-Naturwissenschaftlichen Fakultät

Prof. Dr. Elmar Kulke

Gutachter/in: 1. Prof. Dr. Emil List-Kratochvil

2. Dr. Eva Unger

3. Prof. Dr. Aldo Di Carlo

Datum der Einreichung: 15.01.2021

Datum der Promotion: 08.04.2021

Declaration

Hiermit erkläre ich, die Dissertation selbstständig und nur unter Verwendung der angegebenen Hilfen und Hilfsmittel angefertigt zu haben. Ich habe mich nicht anderwärts um einen Doktorgrad in dem Promotionsfach beworben und besitze keinen entsprechenden Doktorgrad. Die Promotionsordnung der Mathematisch-Naturwissenschaftlichen Fakultät, veröffentlicht im Amtlichen Mitteilungsblatt der Humboldt-Universität zu Berlin Nr. 42 am 11. Juli 2018, habe ich zur Kenntnis genommen.

Edgar R. Nandayapa
Berlin, 23.11.2020

Acknowledgements

The successful completion of this work has been possible thanks to the support, guidance, and motivation of various people.

First, I would like to thank Prof. Dr. Emil List-Kratochvil for his trust, constant encouragement, thoughtful supervision, and fruitful discussions. Also, for allowing me to continue and finalize my research work on his group.

Additionally, I would like to thank the Functional Devices and Materials group at Fraunhofer IAP for the support, patience, and advice during my learning process at the lab. To Christine Boeffel for first believing in me and her encouragement. To Armin Wedel for allowing me to work on his group. To Bert Fischer and Stefan Kröpke for their patience and outstanding troubleshooting skills, and together with Alexander Lange, for guiding me into the inkjet printing world. To the rest of the team: Yohan Kim, Manuel Gensler, Benjamin Heyne, Franziska Ebert, and Stefanie Voigt for their consistent support and friendship. To Andreas Bohn for his time and curiosity on perovskites.

To the members of the Hybrid Devices group at Humboldt University in Berlin for the wonderful work atmosphere. Special thanks to Bodo Kranz and Paul Zybarth for their invaluable help and dedication. I am also grateful for the guidance and friendship from Felix Hermerschmidt, Niklas Mutz, Sebastian Kickhöfel, Michael Hengge, and Vincent Schröder, as well as the support from Paul Hänsch.

From the Helmholtz Zentrum Berlin, I would like to thank Florian Mathies and Gopinath Paramasivam for the great synergy at the lab and help on designing and accomplishing the experiments successfully. Additionally, to Eva Unger for her support and Hagen Heinz for his

constant assistance. Also, to the rest of the members from the HySPRINT Innovation lab for their camaraderie.

To all the project partners from the CHEOPS project, sponsored by the European Union, and the flex!PV_2.0 project, sponsored by the FFG, for the exchange of ideas and solidarity. Also, to the mentioned entities as well as CONACYT and the Helmholtz Energy Materials Foundry for the financial support.

I would like to give special thanks to Cristiane Henschel for her invaluable help across life, this accomplishment would have been much more difficult and less fun without you.

Finally, I would like to thank my parents and brothers: Quiero dar un agradecimiento especial a mis papás; Enrique y José, por creer en mí desde el principio y apoyarme en todos mis sueños y mis hermanos Quique y Pepe por siempre estar ahí para mí.

Zusammenfassung

Metallhalogenid-Perowskite (MHPs) sind Halbleiter, die einzigartige photophysikalische Eigenschaften aufweisen, die sie ideal für photovoltaische Anwendungen machen. Techniken werden kontinuierlich entwickelt, um die Leistungsgrenzen der Perowskite weiter zu verschieben. Dennoch weisen diese Materialien verschiedene Herausforderungen auf. Zu diesen gehören eine geringe Stabilität unter einer Vielzahl von äußeren Bedingungen, sowie eine große Diskrepanz zwischen den Wirkungsgraden von Geräten im Labormaßstab und großflächigen Geräten. Die vorliegende Arbeit beleuchtet diese beiden bedeutenden Hürden.

Zunächst wurden mit Hilfe von Photolumineszenz-Spektroskopie Ladungsübertragungs-mechanismen zwischen MHPs und atmosphärischen Gasen untersucht, um deren Einfluss auf die Materialstabilität zu bestimmen. Durch den Vergleich der Emission von MHP-Einkristallen und Mehrkristallen hoher und niedriger Qualität wurde die Wirkung untersucht, die molekularer Sauerstoff, Stickstoff, Argon und Wasser auf Grenzdefekte im Material haben. Diese (Fluoreszenz)löschungseffekte wurden nachfolgend mit dem Stern-Volmer-Modell analysiert. Es stellte sich heraus, dass die Gase mehrheitlich von der Oberfläche abprallen. Ein Teil von ihnen bindet jedoch an die MHPs, wobei teilweise Kristalldefekte passiviert werden. Anhand dieser Ergebnisse wurden für jedes der Gase Ladungstransfermechanismen vorgeschlagen.

Zweitens wurde die Skalierung von MHP-Bauelementen mittels Tintenstrahldruck untersucht. Dazu wurden drei Kristallisationstechniken ausgewertet. Eine davon verwendete eine sequenzielle Abscheidung von zwei Präkursortinten, während die beiden anderen kristallisierte Tinten verwendeten, die in einem Schritt abgeschieden wurden. Die letztgenannten Techniken verwendeten beide niedrige Drücke und bei einer wurde ein kontrollierter Stickstoffstrom auf die Probe angewendet. Mit diesen Techniken wurde eine Abscheidung auf einer Fläche von 15x15 cm^2 erreicht, sowie eine Solarzelle mit einer Effizienz von 16,8% demonstriert.

Diese Ergebnisse zeigen ein neuartiges Verfahren zur Untersuchung von strahlungslosen Verlustwegen in MHPs auf, um deren Stabilität und Leistung in Bauelementen zu verbessern. Zusätzlich demonstrieren diese Studien, dass der Tintenstrahldruck eine geeignete Technologie ist, um MHP-Bauelemente zu skalieren und letztendlich die Massenproduktion von photovoltaischen Geräten dieser Art zu erleichtern.

Abstract

Metal halide perovskites (MHPs) are semiconductor materials that show unique photophysical properties, making them ideal for photovoltaic applications. Having shown power conversion efficiencies of up to 25.5%, techniques are continuously being developed to push perovskites to unprecedent limits. Yet, these materials present challenges like a low stability under a variety of conditions as well as a large disparity between the efficiencies of lab scale and large area devices. This thesis addresses these two major obstacles.

First, by using photoluminescence spectroscopy, charge transfer mechanisms between MHPs and atmospheric gases were studied to determine their effect on the material stability. By comparing the emission of MHP single crystals and polycrystals of high- and low-quality, the effect that molecular oxygen, nitrogen, argon, and water have on boundary defects in the material was studied. These quenching effects were later analyzed using the Stern-Volmer model. It was found that the gases bounce off the surface, but a portion of them bind to the MHPs, in occasions passivating defects on the crystals. Using these results, charge transfer mechanisms were proposed for each one of the gases.

Second, scaling of MHP devices was examined using inkjet printing. For this, three crystallization techniques were evaluated. One of them used a sequential deposition of two precursor inks, while the other two crystallized ink that was deposited in one step. Both latter techniques used low pressures, below 1 mbar, and only one of them applied a controlled stream of nitrogen to the sample. Using these techniques, the deposition of a 15x15 cm^2 area as well as a device with an efficiency of 16.8% on an area of 0.16 cm^2 were demonstrated.

These results show a novel procedure to study non-radiative loss paths in MHPs to enhance their stability and performance as devices. Also, they show that inkjet printing is a favorable technology to scale MHP devices and eventually facilitate the mass production of this type of photovoltaic devices.

Schlagwörter:

Perowskit, Photolumineszenz, Stern-Volmer, Tintenstrahldrucken

Keywords:

Perovskite, Photoluminescence, Stern-Volmer, Inkjet Printing

Table of Contents

List of Abbreviations

BCP	Bathocuproine
BIPV	Building Integrated Photovoltaics
CBM	Conduction Band Minimum
CCD	Charge-Coupled Device
CIGS	Copper Indium Gallium Selenide
CTL	Charge Transport Layer
DMF	Dimethylformamide
DMSO	Dimethyl Sulfoxide
DOS	Density of States
DPI	Dots per Inch
EA	Ethyl Acetate
EBSD	Electron Backscatter Diffraction
EET	Electronic Energy Transfer
EQE	External Quantum Efficiency
ETL	Electron Transport Layer
FACl	Formamidinium Chloride
FAI	Formamidinium Iodide
FET	Field Effect Transistor
FF	Fill factor
GaAs	Gallium Arsenide
GBL	γ-butyrolactone
GUI	Graphical User Interface
HD	High Definition
HTL	Hole Transport Layer
IPA	Isopropanol
IR	Infrared
Jsc	Short Circuit Current
JV	Current-Voltage
LED	Light Emitting Diode
MAI	Methylammonium Iodide
MAPI	Methylammonium Lead Iodide
MHP	Metal Halide Perovskite
MPP	Maximum Power Point
NHE	Normal Hydrogen Electrode
NMP	N-Methyl-2-pyrrolidone
NREL	National Renewable Energy Laboratory
PCE	Power Conversion Efficiency
PEDOT	Poly(3,4-ethylenedioxythiophene)
PSS	Polystyrene Sulfonate
PK	Perovskite
PL	Photoluminescence
PLQY	Photoluminescence Quantum Yield
PTAA	Poly (Triaryl Amine)
PTFE	Polytetrafluoroethylene
PV	Photovoltaic
RET	Resonance Energy Transfer
rpm	revolutions per minute
SAM	Self-assembled monolayer
SEM	Scanning Electron Microscope
SFE	Surface Free Energy
SV	Stern-Volmer
TCSPC	Time-Correlated Single Photon Counting
THC	Total hydrocarbons
TRPL	Time-Resolved Photoluminescence
UV	Ultraviolet
VBM	Valence Band Maximum
VdW	Van der Waals
Voc	Open Circuit Voltage

1 Introduction

1.1 Motivation

Current environmental problems, like overpopulation and global warming, require creative solutions to maintain the energy requirements for modern life while maintaining low carbon emissions. Generation of electric power by photovoltaic devices is a favorable generation method to meet these conditions. And although this technology has hurdles that still need to be addressed, like the mismatch of peak solar power generation and demand times, the so-called "duck curve", renewable energy sources are becoming more prevalent around the world. In the first half of 2020, 48.7% of the electric power generated in Germany came from renewable sources, of which, 9.7% of the total came from solar sources.[1] Globally, 69% of the energy supply is expected to be produce by photovoltaic devices by the year 2050.[2]

Currently, more than 90% of the market share of photovoltaics is held by silicon-based solar cells.[3] The cost per watt of this technology has shown a dramatic reduction, going from $4.00 in 2008 to less than $0.5 in 2018.[4] The efficiency and costs of silicon solar cells can be improved even further by combining them with a new type of promising materials called metal halide perovskites (MHPs).[5] MHPs show several advantages, including a high absorption coefficient, bandgap tunability, high defect tolerance, and low production costs. Additionally, while silicon solar cells have shown a record efficiency of 26.7%, MHP devices have already shown 25.5%, and as high as 29.15% in tandem with silicon solar cells.[6] These are highly efficient devices that can be deposited by solution processes, which makes them more accessible and low cost, especially when looking at techniques like inkjet printing and slot-die coating. These aspects make them an attractive complement, as well as an alternative, to the already well-established

silicon-based technology. For these reasons, companies like Oxford PV and Saule Technologies are motivated to develop products that use MHP materials for solar power generation and bring them as consumer products in the near future.

Even with all the promise shown by MHPs, there are still challenges that need to be addressed. As it is the case, the stability of these materials dwarf in comparison to their silicon counterparts. While silicon solar cells have an estimated lifetime of 25 years, MHPs have been shown to last no longer than 6 months under the same standards.[7] Additionally, there is a disparity in efficiencies between lab scale and large scales. An MHP device with area of 0.09 cm^2 showed an efficiency of 25.5%, while a larger area of 1 cm^2 showed a maximum 20.3% by spin coating and 12.3% by inkjet printing.[8,9]

1.2 Outline

In this thesis, the challenges of stability and scalability will be addressed. First, processes that reduce the efficiency of MHP devices by charge transfer mechanisms to other molecules will be revealed. Specifically, the reduction of photoluminescence due to charge transfer losses to atmospheric gases. Second, strategies to deposit MHPs by inkjet printing in areas larger than lab scale, 1x1 in^2, will be developed. To accomplish this, the thesis is divided in two main segments, one that introduces the concepts and materials used in the experiments, and a second focused on the experimental results.

In **Chapter 2**, the fundamental concepts needed to understand the topics covered throughout the thesis will be described. First, general information about metal halide perovskites is presented, focusing on their crystal structure and essential properties. Then, the physical properties of solar cells are discussed: from the generation and recombination of charges, to different junction types and other key performance parameters. Later, the fundamentals of photoluminescence are discussed. Starting with the phenomenon of absorption and emission, to relevant photophysical properties like quantum yield and lifetime. Then, the Stern-Volmer model is explained. Here, the changes of photoluminescence intensity of the material are analyzed in the presence of other molecules. Finally, the fundamentals of inkjet printing are

discussed, focusing on the different types of inkjet printing and the relevant physical parameters involved during the printing process.

In **Chapter 3**, the quenching effects of atmospheric gases on MHP layers are explored. Their energy transfer mechanisms are identified using photoluminescence spectroscopy. These atmospheric gases were molecular oxygen, molecular nitrogen, argon, and water in the form of water-enriched argon. The effect is measured by tracking the change of photoluminescence emission and photoluminescence lifetime of MHP layers at different concentrations of the gases. The quality of the MHP crystals was determined using photoluminescence quantum yield. Finally, the data was analyzed with the Stern-Volmer model and the results were used to quantify the energy transfer efficacy and mechanisms for each one of the molecules. Additionally, the Stern-Volmer model is displayed as a useful tool to evaluate the passivation effects of ions and molecules used to increase the stability of MHP devices.

In **Chapter 4**, inkjet printing was used to investigate upscaling pathways of high quality MHP layers. Three different techniques to crystalize the perovskite inks were evaluated. The first one combined the deposition of two inkjet-printed layers to promote the crystal formation of MHPs. The second and third techniques required a single inkjet deposition of a perovskite ink and differed on the way that crystallization was enhanced. For instance, the second method was done on a large chamber with a volume of 22 L and induced the crystallization of the ink through low pressures. The third technique used a small chamber of 0.25 L and implemented a constant stream of nitrogen at low pressures to crystallize the layers. The chamber used in the third technique also contained a quartz glass from which in-situ measurements exposed new aspects of the crystallization process.

Chapter 5 contains a general conclusion and outlook of the results discussed on the experimental segment of this thesis. **Chapter 6** contains the list of all references used and **Chapter 7** contains appendixes and other supportive information to the main text.

2 Fundamentals

In this chapter, the fundamentals of the topics covered throughout the thesis will be discussed. The goal is to present the reader with all the information needed to follow the contents of this thesis. First, metal halide perovskites (MHPs) – the material used for the experiments – will be put into context as a crystal with unique characteristics and properties. Then, the physics of solar cells is covered, focusing on the key performance characteristics of a cell. Then, the fundamentals of photoluminescence spectroscopy will be discussed, as well as the basics of the analytical model used, the Stern-Volmer model. Finally, inkjet printing will be discussed as the large area deposition technique employed in this thesis.

2.1 Metal Halide Perovskites

Perovskites are group of materials that share a crystalline structure with the mineral calcium titanium oxide ($CaTiO_3$). This section contains a brief description of what constitutes a perovskite and will describe the physical and chemical characteristics that have made of it such a popular material.

2.1.1 Brief History

Named after Lev Perovski, a Russian mineralogist, perovskites were first discovered in the Ural Mountains in the form of $CaTiO_3$ by Gustav Rose in 1839.[10] Outside of geology, this type of materials started to gain interest in the 1950s, due to the ferroelectric properties found in perovskite oxides, like $BaTiO_3$.[11] In 1958, the first MHPs with a composition of $CsPbCl_3$ and $CsPbBr_3$ were studied.[12] They were prepared via spin coating and showed photoconductive

properties. However, it was only in 1995 when the first semiconducting properties were measured by Mitzi and collaborators with $MASnI_3$.[13] In 2001, the first perovskite-based LED was demonstrated by Mitzi using the same material.[14] The first perovskite-based photovoltaic was demonstrated by Miyasaka and collaborators in 2006, using MAPbBr3 in a dye-sensitized solar cell (DSSC).[15] However, the full potential of MHPs as photovoltaic materials did not concretize until the solar cells became completely solid-state, as demonstrated by Grätzel, Park and Snaith in 2012.[16,17] Over the next few years, perovskite-based solar cells have kept pushing the performance limits to 25.5% at present, and it has found a wide range of uses outside from the photovoltaic realm.[6]

2.1.2 Crystal Structure

Perovskites present a stoichiometry of ABX_3, where A is a large cation – usually an alkali, alkaline metal or even a small molecule like methylammonium (MA), formamidinium (FA) or cesium (Cs). B is a smaller metal cation like lead (Pb) or tin (Sn). X are anions, usually oxygen or halides like iodide (I) and bromide (Br). These ions arrange into a cubic, tetragonal, or octahedral geometry, depending on the radii of the ions and the temperature of the material, as depicted in Figure 2.1.

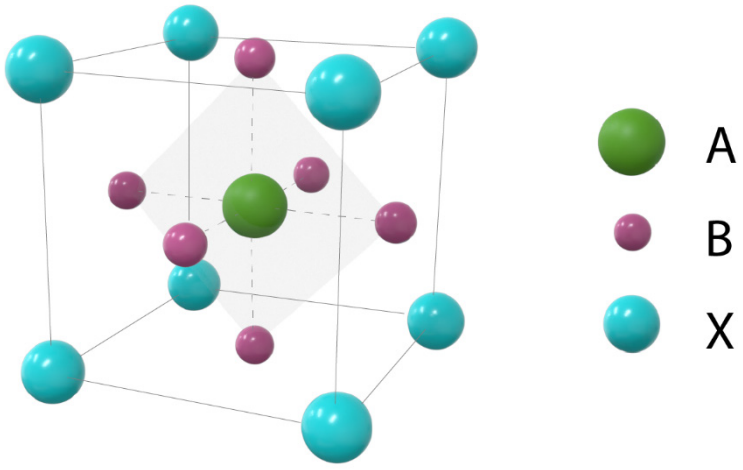

Figure 2.1. Structure of the perovskite crystal in a cubic phase.

In general, the perovskite structure can only form if the ion radii follow the Goldschmidt tolerance factor t, described as

$$t = \frac{r_A + r_X}{\sqrt{2}\ r_B + r_X}\ , \qquad 0.8 < t < 1\ , \tag{2.1}$$

where r_A, r_B, and r_X are the ionic radii of A, B, and X.[18] If the tolerance value is lower than 0.8, other low-dimensional perovskite-derivatives can be formed. For example, Ruddlesden-Popper perovskites have a two-dimensional phase with high stability, flexibility and other enhanced optoelectronic properties.[19]

Perovskite oxides, with an ABO_3 structure, are the most common type of perovskites. In fact, the most abundant mineral on Earth is a perovskite oxide with a composition of $MgSiO_3$, constituting up to 38 vol.% of Earth.[20] Other types of perovskite oxides have been widely studied due to their special properties like superconductivity, insulation, ferro-, piezo-, and pyroelectricity, among many others.[21]

Metal halide perovskites form a subset of the perovskites group that show unique photophysical properties. Their popularity has increased over the last few years due to, among other things, the expedited development of power conversion efficiencies when employed in photovoltaic devices.[22] Depending on the type of cation found at the A-site of the lattice, they are considered inorganic or hybrid.[23] Hybrid metal halide perovskites, combining both organic and inorganic cations, have shown advantageous properties that will be discussed in the following sections.

2.1.3 Physical and Chemical Properties

MHPs show a wide variety of significant properties. For example, bandgap tunability, high absorption coefficient, defect tolerance, ambipolarity, photon recycling, among others. Additionally, the preparation process of MHPs allows for the fine control of their characteristics. For example, the choice of solid precursors and solvents leads to specific complexations that affect the crystallization process. Also, the use of certain precursors can influence the quality and resistance of the crystals.

Bandgap tunability is one of the most advantageous aspects of MHPs. By changing the ratio and type of halides, it is possible to regulate their emitting color, derived from the material's bandgap which can be tuned from 1.5 to 2.3 eV.[24] In solution, colloidal nanocrystals of perovskite can also emit in a wide range of colors, going from the ultraviolet (UV) to the infrared (IR), as shown in Figure 2.2a.[25] This has brought much interest to the use of perovskites

as a design tool since colored solar panels can be added into different types of artistic or architectural models.[26] Furthermore, according to the Shockley-Queisser limit, the bandgap of these materials indicates that they can reach efficiencies as high as 31% as a single junction.[27]

Besides the bandgap tunability, MHPs also show a high absorption coefficient (10^4-10^5 cm^{-1}), making it comparable to other highly efficient semiconductors such as GaAs and CIGS.[16,28] The high absorption comes from a favorable direct bandgap, which is common in other highly efficient semiconductors used for photovoltaics.[29]

In a MAPI crystal, the valence and conduction bands are formed by the molecular orbitals of iodine and lead, respectively.[30] Whenever a defect forms in the lattice, usually as vacancies or interstitials, traps are mostly created near or outside the bandgap.[30] This makes this class of materials highly defect tolerant.

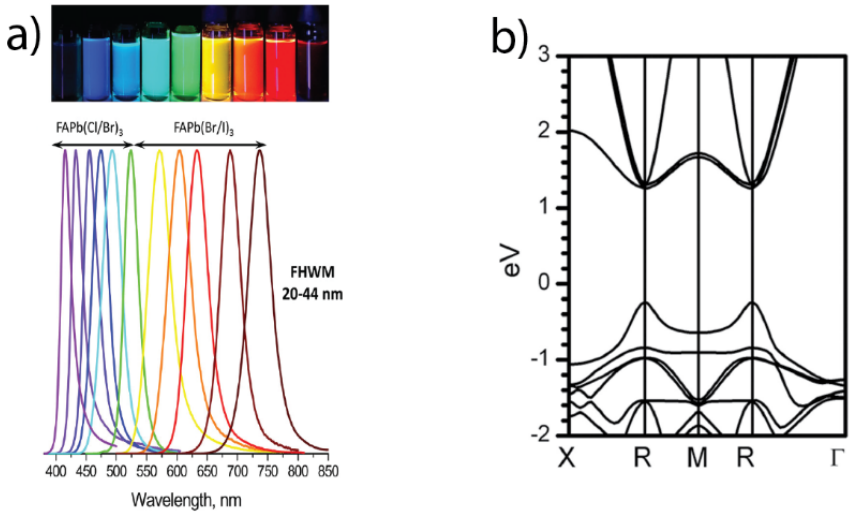

Figure 2.2. a) Emission from UV to IR of perovskite quantum dots in solution, from Ref. [25], and b) Band structure of a MAPbI3 perovskite, from Ref. [30].

Furthermore, the valence and conduction bands have comparable dispersions, as shown in Figure 2.2b, which allows for an equilibrated movement of holes and electrons, respectively.[31,32] This promotes good charge transport properties and high mobilities (of tens of $cm^2V^{-1}s^{-1}$ for polycrystalline samples),[33,34] which facilitates photon recycling in the crystals, leading to large diffusion lengths (longer than 1 μm) and long carrier lifetimes (longer than 1 μs).[35–37] Electron-hole pairs are generated with a low binding energy, within k_BT, which results in the generation of charge carriers that are mostly unbound.[38–40]

Perovskite devices are prepared from precursor salts that are diluted into ionic solutions. Complexes formed between the salt ions and the solvents generate colloids, which serve as seeds for the crystal formation.[41] To dissolve these salts, aprotic solvents are needed, as is the case of dimethylformamide (DMF), dimethyl sulfoxide (DMSO), N-methyl-2-pyrrolidone (NMP), acetonitrile (ACN) and gamma-butyrolactone (GBL). The strength of these solvents as Lewis bases is directly related to their coordination with the lead salts.[42] It has been shown that this coordination is an essential part of the crystallization process, as they form intermediate states that directly influence the morphology of the crystals.[43,44]

Furthermore, the effect of the solid precursors has also been widely investigated. For instance, the quality of the crystals can be enhanced by adding spectator ions, which form a crucial part of the crystallization process, as it is the case of chlorine and acetate.[45] However, they are completely removed after annealing. The stability of the crystal as well as the bandgap can be adjusted by adding a small portion of different cations, as it is the case for potassium , rubidium, and cesium, which in some cases form non-perovskite species around the perovskite crystals that protect them from external influences.[46,47]

The crystal quality can also be enhanced by controlling the crystallization process of the material. In a lab scale, where samples are mostly prepared by spin coating, the perovskite crystallization is induced by applying an antisolvent to the wet layer. The antisolvent, which can be chlorobenzene, anisole, or toluene, mixes well with the perovskite solvents but does not dissolve the perovskite precursors. The effect of the antisolvent is to facilitate the removal of the solvents to allow the crystal seeds to grow.[48] Many other techniques have been developed to induce the crystallization process, like a two-step deposition of precursors,[49] applying a pressure drop,[50] using a flow of nitrogen,[51] or high temperatures.[52]

2.1.4 Challenges

On the downside, MHPs show a few disadvantages compared to other technologies. One of them is the presence of a strong hysteresis effect due to capacitive currents. These currents are generated from ion migration and nonradiative recombination which occur at the interface with the charge transport layer.[53]

The presence of lead is another challenge to overcome, especially when planning towards a commercial use of perovskites. Lead is a well-known polluter and poses a health risk to living

beings.[54] Initially, a replacement of lead by tin was considered, however, the toxicity of tin is still comparable to that of lead.[55] A big effort has been put into finding lead-free perovskite alternatives, in which Sn and Ge-based perovskites have shown the most promise in photovoltaics (PV) with a power conversion efficiency (PCE) close to 10%.[56] However, these efficiencies are still much lower than the Pb-based record of 25.5%.[57]

The stability of MHPs is still a problem that needs to be tackled. Silicon solar cells, the baseline technology, have an expected lifetime of 25 years, while the maximum lifetime reported for perovskites under the same testing standards has been of less than 6 months.[58]

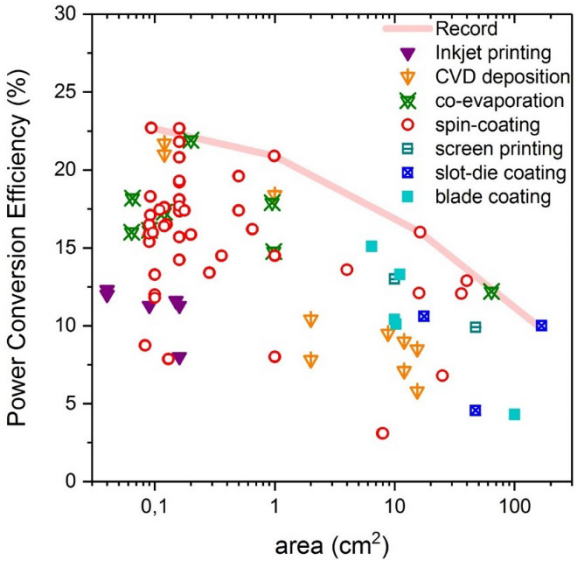

Figure 2.3. Published solar cell performances against the device active area. The performance dramatically reduces as the active area increases. Image taken from Ref. [59].

Scalability is another challenge that needs to be addressed. There is a large discrepancy between the performance of small and large devices, see Figure 2.3. The reduction of performance on large area devices occurs in general due to an increase of the parasitic resistances, which in turn is caused by long diffusion lengths.[60] In the case of perovskites, large areas are harder to crystallize in a homogenous way, increasing the probability of forming defects or gaps across the device area, which would in turn form recombination sites and shunts.

Despite their shortcomings, MHPs are promising materials with many attractive properties that have rapidly developed in the last few years. They are easy to prepare and deposit via spin coating, inkjet printing, slot-die coating and a wide variety of other methods.[61] Today, perovskites are being developed for many applications such as light emitting diodes (LED),[62] field effect transistors (FET),[63] lasers,[64] memory devices,[65] and different types of sensors.[66–68]

In the photovoltaic realm, development of tandem solar cells with CIGS and silicon based solar cells are revolutionizing the field with unprecedented records.[57,69]

In this thesis, we explore two types of MHPs. One is $MAPbI_3$, a perovskite formed of methylammonium, lead, and iodide which is also referred to as MAPI. Its simple composition allows for fast experimentation and analysis while still being able to reach high efficiencies as solar cells. However, this material shows a general poor stability, especially under ambient conditions.[70] The second MHP is the so-called triple cation, or CsMAFA. This is a hybrid MHP formed of cesium and two organic compounds as cations – methylammonium and formamidinium –, as well as lead, iodide, and bromide as the other ions. This material exhibits a higher reproducibility and a more robust stability under ambient conditions. Although currently MHPs still display lower stabilities than other photovoltaics, these materials have shown promise to become the next generation of highly efficient photovoltaics.

2.2 Solar Cells

In this section, solar cells will be put into context as promising green alternatives for power generation. First, the different types of photovoltaic materials will be discussed. Then, the mechanisms of charge generation and recombination will be described. Finally, the diode model and main characteristic parameters of solar cells will be examined.

2.2.1 Foundations

In general, a solar cell generates a voltage when exposed to light due to the photovoltaic effect, producing an electric current if the cell is connected to a circuit. Photon absorption is possible because the active material of the cell, the semiconductor, has an energetic region where no electronic states can exist, called the *bandgap*. The bandgap corresponds to the energetic difference between the valence band maximum (VBM) and the conduction band minimum (CBM) of the semiconductor. The valence band is formed by the delocalized valence electrons of the crystal's atoms while the conduction band is formed by delocalized excited electrons.

The photovoltaic effect, which makes solar cells possible, was first discovered by E. Becquerel in 1839. This phenomenon describes the generation of voltage in a material through its exposure to light.

The first modern solar cell was developed by D. Chapin and collaborators from Bell Labs in 1954.[71] Using a junction of silicon with impurities of boron and arsenic, they built a solar cell that achieved a 6% efficiency.[71] The type of solar cell they created is considered the first generation of photovoltaics.

Solar cells are made from sliced silicon ingots. For this, a carbon arc furnace is used to isolate silicon from silicon dioxide. Further purification is done through a floating zone process. Multiple ingot growing methods exist, being the most common the Czochralski process.[72] Here, a small silicon crystal seed is dipped into a bath of molten silicon. The seed is then slowly pulled out of the bath while spun, allowing the molten silicon to crystallize. Once the process is done and the crystal cooled, the ingot is sliced into thin substrates.

Impurities can be added to the molten silicon to change their optical and electrical properties in a process called doping. For example, n-doping can be accomplished by using elements with 5 valence electrons, like arsenic or phosphorus, creating a negatively charged crystal with electrons as majority carriers. On the other hand, p-doping is done with elements having 3 valence electrons, like boron or gallium atoms, resulting in a crystal that is positively charged. Doping can also be accomplished by ion implantation by using a particle accelerator, or by impurity diffusion, which has to be done at temperatures above 800 °C.[72] The active area of this type of cells is limited to the diameter of the ingots, which today can be as large as 400 mm.[73]

The majority of semiconductor devices are built as p-n junctions. Here, a negatively (n-) and a positively (p-) doped layers are merged to promote the separation of charges. When the doped layers are in contact, majority carriers move across the junction. That is, electrons from the n-side and holes from the p-side – the majority carriers – diffuse into to the opposite layer. This process results in the annihilation of charges near the junction, creating a region depleted of charges.[74] The unbalance of charges on this region creates an electric field that favors the movement of minority carriers into the opposite layer.[74] This type of junction is also called a homojunction, since the same material, with different types of doping, is used for both halves of the junction.

Currently, silicon-based solar cells are still the most common type of photovoltaic material, representing more than 90% of the total market share.[6] They are found either as a single crystal or as polycrystals and can reach efficiencies as high as 26.7%.[6] The photovoltaic effect, however, is also shown by other materials that have a different set of characteristics.

Thin film materials form the so-called second generation of photovoltaics. Examples of them are cadmium telluride (CdTe), copper indium gallium diselenide (CIGS) and amorphous silicon (a-Si:H).[75] The advantage of these materials is that they can be directly deposited onto a substrate. This eliminated the size limit of silicon-based solar cells built from ingots and extended it to the size of glass substrates, which can be much larger than 400 mm in diameter.[76] Other advantages of these materials are that only a few microns of material is necessary to build devices with efficiencies as high as 15% and the bandgap can be tuned for some of them.[76] On the downside, the manufacturing process is difficult and, since most of these materials are niche products, the costs of production are generally high.[77] Thus, they form today about 5% of the total photovoltaic energy production in the world.[4,78]

Additionally, there is a third generation of photovoltaics. These are solution processable thin-film devices which are found in the form of organic molecules, dyes (for dye sensitized solar cells, DSSCs), copper zinc tin sulfide (CZTS), quantum dots and metal halide perovskites. One of the biggest advantages of this type of materials is that the bandgap can be tuned, meaning that the emission and absorption of these devices can be controlled.[79] This also allows them to be used in tandem with other materials, such as silicon and GaAs solar cells, to enhance their overall efficiency.[80] Additionally, deposition techniques are simpler than for the previous generations and the material costs are lower, facilitating the further reduction of the costs of energy production.[78,81] On the downside, many of these materials are sensitive to oxygen, water, high temperatures and UV light, reducing their stability under ambient conditions.

A useful parameter to understand junctions is the *work function*. The work function of a material is equal to the potential between the vacuum and Fermi levels. In other words, the value describes the required potential to completely remove the least tightly bound electron of the material. Its magnitude is equal to the *electron affinity* and *ionization potential* in metals.[82] The concept is redefined for semiconductors due to the existence of the valence and conduction bands. At absolute zero, electrons in a semiconductor have no kinetic energy. The valence band can be filled with electrons up to a point called the *Fermi energy* or *Fermi level*.[82] As the temperature increases, kinetic energy added to the electrons would displace them to a higher

energy level, out of the bandgap. In pure semiconductors at room temperature, the Fermi level is found right in the middle of the valence and conduction bands, while in the case of doped semiconductors, the additional charges will shift it up or down for n-type or p-type materials, respectively. Junctions built with materials having different bandgap values are called *heterojunctions*. The n-type GaAs on p-type AlGaAs is an example of a p-n heterojunction.[83]

There are also metal-semiconductor junctions. Perovskite solar cells are built this way, where an intrinsic (i), or pure, semiconductor is placed in between conductive layers. These conductive layers are usually chosen in a way that the resulting electric field would favor the diffusion of only the minority carriers, which are electrons or holes in p- or n-doped materials, respectively, into the metal layer. This is known as a *Schottky barrier*.[82] When the diffusion of majority carriers is favored, it is called an *ohmic contact*.[82]

Third generation photovoltaics are generally found as semiconductor-semiconductor junctions in two main architectures: n-i-p and p-i-n, where the order of the first letter signals the conductive layer through which light enters the device. In this type of junction, carriers are required to move a longer distance before they spontaneously recombine, a parameter called diffusion length, so it is possible to extract them at the contacts.[84] Most organic solar cells are prepared as bulk heterojunctions due to their short diffusion lengths.[85] Here, the donor and acceptor materials are blended in such a way that the distance from one to the other is minimized to the nanometer range.[86,87] In the case of perovskites, most of the latest photovoltaic devices are prepared in a planar architecture, where all the layers are deposited flat and unstructured. This is possible because MHPs have long diffusion lengths.[88] Additionally, the mesoscopic architecture for perovskite devices is used to increase the contact area between the n-doped material, usually titanium dioxide (TiO_2), and the perovskite. Here, a highly porous material – called mesoporous – is infiltrated with the semiconductor before it crystallizes.[89]

2.2.2 Physics of Solar Cells

Solar devices work by absorbing the electromagnetic radiation in the form of photons from light sources, like the sun. The sun emits photons at different intensities across a wide range of wavelengths, as shown in Figure 2.4. The radiation from the sun outside of Earth's atmosphere can be approximated to the radiation emitted by a material, so-called black body, that is heated to 5800 K. On Earth, a portion of the photons is partially absorbed by atmospheric gases, like

water vapor, carbon dioxide, nitrous oxide, methane and fluorinated hydrocarbons, dust and ozone.[74] The absorption intensity of these gases can be calculated by the air mass, $AM = (\mathrm{Cos}\,\theta)^{-1}$, where θ is the angle of incidence to Earth.[90]

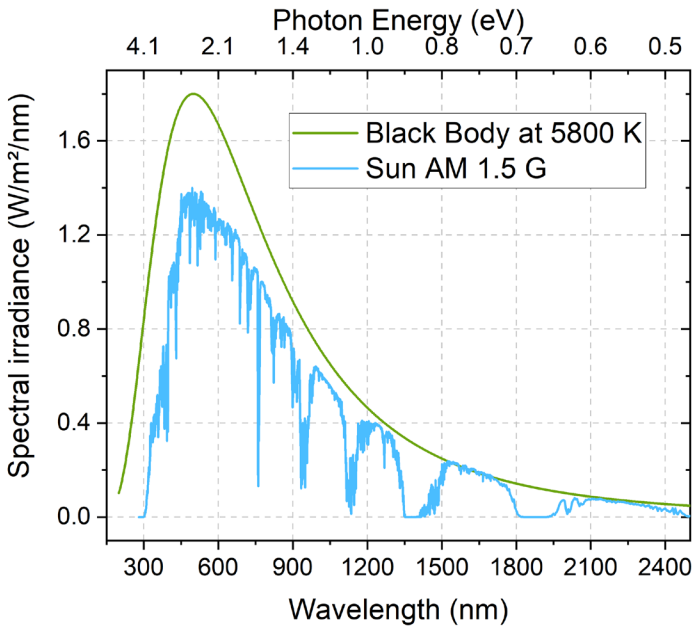

Figure 2.4. The radiation spectrum of a black body at 5800 K and the AM 1.5 G spectrum.

As a standard, the performance of photovoltaic devices is measured with a light source that is comparable to the sun's emission at an incidence angle of 48.2° and a power density of 1 kW/m². This is known as AM 1.5 G, where G stands for "global", meaning that the spectrum considers a diffusive component of scattering and reflection by the atmosphere.[90] Furthermore, the energy of a photon E is related to its wavelength λ by $E = \frac{h\,c}{\lambda}$, where h is Planck's constant and c is the speed of light.

The possible paths that a photogenerated charge can follow in a semiconductor are shown in Figure 2.5. First, photons excite electrons from the valence band into the conduction band as shown in Path 1. This only occurs if the photon's energy is equal or larger than the bandgap of the material. Once in the conduction band, electrons are free to move across the molecule or crystal lattice.

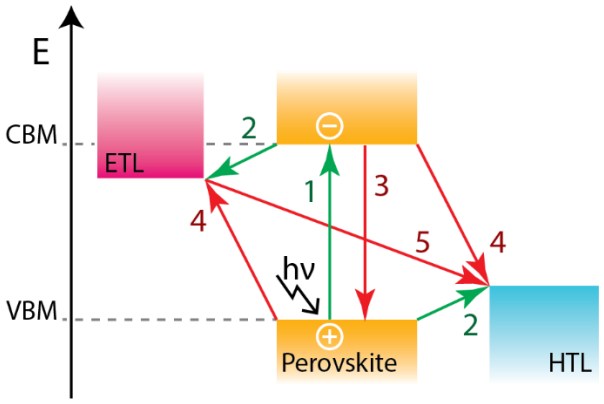

Figure 2.5. Diagram of carrier generation and recombination processes of a solar cell. Paths 1 and 2 are favorable, in green, while 3, 4, and 5 are unfavorable, in red.

When the electron is excited, a void is left behind in the valence band. This void is a quasiparticle called *hole* and behaves exactly like an electron but with a positive charge and opposite momentum. Conductivity occurs when holes in the valence band are displaced by neighboring electrons due to an exerted electric field. Alternatively, due to electrostatic Coulomb forces, electron-hole pairs can remain bound into what is known as *excitons*. Selective contacts are then used to break the binding force and separate the exciton into free charges (see path 2 in Figure 2.5). That is, the electron in the conduction band then diffuses into the electron transport layer (ETL) while the hole diffuses into the hole transport layer (HTL). These charges generate a current if they are successfully extracted from the contacts. Charge transport layers (CTLs) can also work as blocking layers. For example, electrons in the CBM are prevented to move to the cathode due to the energy difference with the HTL. The same is true for holes in the VBM and the ETL.

Additionally, unwanted events can happen. For example, electron-hole pairs can recombine before they are separated. Specifically, an electron in the CBM can radiatively recombine with a hole in the VBM, emitting a photon (path 3, Figure 2.5). Conversely, the recombination can occur non-radiatively, where the energy is dissipated as heat. A similar process can occur where charges become trapped by defects in the middle of the bandgap. From here, trapped charges can recombine directly with other charges, or in the case of electrons, they can decay non-radiatively to the valence band. When the blocking properties of the CTL are not correctly matched with the semiconductor, charges can recombine at the junction, as shown in path 4. Finally, charges can recombine directly from the ETL to the HTL (path 5). This happens when there are pinholes in the active layer that allow a direct contact between the CTLs.

Recombination Mechanisms

The processes shown in Figure 2.5 reach an equilibrium under illumination and steady state conditions. Specifically, paths 1, 2, and 3, the generation and recombination processes of a semiconductor in equilibrium are described by the rate equation as[91]

$$\frac{dn}{dt} = G - k_{tr}n - \gamma\, n^2 + k_q[Q]\ , \qquad 2.2$$

where G is the generation rate of electrons and holes, k_{tr} is the monomolecular recombination coefficient that occurs between bound charges, γ is the bimolecular annihilation constant that occurs between unbound charges, k_q is the quenching coefficient that occurs with charges of other materials, n are the concentrations of electrons, and $[Q]$ is the concentration of quenchers.

The phenomenon of recombination is closely related to the photogeneration of mobile charges and can occur in two main different ways: radiative and non-radiative recombination. Furthermore, there are three main recombination mechanisms: Auger, trap-assisted, and surface recombination, and they will be discussed in the following paragraphs.

Radiative recombination is a loss mechanism that cannot be avoided.[82] This happens when the spontaneous annihilation of an electron and a hole generate a photon. The rate is dependent on the concentration of electrons n_{e} and holes n_{h}, and it is described by[74]

$$G_{\gamma} = R_{\mathrm{e}} = R_{\mathrm{h}} = B\, n_{\mathrm{e}}\, n_{\mathrm{h}}, \qquad 2.3$$

where G_{γ} is the generation rate of photons, R_{e} and R_{h} are the recombination rates of electrons and holes, respectively, and B is the coefficient of radiative recombination. In a perfect material, radiative recombination is the only mechanism that limits the efficiency of the cell.[82]

Another unavoidable type of recombination is where either two electrons and one hole, or vice versa, interact during the so-called *Auger recombination*. Here, the two alike carriers bounce off each other exchanging kinetic energy. This results in one of the carriers recombining with the opposite charge across the bandgap, while the third one is excited to a higher kinetic level, proportional to the bandgap. The excess of energy in this excited carrier is ultimately lost as

heat.[82] This type of recombination is more predominant on materials that have a high density of charge carriers and a small bandgap. The Auger recombination rate R_{Aug} is described by[74]

$$R_{\mathrm{Aug}} = n_{\mathrm{e}}\, n_{\mathrm{h}}\, (C_{\mathrm{e}}\, n_{\mathrm{e}} + C_{\mathrm{h}}\, n_{\mathrm{h}}) \qquad 2.4$$

where C_{e} and C_{h} are recombination coefficients for electrons and holes, respectively. This type of recombination can be enhanced with a higher level of doping of the materials.[82]

Unlike radiative or Auger recombination, Shockley-Read-Hall (SRH) recombination, also called *trap-assisted recombination*, is an avoidable process that is dependent on the number of defects or impurities in the crystal structure. Here, impurities in the crystal lattice form localized traps inside the band gap where electrons or holes can be captured. If the localized states are close to either the CBM or the VBM, the traps are shallow and only admit the closest type of minority carriers. An increase of temperature can remove charge carriers from these traps.[82] If the states are localized near the middle of the bandgap they are called recombination centers, since either electrons or holes can be trapped.[74] Additionally, since they are located well within the bandgap, this type of recombination predominantly results in non-radiative recombination. SRH recombination rate is dependent on the excess carrier density and it is strongest when the concentration of electrons and holes is similar.[82]

Additionally, surface recombination occurs near the boundary of the semiconductor, where a larger density of defects and impurities are found. Here, external molecules, like oxygen, can be adsorbed onto the semiconductor. As the recombination sites are located at the two-dimensional surface, the recombination rate is given in terms of a cross-sectional area. This type of recombination is characterized by the surface velocity ν_{R}, which is used to measure the surface quality of the material.[74] A value of zero indicates that there is no recombination.[82] The surface recombination rate R_{Surf} is similar to the one from trap-assisted recombination and for electrons it is described as

$$R_{\mathrm{Surf,e}} = \sigma_{\mathrm{surf,e}}\, \nu_{\mathrm{e}}\, n_{\mathrm{surf,h}}\, n_{\mathrm{e}} = \nu_{\mathrm{R,e}}\, n_{\mathrm{e}} \qquad 2.5$$

where $\sigma_{\mathrm{surf,e}}$ is the capture cross section of electrons, ν_{e} is thermal velocity, $n_{\mathrm{surf,h}}$ is the density of surface states per area occupied by holes and $\nu_{\mathrm{R,e}}$ is the surface recombination velocity.[74]

Furthermore, bimolecular recombination occurs when delocalized charges in the valence and conduction bands, so-called band-to-band, become spontaneously annihilated. This process is analogous to non-geminate recombination in organic semiconductors. When the carriers are bound, as is the case of SRH recombination, the process is called monomolecular recombination. The analogous term in organic semiconductors is called geminate recombination, which occurs in bound electron-hole pairs.[92]

2.2.3 Solar Cell Parameters

To characterize the behavior of a solar cell, the Shockley diode equation is used:

$$J_{\text{dark}}(V) = J_0(e^{q\,V/K_B T} - 1) \qquad 2.6$$

where J_{dark} is the dark current density and describes the current that flows in the diode while a voltage V is applied in dark conditions. J_0 is the saturation current, q is the charge of an electron, K_B is Boltzmann's constant and T is the temperature.[74]

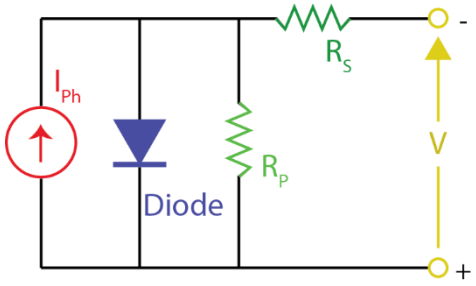

Figure 2.6. Circuit diagram of a solar cell with parasitic series (R_S) and parallel (R_P) resistances.

In real conditions, the behavior of the cells is slightly different from what is expressed in eq. 2.9. For a better correlation, the equation is modified into a non-ideal diode model, where an extra exponent of value $1 < m < 2$ is added. A large value of m results in a lower fill factor. The maximum fill factor of an ideal diode is 86%.[82] This model is expressed as

$$J(V) = J_{SC} - J_0\left(Exp\left[\frac{q\,V}{m\,K_B T}\right] - 1\right). \qquad 2.7$$

Additionally, the effect of parasitic resistances of a solar cell circuit in real conditions can be taken into consideration.[74] For instance, two extra resistances are added into the model, one in

series (R_S) and another in parallel (R_P), the so-called shunt resistance. A diagram of this circuit is shown in Figure 2.6 and the equation is expressed as

$$J(V) = J_{SC} - J_0 \left(Exp \left[\frac{q\,(V + I \cdot R_S)}{m\,K_B T} \right] - \frac{V + I \cdot R_S}{R_P} \right), \qquad 2.8$$

where the current $I = J \cdot A$, and A is the active area of the solar cell.[74] The effect of these parasitic resistances directly alters the behavior of the device, as will be described below.

The characteristic current response of the diode when voltage is applied can be approximated as the sum of the dark current and the short circuit current (J_{SC}) of the device, $J(V) = J_{SC} - J_{dark}(V)$, where the signs correspond to the current flow direction.[82] This is known as the current-voltage (JV) characteristic of the diode, depicted in Figure 2.7, and it is expressed as

$$J(V) = J_{SC} - J_0 \left(Exp \left[\frac{q\,V}{K_B T} \right] - 1 \right). \qquad 2.9$$

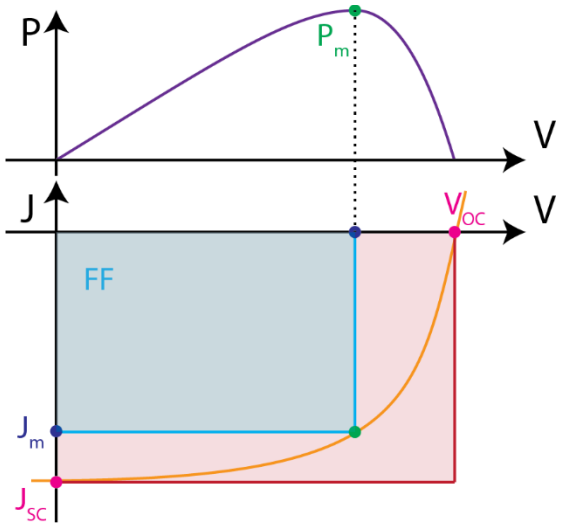

Figure 2.7. Diagrams of the power vs voltage (top) and current vs voltage (bottom), also called JV characteristics of a solar cell. J_{SC}, V_{OC} and P_M and FF areas are marked accordingly.

Another significant characteristic of solar cells is the maximum reachable voltage, achieved when no current is flowing through the diode. This is called the open-circuit voltage (V_{OC}) and is derived from eq. 2.9 as

$$V_{OC} = \frac{K_B T}{q} \ln\left(\frac{J_{SC}}{J_0} + 1\right). \qquad 2.10$$

The power of the solar cell is given by $P = J\,V$. As bias is applied to the solar cell under illumination, the power reaches a maximum value, as shown in Figure 2.7. This is called the maximum power point (P_M). The current density and voltage values at the maximum power point are denoted J_M and V_M, respectively. From here, the quality of the cell can be evaluated by the fill factor (FF), which measures how well the resulting maximum power fits the current-voltage characteristic, and is defined as

$$FF = \frac{P_M}{J_{SC}\,V_{OC}} = \frac{J_M\,V_M}{J_{SC}\,V_{OC}}\,. \qquad 2.11$$

The fill factor of the solar cell is maximized when the series resistance, as described by eq. 2.8, is small and the shunt resistance is as large as possible.[82] A large series resistance would affect the performance of the cell by reducing the short circuit current while a small shunt resistance would do it by decreasing the open circuit voltage of the diode.

With this, the power conversion efficiency (PCE) of the cell can be calculated as the ratio of the cell's maximum power (P_M) to the light power density (P_s). Using eq. 2.11, this is expressed as

$$PCE = \frac{P_M}{P_s} = \frac{J_{SC}\,V_{OC}\,FF}{P_s}\,. \qquad 2.12$$

Finally, the external quantum efficiency (EQE) of the cell, also known as the incident photon-to-converted-electron ratio (IPCE), measures how efficiently photons n_{ph} are converted to electrons n_e. It is described as

$$EQE = \frac{n_e}{n_{ph}} = \frac{I_{ph}}{q}\left(\frac{h\,\nu}{p_{opt}}\right), \qquad 2.13$$

where I_{ph} is the photocurrent, and p_{opt} is the optical power.[84]

2.3 Photoluminescence

The electronic properties of semiconductors, like perovskites, can be studied by the light they emit after they have been excited with a light source. In this chapter, the historic developments surrounding this topic will be briefly discussed. Then, the phenomenon will be described in detail as well as charge transfer mechanisms, followed by a description of the spectroscopic methods that have been developed using this phenomenon. Finally, the Stern-Volmer model, which characterizes the charge transfer between an emitter and an acceptor molecule, will be examined.

Photoluminescence (PL) is the phenomenon where a substance emits light due to excited electronic states induced by the absorption of photons. The phenomenon was first described by N. Monardes in 1565. Many important contributions to the subject were made in the 1800s by figures like E. Becquerel and G. C. Stokes. However, the phenomenon was not fully understood until the development of quantum theory in the 1900s.[93]

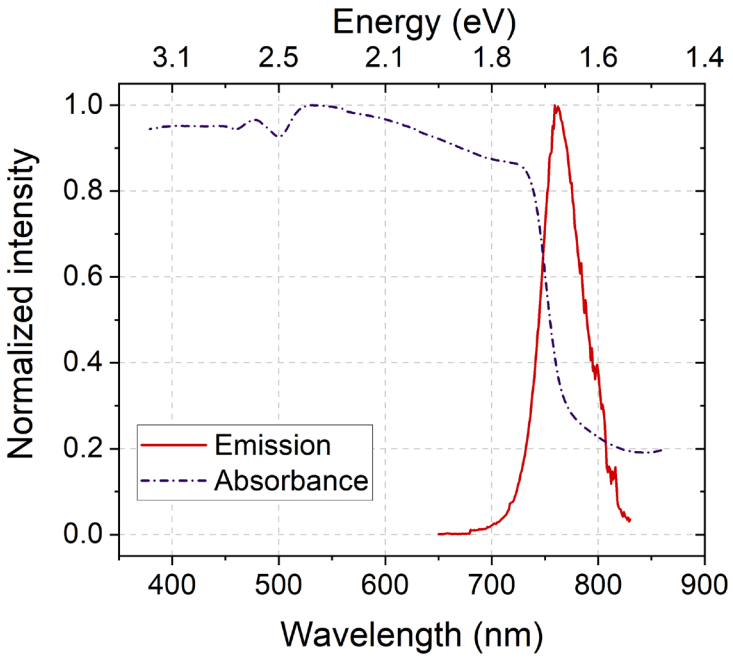

Figure 2.8. Absorption and emission spectra of triple cation perovskite.

2.3.1 Photoluminescence Mechanisms

Photoluminescence occurs after a photon is absorbed by a material. The material then emits another photon of lower energy than the one which was absorbed. This change of energy is

depicted in Figure 2.8. Fluorescence and phosphorescence are types of photoluminescence which will be described later on this chapter.

Absorption of a photon is possible because an electron in the material, which is in the ground state (S_0), can become excited to a higher electronic state (S_1 or S_2). This is shown in the Jablonski diagram in Figure 2.9. Once the electron is excited, a few processes can take place. If the electron is excited to a higher vibrational level, it will always relax to the nearest lower electronic state, usually S_1. If the excitation is at S_2, it can undergo an internal conversion and relax non-radiatively to S_1. It can also decay radiatively by emitting a photon as it returns to S_0. The process is called *fluorescence* if it occurs within 10^{-9}-10^{-7} s.

Alternatively, an electron in S_1 can flip its spin and form a triplet state T_1. Once the electron is in a triplet state, it can either decay radiatively in a process called *phosphorescence*, or non-radiatively. The flipping process to a triplet state takes additional time, extending the time until emission to 10^{-3}-10^{-2} s.[94]

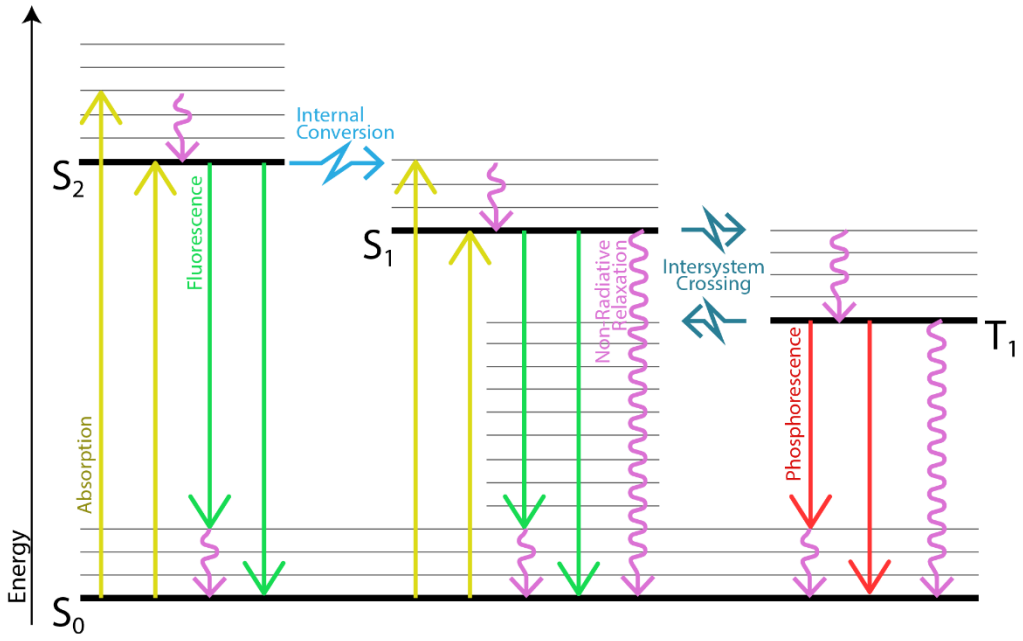

Figure 2.9. Jablonski diagram showing the electronic states of a molecule. Absorption is shown in yellow, fluorescence in green, phosphorescence in red. Non-radiative relaxation appears as purple wavy lines, internal conversion as a blue line and intersystem crossing as dark blue arrows.

As depicted in Figure 2.9, emitted photons tend to be less energetic than the absorbed ones. Emitted photons have a reduced energy due to losses induced by vibrational relaxations. This creates a red shift of the emission spectra with respect to the absorption known as *Stokes shift*.

Triplet states are energetically lower than singlet ones, making the resulting phosphorescence spectrum even more red-shifted.[93] Moreover, electronic states in a semiconductor crystal merge together forming bands where electrons are delocalized. For this reason, the absorption onset of the material corresponds approximately to the bandgap energy.[93]

2.3.2 Spectroscopic methods

Spectroscopic methods, like absorption and emission spectroscopy, have been developed to directly probe optoelectronic properties like the bandgap as well as charge transport properties of the semiconductor. Two important parameters that can be extracted from these techniques are the PL lifetime and PL quantum yield (PLQY) and will be explained in the following paragraphs.

The PL lifetime measures the average time that an excited species takes to relax to the ground state. It considers the decay rate of the radiative k_r and non-radiative k_{nr} species as $\tau = (k_\mathrm{r} + k_\mathrm{nr})^{-1}$. A common way of measuring this value is through *time-correlated single photon counting* (TCSPC). Here, a periodic light signal is used to excite charges in the sample.[95] Then, a detector that is synchronized with the frequency of the excitation light measures the elapsed time and counts the emitted photons coming from the sample. The process is repeated until enough collected photons show an intensity decay of 3 orders of magnitude, preferably.[94] This process is similar to the *delayed coincidence* method used to measure the decay of unstable nuclei in nuclear physics.[95] The resulting intensity decay curve can be fitted with a multi-exponential model of the form

$$I(t) = \sum_{i=1}^{\mathrm{n}} \alpha_i \exp\left(-\frac{t}{\tau_i}\right) \ , \qquad 2.14$$

where τ_i are particles lifetimes and α_i are the amplitudes of the components at $t = 0$. Depending on the amount of known decaying particles, the term n is chosen. Furthermore, if the mobility of the particles is known, the PL lifetime can be used to determine their diffusion length.

The other parameter, PLQY, measures the efficiency at which absorbed photons are being converted to emitted photons. It is defined with respect to the decaying rates as

$\Phi_F = k_r \cdot (k_r + k_{nr})^{-1}$.[93] Additionally, PLQY can be measured by a *direct excitation* method. For this, the ratio of emitted photons (N_{em}) with respect to the absorbed ones (N_{abs}) is calculated. Here, an integration sphere, which is a highly reflective spherical container, is used to collect all the emitted photons and to direct them towards the detector. The absolute PLQY (η) can then be calculated as

$$\eta = \frac{N_{em}}{N_{abs}} = \frac{E_R - E_M}{S_R - S_M} , \qquad 2.15$$

where S_M and E_M are scattered and emitted photons by the material, respectively, and S_R and E_R are scattered and emitted photons of a blank reference, respectively.

2.3.3 Charge Transfer Mechanisms

Besides radiative and non-radiative decay of photogenerated carriers inside of the semiconductor, the excited state of one molecule, called donor, can also be transferred to a different one, called the acceptor. This process is known as Resonance Energy Transfer (RET). However, for this to happen, the emission spectrum of a donor material must overlap with the absorption emission of the acceptor. This process is non-radiative, meaning that the donor is not required to be luminescent. These type of dipole-dipole Coulombic interactions can occur at within distances of 1 to 10 nm and are described by the *Förster mechanism*.[93] Energy transfer can also occur at shorter distances due to intermolecular orbital overlap between the donor and acceptor where an electron is exchanged. This is known as the *Dexter mechanism* and involves electronic triplet states. A well-known molecule that undergoes an electronic energy transfer (EET) of this type is molecular oxygen.[96,97] For luminescent donor materials, the transfer of energy that results in the absence of emitted photons is called *photoluminescence quenching*, and the acceptor material is called a *quencher*. The rate of Förster energy transfer is given by[93]

$$k_{T(r)} = \frac{1}{\tau_D}\left(\frac{R_0}{r}\right)^6 \qquad 2.16$$

where r is the distance between donor and acceptor, $\tau_D$is the lifetime of the unperturbed donor and R_0 is the Förster Radius, which marks the distance at which the energy transfer is 50% efficient.

2.3.4 Stern-Volmer Model

Fluorescent dyes can be designed to exploit the quenching behavior of molecules. Some of them can react selectively to certain quenchers.[94] For instance, sensors of this type are used to detect hormones[98], identify explosives[99], pollutants[100] or unwanted particles in a system.[101] The sensing capabilities of molecules are characterized by the Stern-Volmer (SV) model. This model involves a standard technique that has been popularly used in organic chemistry to understand second-order charge transfer mechanisms of diffusive fluorescent molecules and quenchers.[102,103] Developed by O. Stern and M. Volmer in 1919, this technique has been mostly used for systems in solution, although in later years it has also been applied successfully in the solid state.[98,102,104–108]

In general, for every photon absorbed by the emitter, an electron-hole pair is created. Under steady-state conditions, the rate of generation is balanced by the rate of recombination, which can be radiative or non-radiative. The steady-state decay rate is described as $\gamma_{\mathrm{st}} = \tau^{-1} = k_{\mathrm{nr}} + k_{\mathrm{r}}$, where k_{r} and k_{nr} are radiative and non-radiative recombination rates, respectively. With this, the concentration of fluorescent particles in a quencher-free environment can be described by[94]

$$\frac{d[\mathrm{F}^*]}{dt} = f(t) - \gamma_{\mathrm{st}}\,[F^*]_0 = 0, \qquad 2.17$$

where $[F^*]$ is the concentration of excited emitters and $f(t)$ is the constant excitation function.

When quenchers are present, the process is described by

$$\frac{d[\mathrm{F}^*]}{dt} = f(t) - \big(\gamma_{\mathrm{st}} + k_{\mathrm{q}}[Q]\big)[F^*] = 0, \qquad 2.18$$

where k_q refers to decay rate and $[Q]$ is the concentration of quenchers.

The ratio between equations 2.17 and 2.18 can be used to study the effect of quenchers in contact with an emitter. This is known as the Stern-Volmer model and it is expressed as

$$\frac{F_0}{F} = \frac{I_0}{I} = \frac{\gamma_{\mathrm{st}} + k_{\mathrm{q}}[Q]}{\gamma_{\mathrm{st}}} = 1 + k_{\mathrm{q}}\tau_0[Q] = 1 + K_{\mathrm{SV}}[Q], \qquad 2.19$$

where I and I_0 are the PL emission with and without quencher, respectively. K_{SV} is the Stern-Volmer constant, k_q is the bimolecular quenching constant, τ_0 is the quencher-free emission lifetime and $[Q]$ is the concentration of the quencher.[94]

The SV analysis requires the measurement of the PL emission intensity of the donor as it is exposed to increasing concentrations of the quencher. Depending on the trend of the change in emission intensity with concentration, the quenching mechanism can be distinguished between dynamic and static. Dynamic quenching, also called collisional quenching, refers to the process where emitters and quenchers bounce off each other. This results in a charge or energy transfer whenever they come into contact. Static quenching, on the other hand, refers to the binding or complexation of the quencher to the emitter, resulting in a permanent PL quenching.[93] To determine the type of PL quenching, this procedure can be repeated at different temperatures. The quenching rate is expected to increase for dynamic quenching, or reduce for static quenching, with increasing temperature. Alternatively, this information can be extracted by applying equation 2.19 to the change of PL lifetime instead.

Equation 2.19 has been used to effectively describe the quenching phenomena of particles in solution to a high degree of accuracy.[109] However, when the emitters are immobilized and distributed across a layer, a better model is necessary to account for the fractional accessibility of the quenchers to the emitters. Multiple quenching sites are modeled by the following equation[110]

$$\frac{I_0}{I} = \left[\sum_i \frac{f_{0i}}{1 + K_{\mathrm{SV}i}[Q]}\right]^{-1}. \qquad 2.20$$

Although this model considers an unlimited number of quenching sites, it has been shown that two quenching sites are enough to model the permeation of a layer.[111,112] These two sites are defined as one being fast and easily accessible at the surface of the emitter while the other one is more difficult to access and is likely located at boundary defects. This is described by

$$\frac{I_0}{I} = \left[\frac{f_{01}}{1 + K_{\mathrm{SV1}}[Q]} + \frac{(1 - f_{01})}{1 + K_{\mathrm{SV2}}[Q]}\right]^{-1}, \qquad 2.21$$

where f_{01} and $(1 - f_{01})$ are the accessed fraction of total emitters by the quenchers at each condition, K_{SV1} & K_{SV2} are the SV constants for the first and second component and $[Q]$ is the quencher concentration.

2.4 Inkjet Printing

Inkjet printing is a promising digital fabrication technique that can accelerate the scaling up of MHP devices. Inkjet printing presents several advantages over the other techniques, such as allowing the contactless deposition of ink in an additive manner, the possibility of depositing specific shapes without the need of a mask, and coverage of areas larger than 1 m².[113] Additionally, deposition of inks on flexible substrates is more accessible via inkjet printing.[114]

In this section, the historical developments that brought inkjet printing to life are briefly discussed. Then, the two different inkjet printing techniques are described. Later, the printing mechanisms are detailed, starting with the interactions of printhead, ink and substrate, as well as the specific challenges that are faced when printing perovskite solar cells.

2.4.1 Brief History

The working principle of inkjet printing – the formation of droplets from a liquid jet – was first studied by F. Savart in the early 1800s.[115] Additional developments were later achieved by J. Plateau and F. R. S. Rayleigh towards the end of the 1800s.[116,117] However, the first modern application of inkjet printing was developed by R. Elmquist in 1951 while working for Siemens.[118] Inkjet printing of documents quickly became the preferred method for graphical printing in the industry and everyday life.

Nevertheless, the first functional deposition of electronic devices by inkjet printing was performed a few decades later in the form of transistors by Y. Bao and collaborators in 1997.[119] In the case of solar cells, the first ones were developed by a company called Konarka in 2008,

using organic semiconductors in the form of poly(3-hexylthiophene) (P3HT).[120] Today, inkjet printing, combined with roll-to-toll processing, present an effective method to deposit large area solar cells with minimum waste.

2.4.2 Inkjet Techniques

Two techniques have been developed to control the deposition of droplets on a surface: continuous inkjet printing (CIJ) and drop-on-demand (DOD).[121] The former consists of a continuous stream of ink that breaks into droplets due to the liquid's surface tension. During the fall, droplets are electrostatically charged. Electrodes are then used to deflect droplets in or out of a gutter to control the printing process. This method is advantageous when fast printing speeds are needed or when the process is done on highly irregular surfaces. On the other hand, this technique results in a lot of wasted ink. This is especially disadvantageous for most electronic applications, since recycled ink tends to lose its specially engineered properties.[119]

Inkjet printing can also be performed as DOD. Within this technique, two methods have been developed. The first one, called *bubble-jet*, relies on a heating element that partially vaporizes ink to form bubbles that push the liquid ink, out the nozzle as it expands.[114] This technique is commonly used for graphical printing. However, elevated temperatures can damage the ink properties for specialized applications. The second method uses a piezoelectric transducer to create a pressure wave. When the wave matches the resonance of the ink, constructive interference leads to the ink being pushed outside of the nozzle.[121,122] This type of inkjet printing is the most popular today for functional materials because its versatility enables the deposition of a large range of materials in customized patterns. Applications range from the normal printing of documents to the deposition of flexible circuits, optical devices, as well as DNA, proteins and even living tissue.[114] The experiments performed for this thesis were done with DOD inkjet printing.

2.4.3 Component Interactions

A successful DOD inkjet printing process requires the fine adjustment between the ink properties, the printhead configuration and the substrate characteristics. The proper balance of these aspects is so fundamental that their interactions have been termed the "Magic Triangle of Inkjet Printing".[123] The relationships are depicted in Figure 2.10. These processes determine

crucial mechanisms like the droplet ejection and transit to the substrate, the spreading of the ink after impacting on the substrate, and the end quality of the dried layer. Each one of these aspects will be discussed in the following paragraphs.

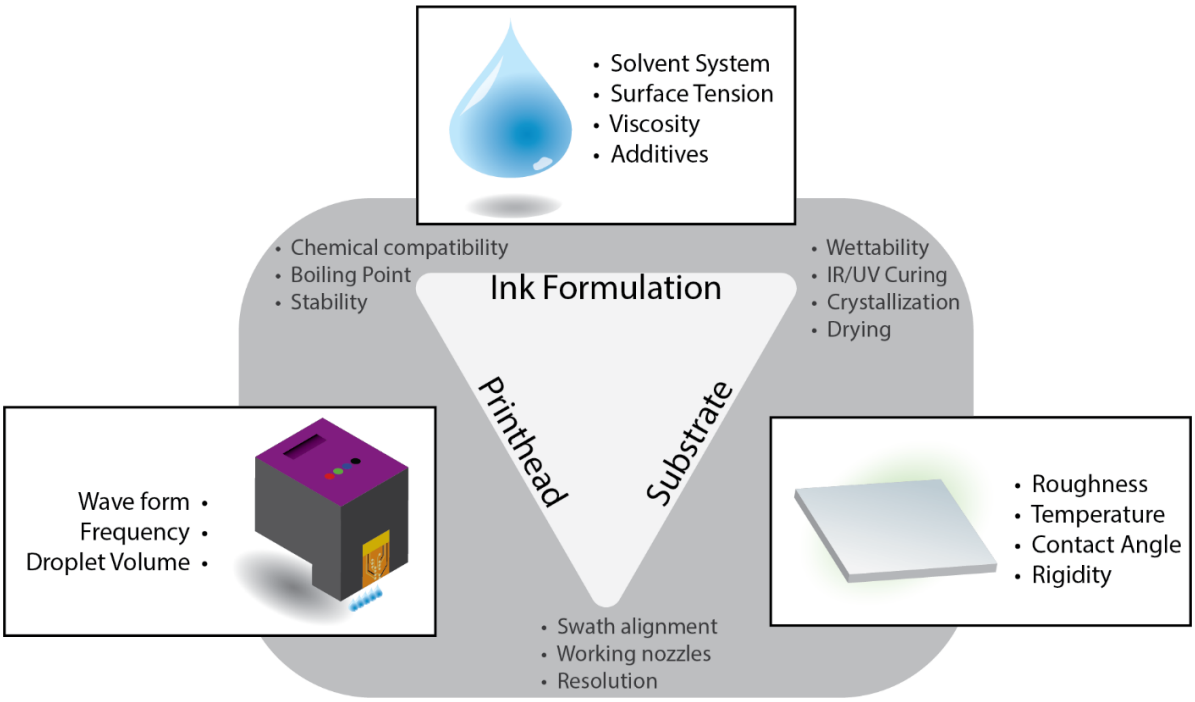

Figure 2.10. Triangle of inkjet printing, showing the interrelation between the ink properties, the printhead and the substrate.

The function of the printhead is to form droplets and position them accurately on the substrate. For this, ink at the reservoir is kept under a negative pressure to allow the nozzles to be filled with ink without dripping. An XY stage controls the movement of the printhead to accurately place droplets across the printing area. The formation of droplets is influenced by a moving piezoelectric, which adds kinetic energy to the ink. Here, droplets are only formed if the induced energy is larger than the surface tension of the ink. Additionally, the jetting frequency must match the acoustic response of the ink to avoid any destructive interference that would disrupt the jetting process. Ejected droplets should be fast enough to travel across a layer of air, usually in the range of meters per second. The resulting droplet speed is equivalent to the difference between the kinetic energy of the moving ink and its surface tension.

A waveform moves the piezoelectric inductors of the printhead to create jetting pulses, as shown in Figure 2.11. The movement of the piezo can be summarized in three stages.[124] First, the ink channel expands, inducing a negative pressure wave of intensity V_D which drives ink into the nozzle within a few microseconds, the rising time. Then, the channel remains expanded at V_D

during the dwelling time to allow the pressure wave to travel across the nozzle. Finally, the piezoelectric is relaxed and the channel is set back to its original position within the fall time.[125] Unipolar waveform cycles end here, however, residual acoustic oscillations can be removed using a bipolar waveform, where the piezo has two additional steps. In this case, the fall time is longer, and the piezo inductor drives the reduction of the channel. There is an additional pause t_{echo} to allow the pressure wave to move across the channel and finally the piezo is relaxed. When the timing and intensity of the pulses are synchronized with the ink, constructive interference results in the ejection of droplets. Changing the jetting frequency can also reduce the volume of the droplets on-demand. With this, droplets of large and small diameters can be printed simultaneously and the quality of the printed image as well as the perceived darkness of the image can be controlled. This technique is called *grey-scaling*.[126]

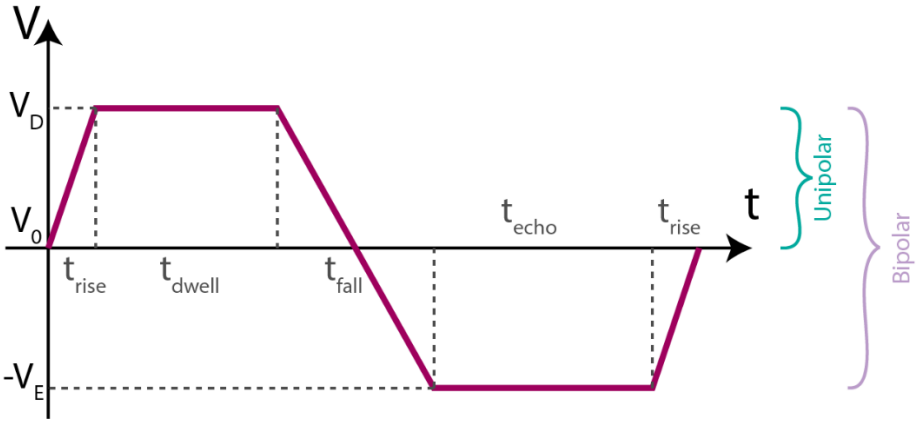

Figure 2.11. Diagram showing the change of voltage over time of the printhead as a waveform. The intensity and intervals of each one of the movement steps of the piezoelectric inductor are shown for a unipolar and a bipolar actuation pulse.

Jetted droplets should ideally be spherical. However, long tails can form due to a suboptimal waveform or from low viscosity inks, as shown in Figure 2.12. These tails can break into tinier droplets called *satellites*. The formation of satellites can reduce the quality of the print by creating rough edges. The severity of the defect depends on the type of printing that is pursued, especially when fine details are wanted. The influence of satellite droplets can be minimized if the printing process is performed with a printhead-to-substrate distance no greater than 1 mm.[127]

The solvent mixture of the ink can also introduce other types of challenges. For example, the chemical resistance of the printhead needs to be considered to avoid any damage triggered by the solvents. Additionally, low boiling point solvents in the ink can evaporate fast enough to clog the printhead nozzles during the printing process. When nozzles become clogged, some

printers offer the possibility of combining multiple nozzles to print single lines. This is called *quality factor*. With this, the layer homogeneity can be improved by reducing the effect of obstructed nozzles. The number of required swaths as well as the printing time to complete the printing process will increase by the same factor.

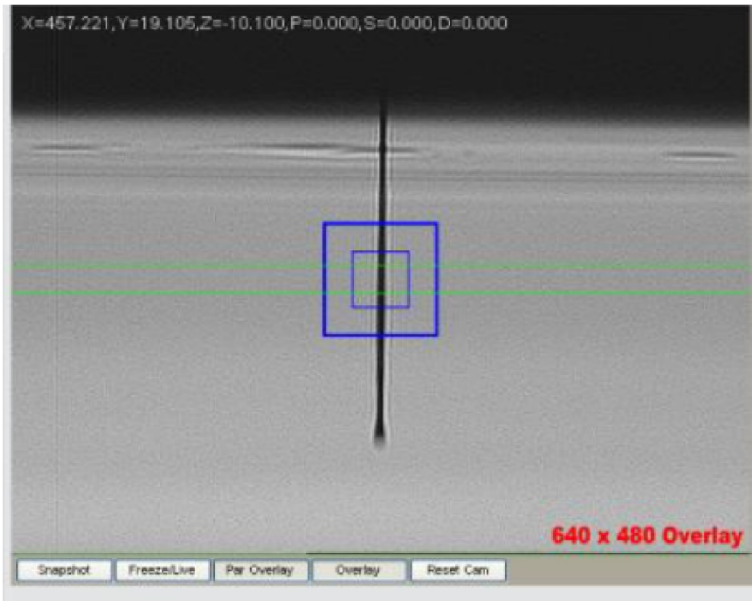

Figure 2.12 Dropview image of a single nozzle ejecting a droplet with a long tail. This tail can blend with the rest of the jet to form a single droplet or it can break into multiple droplets called satellites.

The ink is an essential part of the printing process since it constitutes the active material that will be deposited. An ink is defined by its density (ρ), viscosity (η_v) and surface tension (γ). In a flowing liquid, the propensity for turbulence is described by the Reynolds (Re) number, while the susceptibility of droplet formation is calculated by the Weber number (We), both of which are dependent on the aforementioned properties:

$$\mathrm{Re} = \frac{\nu\,\rho\,a}{\eta_v}\,, \tag{2.22}$$

$$\mathrm{We} = \frac{\nu^2\,\rho\,a}{\gamma}\,, \tag{2.23}$$

where ν is the droplet speed and a is the radius of the printing orifice, also called characteristic dimension. The jettability of a liquid is described by these two terms, which are encompassed by the Ohnesorge number (Oh). However, the inverse of the Ohnesorge number, the Z number, is more commonly used to describe the jettability as

$$Z = \mathrm{Oh}^{-1} = \frac{\mathrm{Re}}{\sqrt{\mathrm{We}}} = \frac{\sqrt{\rho\, a\, \gamma}}{\eta_v} \,. \qquad 2.24$$

Inks are more jettable, and hence easier to print, with a value of $1 < Z < 10$.[127,128]

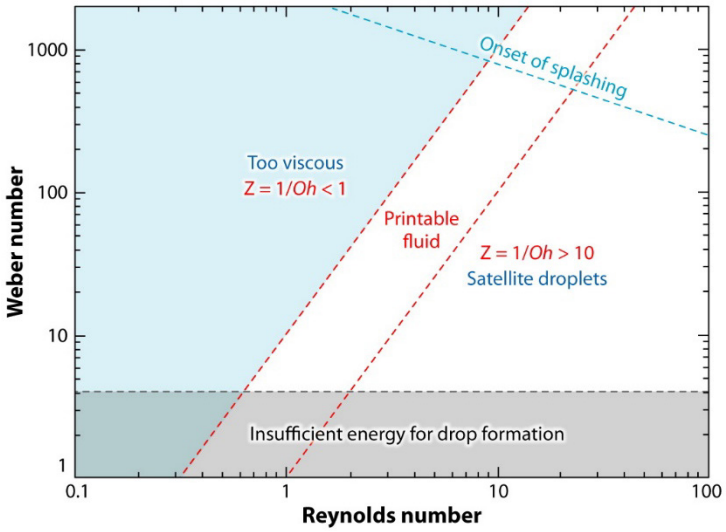

Figure 2.13. Visualization of a printable fluid, showing the relationship between Reynolds and Weber number for inkjet printable droplets. Taken from Ref. [127]**.**

The relationships between the Reynolds, Weber and Z numbers are visualized in Figure 2.13. A high Reynolds number is usually descriptive of a turbulent liquid, which would result in formation of satellite droplets. On the other hand, a small Weber number, with high surface tension, would result in an ink that cannot be jetted out of the nozzles. The ink properties can be finely tuned for ideal inkjet printing by changing the solvent system or using additives, thus altering the density of and viscosity of the mixture. Surfactants can also be used to modify the surface tension of the ink. Nevertheless, it should be noted that inks located outside the "printable fluid" area, shown in Figure 2.13, are still possible to be inkjet-printed. However, complications will appear when trying to increase the throughput of the printer by, for example, increasing the speed and jetting frequency of the printer. Complications include clogging of the nozzles during the printing process or formation of satellites droplets that can reduce the quality of the print.

Another crucial aspect to be considered are the interactions between the printhead and the substrate. For instance, the movement of the printhead must be correctly calibrated to avoid an offset between printed lines. Similarly, the density of the printed droplets, measured on drops

per inch (DPI), needs to be optimized. The lowest possible resolution is given by the nozzle distancing, also known as the *native resolution* of the printhead. The resolution can be increased in two main ways. The simplest is by increasing the number of swaths in between the nozzles distance. Also, printing can be done with the printhead to an angle, effectively reducing the spacing between the nozzles.[129] In any of these situations, the printing frequency and speed need to be re-adjusted, a task that is generally done automatically by the printer software.

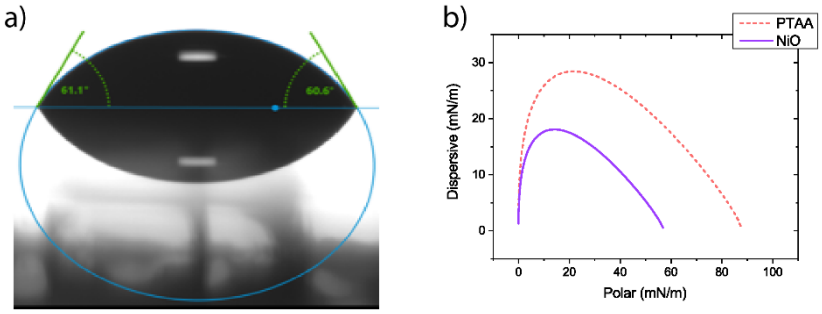

Figure 2.14. a) Picture of a contact angle measurement and plot of the b) wetting envelopes of PTAA and NiOx layers, used as HTLs for PV applications.

One of the main interactions occurs when the jetted droplet hits the substrate. Here, the kinetic energy of the drop is first dissipated by ink's viscous forces. Then, cohesive forces of the ink molecules, the so-called surface tension, equilibrate with adhesive forces from the substrate, so-called surface free energy, until a minimum free energy is reached.[130] This leads to a spread of the liquid across the substrate, forming a contact angle between the liquid and the substrate, as shown in Figure 2.14a. Additionally, the spread of the droplet is subjected to the roughness and temperatures of the substrate as well as the volatility of the ink. The contact angle is described by the Young equation as

$$\cos\theta = \frac{\sigma_{SV} - \sigma_{LS}}{\sigma_{LV}}\ , \qquad 2.25$$

where the interfacial energies are σ_{SV} between substrate and air, σ_{LS} between the droplet and substrate, and σ_{LV} between droplet and air. However, only θ and σ_{LV} can be known experimentally.[131]

There are multiple approaches to determine the surface free energy of the substrate, such as the Zisman, Fowkes and the Owens methods. On the Owens method, also known as Owens-Wendt-Rabel-Kaelble (OWRK) method, the ink and the substrate are assumed to have dispersion and

hydrogen-bonding (or polar) components.[131] Solvents with known polar and dispersive parts are used to determine the interfacial energies in the substrate by measuring their contact angle.[131] From this, it is possible to calculate all the possible combinations of polar and dispersion components of an ink, and the contact angle can be calculated.[132] This is known as the wetting envelope of the substrate and examples of them are shown in Figure 2.14b. In the same manner, the dispersive and polar parts of the ink can be measured to determine the wettability of the layers by the ink.

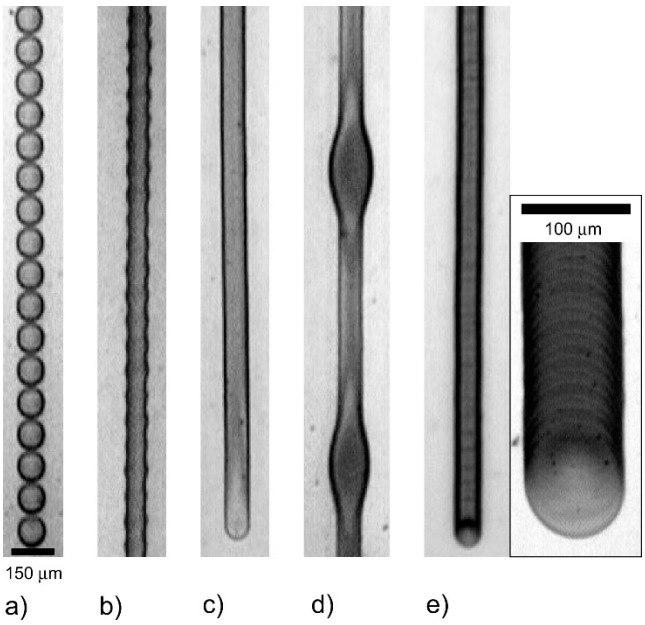

Figure 2.15. Behavior of inkjet-printed lines: a) disconnected line, b) scalloped, c) uniform, d) bulging, and e) stacked coins. Taken from Ref. [133].

The quality of printed lines depends on the drop spacing, delay periods and the temperature of the ink and the substrate. As shown by Soltman and collaborators in Figure 2.15, several effects can be achieved by fine tuning these values.[133] When droplets are printed to a distance larger than double the drop radius, the printed pattern becomes disconnected, shown in Figure 2.15a. At low temperatures, lines become wavy, or scalloped, as the drop spacing is reduced since the drops merge but cannot spread, as shown in Figure 2.15b. At one point, the droplets are separated to a degree where they merge flawlessly into a perfect line, shown in Figure 2.15c. As the droplet distance decreases, droplets start to accumulate in the substrate leading to a periodic bulging when the beads contact angle is exceeded, shown in Figure 2.15e. Droplets dry faster when the substrate temperature is raised, leading to a stacked coin pattern as shown in Figure 2.15e.[133] Furthermore, when depositing full areas, printing with a high resolution can lead to thick wet layers that are harder to dry, resulting in rough surfaces.

Once the wet layer has been successfully deposited, a phase change is necessary to fix the layer to the substrate and gain the physical properties of the material in the solid-state. Conductive layers are generally cured by UV or IR treatments.[134,135] Additionally, microwave and thermal treatments can also be used to quickly dry and compact the layers.[136,137] Some inks are dried in room conditions and the process can be accelerated with a steady stream of air which could also be thermally heated.[138]

Special Case of Perovskites

As mentioned in section 2.1.3, MHPs must not only dry, but crystallize in a specific way. The promotion of the crystallization process on perovskites is also called *quenching*. However, in this thesis the process will not be referred as such to prevent any confusion with the biomolecular quenching process that is discussed in Chapter 3 and will just be referred as the crystallization process.

Perovskites can be crystallized in a variety of ways. In the case for spin coating, the most popular deposition method in a laboratory setting, an antisolvent is applied at a specific moment to promote the crystallization of the layer. However, the addition of antisolvents is not compatible with inkjet printing due to difficulty in their removal after deposition. For this reason, other techniques have been developed. One of these techniques avoids the use of an antisolvent by separately depositing two precursor solutions, one after the other. After the first layer has been dried, the deposition of the second precursor reacts chemically with the first one, resulting in perovskite layers.[49] Other techniques focus on the removal of solvent after depositing the ink. For instance, infrared light has also been successfully used to create highly efficient solar cells.[45] Another technique uses a stream of nitrogen to slowly dry and enhance the crystallinity of the sample.[51] In a similar process, the material is crystallized by applying a vacuum around the sample, leading to high quality crystals after the procedure.[50]

In this thesis, we developed a novel technique that combines aspects of the two latter techniques. While applying a low pressure to the samples, a stream of nitrogen is used to enhance the crystallinity of the samples.

3 Photoluminescence Quenching Mechanisms in Perovskites

The content of this chapter is based on published work and includes some additional data.[139]

Unraveling Reversible Quenching Processes of O_2, N_2, Ar, and H_2O in Metal Halide Perovskites at Moderate Photon Flux Densities

E. R. Nandayapa, K. Hirselandt, C. Boeffel, E. L. Unger, E. J. W. List-Kratochvil

Adv. Opt. Mater., 2001317 (2020); DOI: 10.1002/adom.202001317

Contributions: E.R.N. and E.J.W.L.K. designed the experiments. E.R.N. prepared the samples, performed the sample characterization and analysis of the data with help of E.J.W.L.K. The manuscript was drafted by E.R.N. with advice and feedback from E.J.W.L.K. Furthermore, K.H. elaborated some of the samples and E.L.U. and C.B. contributed with the analysis of results and discussions.

3.1 Introduction

MHP devices have shown an unprecedent performance development in the past few years. However, the stability of these devices is still a challenge that needs to be addressed. Through the experiments described in this chapter, we study the effect that common gases found in the atmosphere have in the stability and performance of MHPs.

Specifically, the PL quenching effects caused by four atmospheric gases on MHP samples will be examined in this chapter. These gases were molecular oxygen, molecular nitrogen, argon, and water in the form of water-enriched argon. The change of PL emission on MHP layers of CsMAFA (see Section 2.1), also referred to as triple cation, was measured under increasing concentrations of the quenching gases. Additionally, the layers were analyzed under a constant flow of the gases to rule out any additional effects induced by the low-pressure conditions of the first experiment. Moreover, the role of boundary defects on the PL quenching process was studied by replicating the first experiment, where the sample is exposed to higher concentrations of quencher, in two ways. First, on crystals with a higher quality. Second, on MAPI samples in the form of a single crystal and polycrystalline layers. The Stern-Volmer analysis was later applied to the data to decode the PL quenching mechanisms of these gases on the MHP layers. Also, by using the PL lifetime information of the samples under different concentrations of the gases, additional details of the quenching mechanisms were determined.

3.2 Materials and Experimental Setup

Perovskite solutions were prepared with the following materials: Lead iodide (PbI_2) and lead bromide ($PbBr_2$) purchased from TCI chemicals. Formamidinium iodide (FAI), methylammonium iodide (MAI), and methylammonium bromide (MABr) purchased from Dyenamo AB, and cesium iodide from Abcr GmbH. The solvents dimethylformamide (DMF), dimethylsulfoxide (DMSO) and ethyl acetate (EA) were purchased from Sigma-Aldrich. All chemicals were used as received, without further purification.

The quenching gases used on this experiment were purchased from Air Liquide. The argon used was Alphagaz 2 Ar and contained <0.5 ppm-mol of water and <0.1 ppm-mol of O_2, total hydrocarbons (THC), CO, CO_2, and H_2. Nitrogen was Alphagaz 2 N_2 and had <0.5 ppm-mol of H_2O and <0.1 ppm-mol of O_2, THC, CO, CO_2, and H_2. Oxygen was N48, containing <2 ppmv of H_2O and <0.2 ppm-mol of THC, CO, CO_2. Custom versions of argon were prepared upon request by Air Liquide containing 10, 50, and 100 ppm-mol of H_2O and 5, 2 and 0.5 ppmv of N_2, O_2 and THC, respectively.

Microscope glass slides were used as substrates. After being cut to 1 in², the substrates were first brushed on mucasol (soap) diluted in deionized water to 2 vol.%. Consecutive sonication steps in soap diluted in water, deionized water, acetone, and isopropanol were performed for 15 minutes each. Finally, the substrates were cleaned using an ozone-plasma treatment for additional 15 minutes.

Sample Preparation

Stock solutions of PbI_2 and $PbBr_2$ were dissolved in DMF:DMSO (in a ratio of 4:1) to a concentration of 1.5 M. CsI was dissolved in DMSO at a concentration of 1.5 M. These solutions were shaken overnight at 60 °C. Later, FAI and MABr were dissolved at a concentration of 1.24 M using the PbI_2 stock solution with the former, and $PbBr_2$ with the latter, forming $FAPbI_3$ and $MAPbBr_3$, respectively. Finally, $FAPbI_3$, $MAPbBr_3$ and CsI were mixed with a volume ratio of 79:16:5.

The perovskite solution was spread onto the substrates and then spun at 4000 rpm for 35 s, with an acceleration of 5 seconds under nitrogen atmosphere. Ethyl acetate (EA) was applied as antisolvent 25 seconds after starting the process. The samples were then annealed for 45 minutes at 100 °C. Finished samples were stored in glass vials that were sealed under a nitrogen atmosphere for transportation. All layers had an average thickness of 600 nm. SEM images as well as an XRD diffractogram of a typical layer are shown in Appendix 7.2.

Sample Characterization

The samples were characterized using the FLS980 Spectrometer from Edinburgh Instruments at a temperature of 300 K. PL emission and PLQY measurements used a 450 W xenon arc lamp while PL lifetime measurements used a picosecond pulsed diode laser EPL-510 with a pulsing period of 10 µs. PL emission was recorded at 760 nm for triple cation and 780 nm for MAPI samples.

Measurements at Low Pressures

Samples were briefly exposed to air before placing them into the spectrometer. Once the samples were secured into a cryostat, pure argon was flushed into the chamber for 10 minutes. Then, the chamber was evacuated to 0.02 mbar and refilled with argon three times to ensure inert conditions. Measurements were performed afterwards, at pressure values of 0.02, 0.1, 0.3,

1, 3, 10, 30, 70, 100, 300, 700 and 1000 mbar. The integral PL intensity was tracked for 2 minutes at each pressure level.

Measurement at Atmospheric Pressures

For the measurements performed under a constant flow of gas, the sample was fixed into the cryostat. Argon was flushed into the chamber for 10 minutes to ensure inert conditions. The integral PL was then measured under the same flow of argon for 6 minutes. The flow was then immediately switched to either molecular oxygen, molecular nitrogen, or water-enriched argon while the measurement continued for 6 minutes. Finally, the flow of argon was returned while tracking the PL changes for 6 more minutes. The overpressure of the flow was kept under 2 mbar.

PLQY Measurements

Quantum yield measurements were performed by the "direct excitation" method using an integrating sphere. For this, two samples with a size of 1 cm^2 were needed. The first one was a reference sample that consists of a clean substrate. The second one was the sample containing the test MHP layer. These samples were cut to the required dimensions after having been deposited by the standard procedure.

Four measurements were then performed with the FLS980 spectrometer. These were separated measurements of the scatter and the emission spectral regions of the reference and the sample, respectively. Due to the low emission of these samples, the scatter regions were measured using a 10 % neutral density filter while no filter was used for the emission region. The scatter region was then appropriately scaled. The absolute fluorescence quantum yield was calculated using eq. 2.15.

PL Lifetime Measurements

PL lifetime measurements were performed in a similar fashion to the "Measurements at Low Pressures" (see above), at pressures of 0.02, 0.1, 1, 10, 100 and 1000 mbar. In this case, the light source was changed to a pulsing laser EPL-510 with a pulsing period of 10 μs. These measurements can take a few hours to accomplish. For this reason, to ensure that the atmosphere

inside the cryostat kept to the desired levels, the measurement at the lowest possible pressure of 0.02 mbar was performed under an active vacuum. For a pressure of 0.1 mbar, the gas flowed inside of the chamber and was regulated with an active vacuum until the pressure was achieved. All other pressure measurements were performed with the cryostat closed as soon as the desired pressure was reached.

The power of the lamp and the laser were measured with a Thorlabs PM100A power meter. The mean photon flux densities of these sources are shown in Figure 3.1. All the measurements were performed with a light intensity below 10^{19} photons s^{-1} m^{-2}.

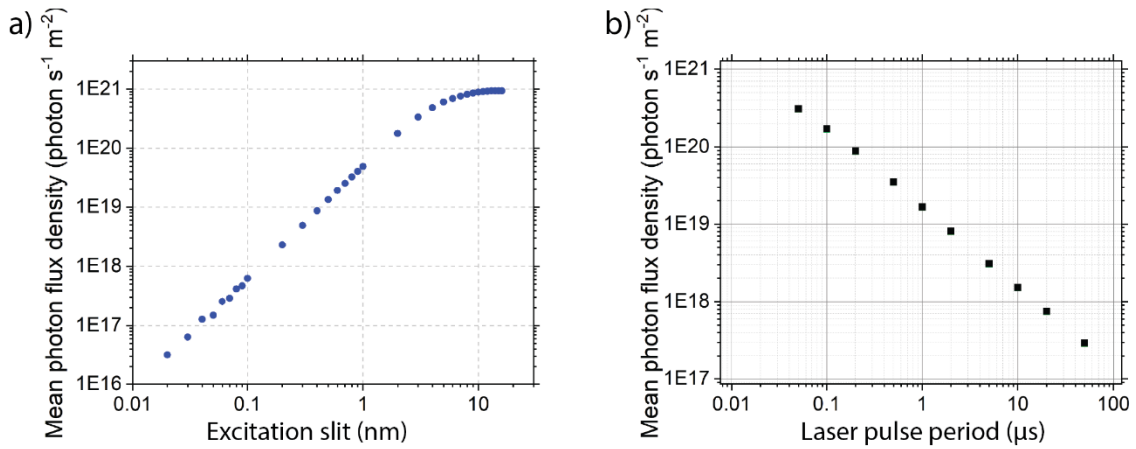

Figure 3.1. Mean photon flux density a) of a xenon lamp at 510 nm with different slit apertures and b) a 510 nm laser at different pulsing times.

Other supportive characterization, like scanning electron microscopy was done using a S4100 microscope, by Hitachi and a cold emission gun. Carola Klimm, of Helmholtz-Zentrum Berlin, made these characterizations. X-ray diffraction was done by Carolin Rehermann, of Helmholtz-Zentrum Berlin, in air with a Bruker D8 Advance, using Bragg Brentano geometry and a Cu K-alpha anode.

3.3 PL Quenching of Atmospheric Gases

In this section we describe four experiments designed to test the PL quenching efficacy of the test gases. Additionally, the role that boundary defects play in these processes is determined using CsMAFA and MAPI layers.

3.3.1 PL Quenching at Low Pressures

As mentioned in Section 2.3.4, the PL emission of a semiconductor will reduce in the presence of quenchers. This effect is displayed in Figure 3.2, where the change on PL emission of triple cation perovskite layers is recorded while increasing concentrations of quenching gases are added. Starting from a 0.02 mbar pressure – which we call the vacuum condition – gases were individually added into the chamber at discrete pressure values of 0.1, 0.3, 1, 3, 10, 30, 70, 100, 300, 700 and 1000 mbar. The integral PL was then tracked for 2 minutes at each pressure level.

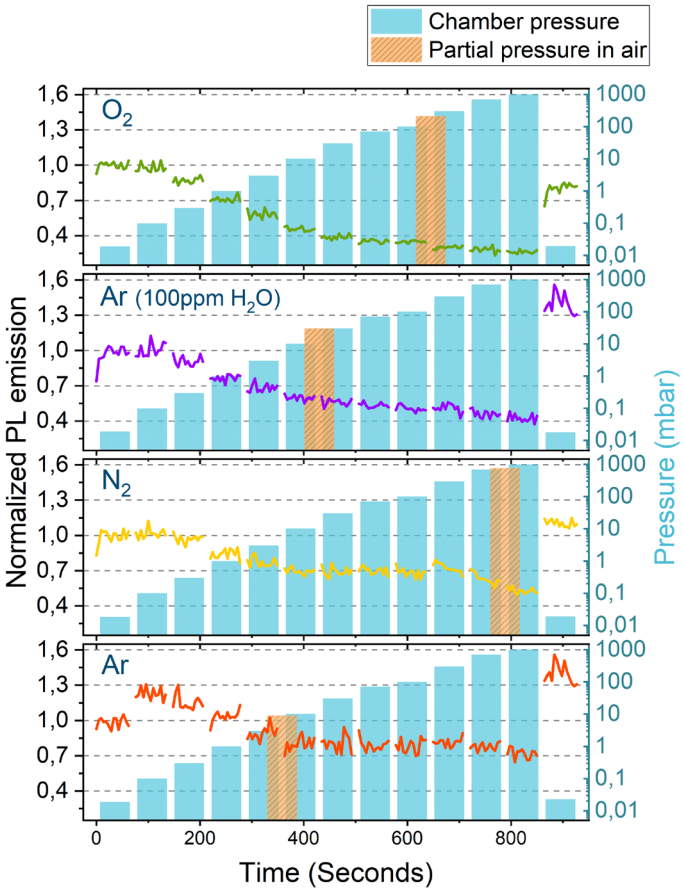

Figure 3.2. Change of emission intensity of a perovskite layer under atmospheres of O_2, H_2O, N_2 and Ar. All emission curves are normalized to the first measurement of the pristine sample. Columns show the pressure value of each emission curve. Orange columns represent the partial pressures of oxygen, water-enriched argon, nitrogen and argon in atmospheric air at 210, 30, 781 and 9 mbar, respectively.[139,140].

The strongest quenching effects are measured with oxygen and water-enriched argon, while nitrogen and pure argon show a weak effect. In particular, oxygen shows a strong decrease in emission of about 10% and 30% at pressures of 0.3 and 1.0 mbar, respectively. PL intensity continues to reduce as oxygen is added, reaching a minimum of 26% at 1000 mbar. Similarly,

water-enriched argon shows a strong and steady PL quenching effect, although not as strong as with oxygen. The lowest PL emission of 37% is reached when the chamber is full at 1000 mbar. By the same token, molecular nitrogen also results in a notable quenching effect. PL emission decreases by 15% at a pressure of 1 mbar, reaching a minimum of 51% when the chamber is full at 1000 mbar of pressure. Finally, argon also presents a weak but clear quenching effect. At low pressures of 0.1 and 0.3 mbar, there is a small enhancement of PL, but it rapidly turns around. A minimum emission of 66% of that from the pristine sample is reached at 1000 mbar. Furthermore, all samples showed a recovery of PL emission when returned to vacuum conditions. In the case of oxygen, PL recovered to only 80% of that from the pristine sample. All other conditions resulted in a slight enhancement.

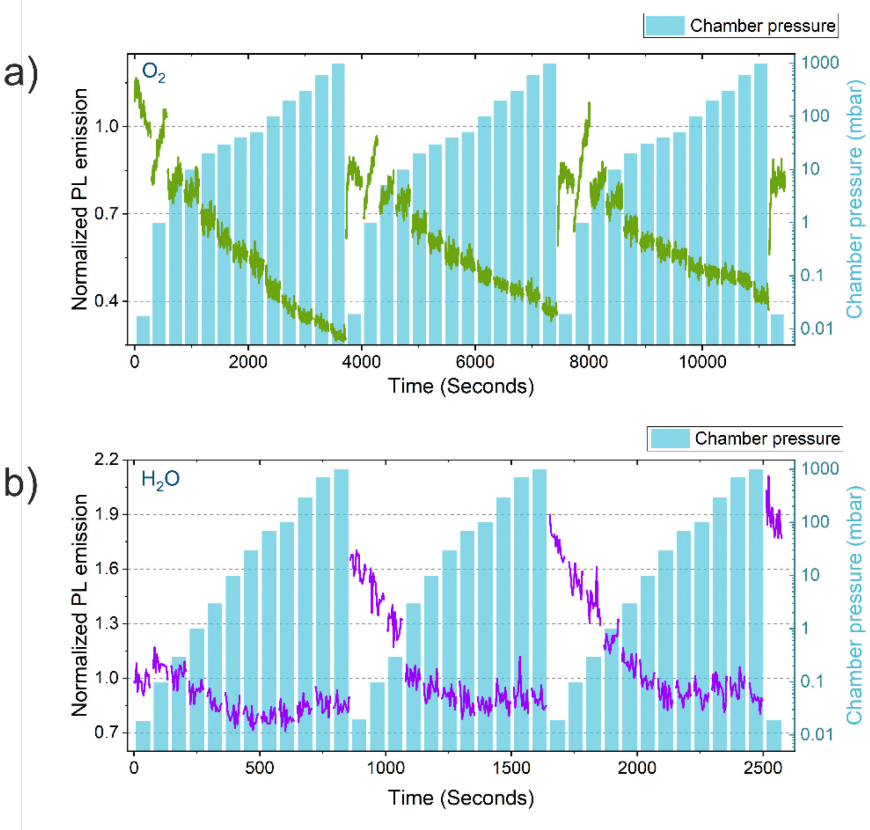

Figure 3.3. PL emission of triple cation perovskite samples exposed to a) oxygen and b) water-enriched argon for 3 consecutive cycles.[139]

These results demonstrate that argon and nitrogen, gases commonly regarded to have a low chemical reactivity, are indeed interacting photo-physically with the perovskite crystals. Additionally, there is evidence that passivation effects are being induced by the quencher molecules since PL emission is enhanced once the exposed sample is returned to vacuum conditions. In like manner, the partial recovery of the sample exposed to an oxygen atmosphere

indicates a binding of the oxygen molecules to the perovskite crystal. The general discussion of these results will continue in Section 3.5.

In an additional experiment, the PL emission recovery of the samples was examined by repeatedly exposing them to incremental concentrations of the same quencher, as shown in Figure 3.3. For this experiment, CsMAFA layers were exposed to the gases that showed the strongest quenching effects, oxygen, and water-enriched argon. Similarly to the first experiment, the PL intensity was recorded as the concentration of the gases was increased in discrete steps starting from a vacuum all the way to 1000 mbar for three consecutive cycles.

After the first cycle of oxygen addition, there was a reduction of PL emission of 20%. This reduction remained constant for two additional cycles. Moreover, there was an unusual behavior at a pressure of 1 mbar, where the PL emission rapidly increased. The reason for this effect is unknown and was recorded only on some of the measured samples under oxygen. On the other hand, water-enriched argon showed an increment of PL intensity in the vacuum after the first cycle. Further cycles increased the PL emission even more at vacuum conditions. However, subsequent pressure steps remained within 10% of the value from the previous cycle at the same pressure value. Considering the negligible emission change during subsequent cycles of quencher addition, we dismiss any immediate degradation of the perovskite crystals induced by oxygen or water.

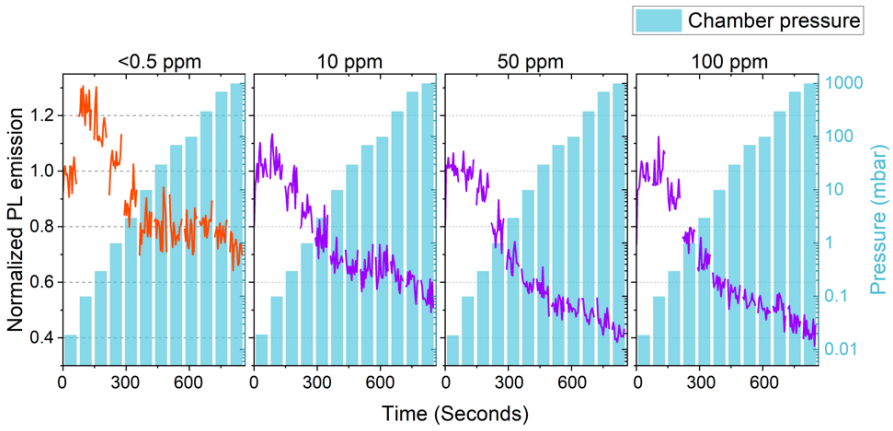

Figure 3.4. PL change of triple cation perovskite samples exposed to argon with different water concentrations.[139]

Finally, as a reference, four different concentrations of water in argon were tested for the water condition of these experiments. Namely, concentrations of <0.5, 10, 50 and 100 ppm of water

in argon. Similar to the first experiment, samples were exposed to incremental concentrations of each version of the gas while the PL intensity was recorded, as shown in Figure 3.4.

These results show a prominent reduction of PL emission for all water concentrations. However, the effect reaches a maximum at 50 and 100 ppm of water in argon. For this reason, to ensure the effect of water in all the measurements, the experiments were performed with the gas containing 100 ppm of water in argon and it is referred to as water-enriched argon.

3.3.2 PL Quenching at Atmospheric Pressures

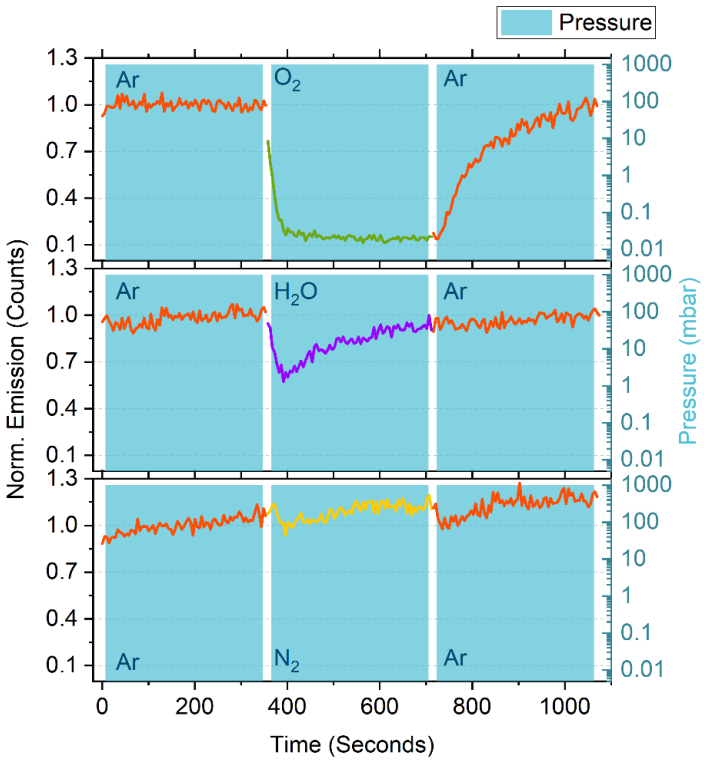

Figure 3.5. PL emission changes of triple cation perovskite layers under constant flows of argon, oxygen, water-enriched argon (H_2O) and nitrogen. Each gas flowed inside of the chamber for 360 seconds. Oxygen showed the strongest PL quenching effect. Water also showed a substantial quenching, however the PL intensity quickly recovered to pristine conditions while the gas was still flowing in the chamber. On the other hand, the effect of nitrogen is barely perceptible.[139]

Due to the existence of volatile components in the perovskite lattice, it has been shown that low pressure conditions can induce lattice changes at the surface and bulk of the perovskite crystallites, and with this, the photophysics of the crystal.[141,142] To determine the extent and influence of this effect in our measurements, perovskite layers were separately exposed to the

quenching gases under a constant flow at 1 atm pressure. Argon was used as a control condition since it showed the lowest level of quenching in the previous experiments.

The experiment consisted of 3 steps. First, argon was flushed into the chamber for 10 minutes to achieve inert conditions. Then, the sample was illuminated while the PL emission was recorded for 6 minutes. Next, the flow was swiftly changed to either oxygen, water-enriched argon, or nitrogen for additional 6 minutes. Finally, the gas flow was changed back to argon for 6 minutes more. The resulting changes in PL emission can be seen in Figure 3.5.

All samples showed a constant PL emission under the first flow of argon. When oxygen was added into the chamber, a sudden decrease of emission was recorded, down to 13%, and stayed constant for the remaining time. As soon as the flow was shifted back to argon, the PL emission started to recover slowly. Similarly, the addition of water-enriched argon resulted in a sudden decrease of intensity to 57%. However, here PL emission rapidly recovered to the pristine levels while the gas was still flooding the chamber. When pure argon was added back into the chamber, there were no noticeable change since the PL emission was already at the same intensity as pristine conditions. For our last test, an almost imperceptible PL emission decrease of about 10% was registered when nitrogen was added into the chamber. This change rapidly stabilized back to pristine conditions. Another subtle decrease was detected when chamber flow was shifted back to argon, which quickly stabilized back to pristine conditions was well.

The PL quenching effects of oxygen and water-enriched argon in this experiment were analogous to the ones obtained in the last one. This shows that the volatility of the crystal components does not strongly influence the procedure performed under low-pressure conditions.

Particularly, the effect of oxygen is consistent with the results of the previous Section. In the case of water-enriched argon, however, there is an unusual behavior where there was a quick recovery of PL intensity after the sudden reduction. This effect is related to the charge transfer mechanism occurring with the water molecule and will be discussed in detail in Section 3.5.2. In the case of argon and nitrogen, there was a weak reduction of PL emission when moving from one gas to the other and vice versa. As discussed in Section 3.3.1, both gases weakly quench the PL emission of the perovskite. Here, however, the perovskite layer was already quenched by argon, so the PL emission change when shifting to a nitrogen atmosphere was also weak, shown as a small dip of about 10% of the tracked PL intensity in Figure 3.5.

3.3.3 PL Emission and Quantum Yield

To study the influence that lattice defects on the perovskite crystals have on the quenching efficacy of the gas molecules, the initial experiment from Section 3.3.1 was repeated on a higher quality crystal. These higher quality crystals were achieved by changing the vial cap materials used to store the perovskite solutions. We found that ink solutions that were stored on vials with PTFE septums yielded layers with a higher PLQY, a signature of crystal quality. All the other samples had been prepared with solutions that were stored with natural rubber septums. The more chemically resistant PTFE reduced the amount of foreign material contaminating the perovskite solution and increased the quality of the crystals.

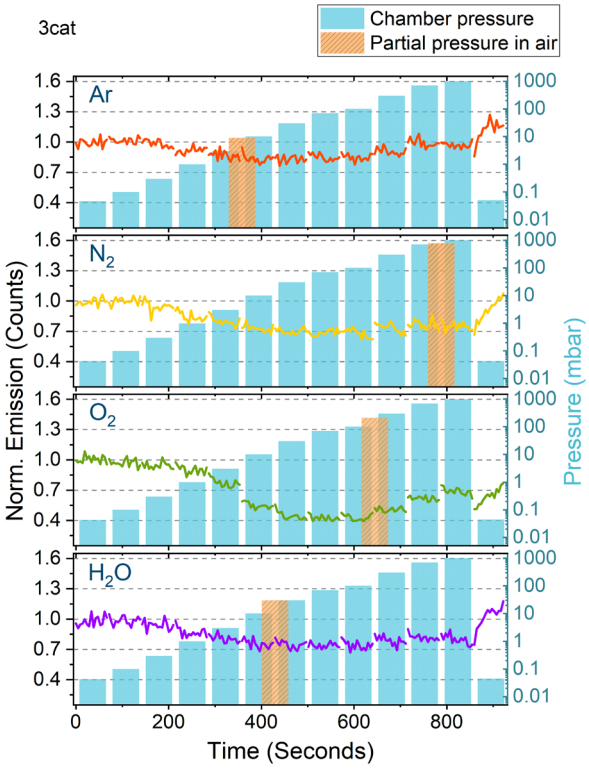

Figure 3.6. Effect of quenching gases – argon, nitrogen, oxygen, and water-enriched argon (H_2O) – in the PL emission of triple cation perovskite layers having a higher quality layer with an 8.4% PLQY.

Figure 3.6 shows the PL quenching effect of the gases on higher quality layers with a PLQY of 8.4%. For reference, the samples with a lower crystal quality showed a PLQY of 3.1% and further details are found in Appendix 7.1. In general, the results are comparable to our earlier results. Oxygen and water-enriched argon show a maximum quenching of 60% and 30%, respectively, as compared to 74% and 63% obtained from the lower quality sample.

Furthermore, the recovery at vacuum conditions after having added incremental concentrations of quencher is still proportional to the ones shown in lower quality layers.

The main difference found on these higher quality layers is that passivation effects are enhanced. Specifically, all gas conditions show a minor increase of PL emission at pressures higher than 100 mbar. However, this passivation is not strong enough to regain the PL emission of a pristine sample.

3.3.4 PL Emission and Boundary Defects

MAPI is one of the most characterized perovskite-types out there. There is a large variety of publications discussing the effect of atmospheric gases on MAPI.[143–147] For this experiments, MAPI was chosen because, although the growth of single crystal CsMAFA is possible,[148] the processing of MAPI is simpler. The aim of this experiment was to study the effect that surface area and boundary defects have on the quenching mechanisms of the gases by comparing their effect on polycrystalline and single crystal MAPI samples.

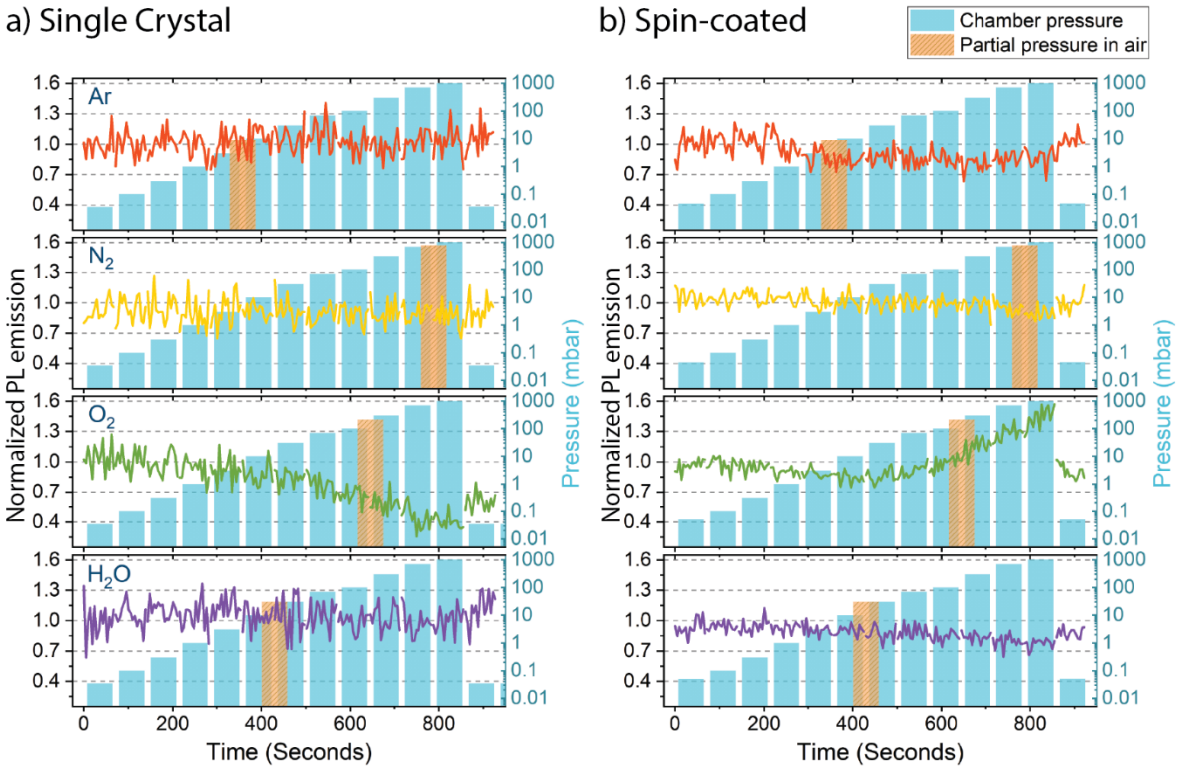

Figure 3.7. Change on PL induced by argon, nitrogen, oxygen, and water-enriched argon (H_2O) on a) a single crystal of MAPI and b) a polycrystalline spin-coated sample of MAPI.

Figure 3.7 shows the effects that the test gases had on 2 different types of MAPI samples. The first was a single-crystal MAPI that was grown by heating a supersaturated solution until crystals grew to a dimension of ca. 5 mm, as described in Ref. [149]. The second sample was spin-coated using a DMSO based solution, as described in Ref. [70]. These samples were prepared by different colleagues upon request, and hence complementary characterization is limited.

When looking at the data from the single crystal MAPI, a steady PL emission is shown under atmospheres of argon, nitrogen, and water. Oxygen, on the other hand, showed a clear reduction of PL intensity with increasing concentrations of the gas. The PL emission reduction is clear at a pressure of 1 mbar. The emission continued reducing to a minimum of 40% at 1000 mbar. There was a small recovery of PL at vacuum conditions to 60% of the initial PL, similar to what was shown on the polycrystalline triple cation samples.

On the other hand, the spin-coated samples showed a contrasting behavior. The PL quenching effect of argon, nitrogen, and water was not so pronounced as with the triple cation but still noticeable. In particular, the argon atmosphere showed a clear reduction of PL at pressures above 1 mbar that reached a minimum of ca. 75%. Similarly, water showed a noticeable reduction at pressures above 1 mbar, which reached a minimum of about 70% of the initial PL. On the other hand, the effect of nitrogen was noticeable only at higher pressures, where a minimum of about 85% of the PL was reached at pressures above 300 mbar. Oxygen showed the strongest PL change. First, a small PL reduction to about 80% at 10 mbar is noticeable. Then, the PL increased rapidly, reaching a maximum of 150% of the pristine condition, as it approached 1000 mbar. Recovery was not so evident as the samples were returned to vacuum conditions. Water and oxygen showed even a small degradation, with a recovery of only ca. 90% for water and ca. 86% for oxygen once they were in vacuum conditions.

The PL change differences between the single crystal and polycrystalline samples were prominent. Small quenching effects were noticeable on the polycrystalline sample for argon, nitrogen, and water. For oxygen, on the other hand, the strong increment of PL intensity points towards passivation effects. This phenomenon has been widely discussed in the literature, having shown evidence that the PL increment occurs due to oxygen binding to iodine vacancies and passivating these defects.[143] Nevertheless, the reduction of PL emission in vacuum conditions after the sample was exposed to oxygen is also a sign of the diffusive effect of oxygen, which permanently quenches the PL by a small fraction once it is absorbed into the surface and the bulk.[150]

When comparing these results to the ones of the single crystal, it is clear that boundary defects play a crucial role on the PL quenching process of the gases due to the bulk to surface-area ratio. With exception of oxygen, all the gases showed no visible change on the PL emission of the single crystal. This happens because diffusion lengths of perovskites, which can be as long as few microns,[88] are much shorter than the crystal size, with a side of ca. 5mm. Even when gases bind to the crystal, recombination at the bulk occurs before the charges can reach the quenchers. In the case of oxygen – a well-known quencher[151] – the known binding mechanism to iodide vacancies makes it a more efficient quencher.[152]

As a quick summary of the experimental results discussed in these sections, the experiments showed that the quenching effect of all molecules was mostly reversible. Oxygen showed the strongest PL quenching effect of all tested molecules. Additionally, oxygen appears to bind into the perovskite lattice since the PL emission intensity of all samples decreased once they were back at vacuum conditions after having been exposed to oxygen. It was also shown that a water concentration of 50 ppm or larger displayed no further differences on its quenching effect. The immediate degradation of the perovskite crystals by oxygen or water was dismissed due to negligible differences on consecutive cycles of quencher addition. Under a constant flow, oxygen showed a stable quenching effect while water showed an immediate and gradual recovery of PL intensity after a sudden decrease when the gas was introduced to the chamber. In the case of high-quality layers, passivation effects were noticeable for all molecules. However, the amount of PL quenching was comparable to the one shown in the lower quality crystals. Finally, the role that boundary defects play on the PL quenching effect of the molecules was revealed by comparing their behavior in a single crystal and polycrystalline layers of MAPI. All these results will be brought in the next section into perspective to determine the quenching mechanisms to the quencher molecules.

3.4 Stern-Volmer Analysis

The Stern-Volmer (SV) analysis is a standard procedure to study bimolecular quenching in molecules, as explained in Section 2.3.4. The SV method had not been previously used in perovskites, since the procedure is more common for organic molecules suspended in solution. However, this type of analysis can also be applied to perovskites because at room temperature,

photogenerated charges in MHPs occur as free charges if the excitation density remains below the trap density and can be transferred to a quencher.[153,154]

The light intensities used in our experiments correspond to an excitation density below 10^{16} cm^{-3}, which is within the reported trap density of MAPI and triple cation perovskites.[155,156] As described by eq. 2.2 in Section 2.3.4, the predominant recombination occurring is of the monomolecular type in our samples. However, PL quenching involves two separate compounds. That is, photogenerated charges in the perovskite crystals and the quenchers, making it a bimolecular process.

In this section, the term "bimolecular recombination", or quenching, will be used to refer to the charge transfer between a photoexcited material and a quencher, and not to the standard bimolecular recombination process that occurs band-to-band within the semiconductor.

3.4.1 SV Analysis: PL Emission

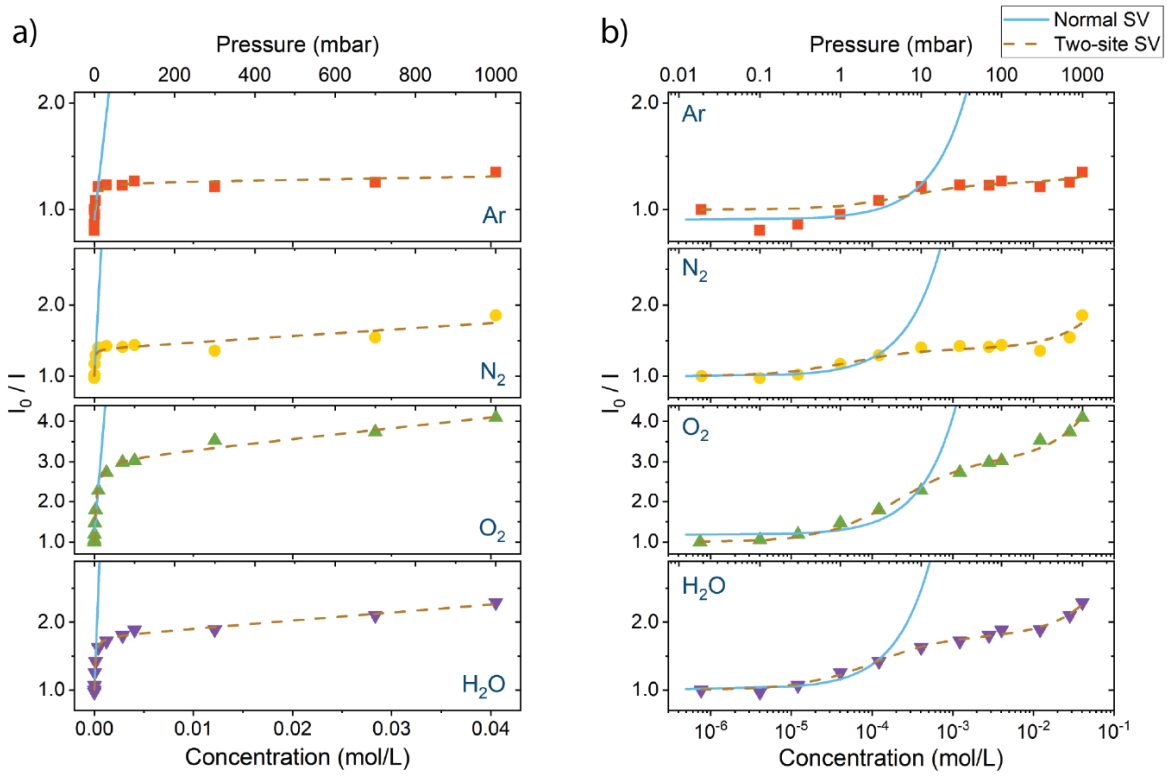

Figure 3.8. Stern-Volmer plot of PL emission of perovskite layers exposed to oxygen, water-enriched argon, nitrogen, and argon. Blue line corresponds to the standard SV model while dashed golden line corresponds to the Two-site model. Figure b) shows the same data but with x-axis on a log scale to make details easier to the eye.[139]

By applying equations 2.19 and 2.21 to the data shown in Figure 3.2, the results depicted in Figure 3.8 are obtained. It should be noted that the data shown in these two plots are the same. Figure 3.8b shows the x-axis in a log-scale to enhance the visibility of figure a. In these plots it is shown that all data points below 10 mbar are well fitted by the Standard SV model, shown as a blue line and resulting from fitting the data with equation 2.19. On the other hand, the data is well described throughout all the pressure range by using the Two-site SV model, from equation 2.21 and shown as a dashed golden line.

The fitting values for these equations are shown in Table 3.1. For the Standard Model, the SV constant (K_{SV}) refers to the slope of the blue curves shown in Figure 3.8. Here, water-enriched argon shows the largest value of 3625, closely followed by oxygen and nitrogen. Argon has a slope value of 811.7, which is 4.5 times smaller than that of water.

On the other hand, the Two-site model contains two SV constants. It is not intuitive to interpret these results as slopes, however, the fractional number of quenched emitters, f_{01} and f_{02}, can be used to weight the two SV constants into a single one to have a direct comparison between both models. In this sense, oxygen has the largest SV constant of 10 037, followed by water and nitrogen. Argon, in comparison, has a small constant value of 946.5, which is 10.6 times smaller than the one from oxygen.

Table 3.1. Table 1. Fitting parameters resulting from applying the Standard (eq. 2.19)and the Two-site (eq. 2.21) SV models to the data shown in Figure 3.2.

	Standard Model	Two-site Model				
	K_{SV}	f_{01}	$K_{SV,1}$	f_{02}	$K_{SV,2}$	$K_{SV\text{-}WA}$ [a)]
Ar	811.7	0.20	4728.0	0.80	1.17	946.5
N_2	2584.2	0.28	26748.1	0.72	6.58	7494.2
O_2	2953.7	0.67	14975.9	0.33	8.59	10036.7
H_2O	3625.2	0.44	17303.2	0.56	6.54	7617.1

[a)] Weighted arithmetic mean

Furthermore, the accessed fraction of emitters by the quenchers (f_{01} and f_{02}) can be used to determine the location in the crystal where the PL quenching occurs. As described in Section 2.3.4, the Two-site model divides the quenching sites into two: one “easy to quench” at the surface and the other “difficult to quench” at the boundary defects. For instance, the f_{01} values of oxygen and water indicate the 67% and 44% of all emitters were “easily” quenched at a low

pressure, as shown in Table 3.1. On the other hand, the f_{02} values of nitrogen and argon state that 72% and 80% of the emitters were quenched at higher pressure values, suggesting that quenching occurs mostly at the harder to access boundary defects. Considering that these results can be fitted with the standard model for a pressure of up to 10 mbar, we use this value as the breaking point between low and high pressure. In the same manner, there are signs of quencher saturation since the quenching rate dramatically slows down at pressures higher than 10 mbar for all gases.

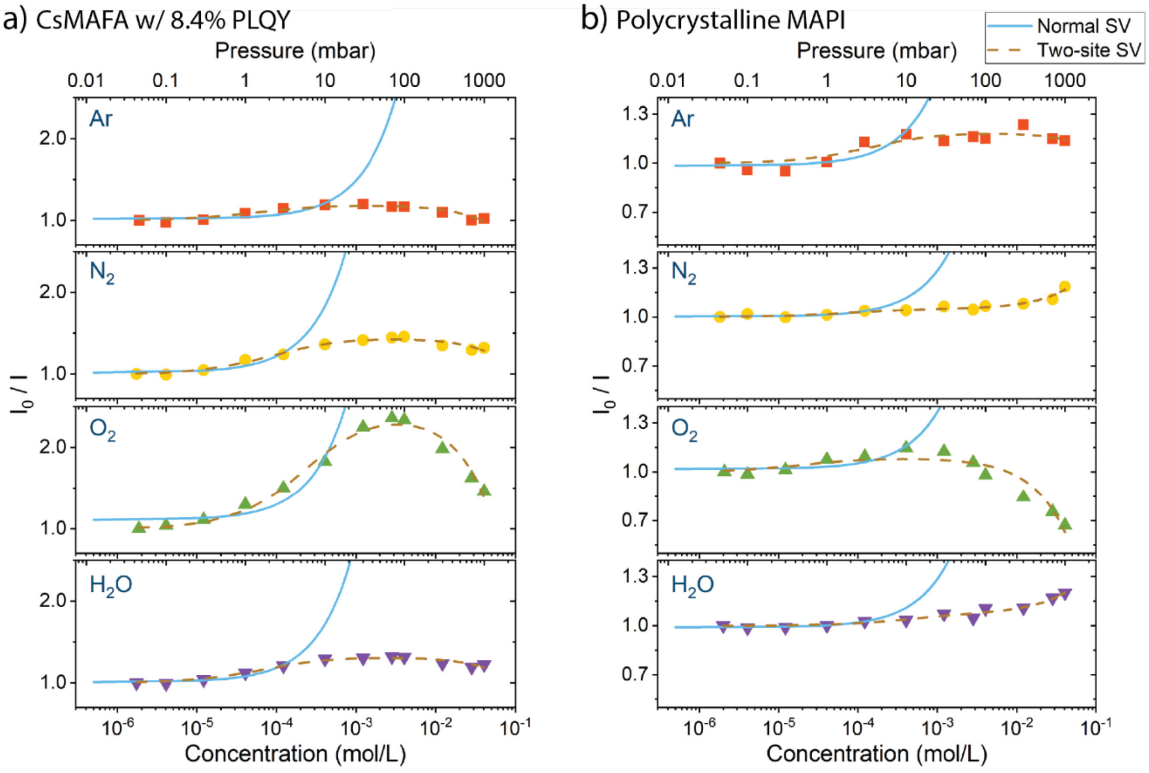

Figure 3.9. SV Plots with the x-axis in a log scale of a) the CsMAFA sample with a higher quality crystal from Section 3.3.3 and b) the polycrystalline MAPI from Section 3.3.4. The behaviors are compatible to the ones shown in Figure 3.8.

The SV values obtained from both models are mostly in agreement with each other. For example, argon and nitrogen had the lowest SV constants in both cases. However, it is important to keep in mind that the Standard model only fits the initial part of the data, while the Two-site model does for the whole extent of it. Additionally, the Two-site model goes a step forward and provides useful information about the fast and slow quenching components which can also be used to find the quenching location on the perovskite crystals.

For reference, the $K_{SV\text{-}WA}$ refers to a normalized weighted arithmetic mean.[157] Here, the $K_{SV,1}$ & $K_{SV,2}$ values are weighted with respect to f_{01} & f_{02} in the form

$$K_{SV-WA} = \frac{\sum_{i=1}^{n} f_{0i}\, K_{SV,i}}{\sum_{i=1}^{n} f_{0i}} \rightarrow \frac{f_{01}\, K_{SV,1} + f_{02}\, K_{SV,2}}{f_{01} + f_{02}}, \qquad 3.1$$

where the resulting $K_{SV\text{-}WA}$ is a value that unifies the faster and slower coefficient components into one for easy visualization of the trends.

Table 3.2. Fitting parameters of Standard and Two-site models to the data collected on the CsMAFA sample with a higher quality crystal and the polycrystalline MAPI samples.

		Standard Model	Two-site Model				
		K_{SV}	f_{01}	$K_{SV,1}$	f_{02}	$K_{SV,2}$	$K_{SV\text{-}WA}$ [a)]
CsMAFA 8.4% PLQY	Ar	470.5	0.16	21862.2	0.84	-4.3	3494.4
	N_2	2016.7	0.30	16403.3	0.70	-2.8	4919.1
	O_2	1912.7	0.59	10849.5	0.41	-10.8	6396.8
	H_2O	1755.2	0.25	19844.6	0.75	-2.4	4959.3
Polycrystalline MAPI	Ar	529.6	0.15	8598.1	0.85	-0.9	1288.9
	N_2	279.4	0.05	15152.7	0.95	2.8	760.3
	O_2	384.7	0.08	54637.7	0.92	-10.4	4361.5
	H_2O	294.1	0.07	2533.0	0.93	2.9	180.0

Moreover, the SV plots of the samples with a higher PLQY discussed in Section 3.3.3 and the polycrystalline MAPI discussed in Section 3.3.4 are shown in Figure 3.9 along with the fitting parameters in Table 3.2. In general, the results are comparable to the ones obtained previously in Figure 3.8. One of the main differences is shown in Table 3.2, where $K_{SV,2}$ values are negative due to passivation effects.

The bimolecular recombination values k_q of each one of the quenching molecules are shown in Table 3.3. The resulting recombination coefficient of all gases are below the diffusion-controlled limit of 10^{10} M^{-1} s^{-1}, meaning that the quenching processes are not efficient.[158] The value for argon is one order of magnitude lower than the rest for both models. In the case of oxygen, our measured value is consistent with what has been measured in other dyes and organic molecules, like P3HT.[106,107] Notwithstanding, these constants have not been measured for water, nitrogen or argon in any other solid materials.

Table 3.3. Bimolecular recombination values for the Standard and the Two-site model.

	Normal model		Two-site model	
	K_{SV} [M^{-1}]	k_q [$M^{-1}\,s^{-1}$]	K_{SV} [M^{-1}]	k_q [$M^{-1}\,s^{-1}$]
Ar	811.7	4.90×10^8	946.5	5.72×10^8
N_2	2584.2	1.56×10^9	7494.2	4.53×10^9
O_2	2953.7	1.78×10^9	10036.7	6.06×10^9
H_2O	3625.2	2.19×10^9	7617.1	4.60×10^9

3.4.2 SV Analysis: Temperature

By exposing the samples to increasing concentrations of quencher at a higher temperature, it is possible to use the Stern-Volmer analysis to determine the type of quenching that is occurring: static or dynamic. In the case of collisional quenching, an increment of temperature would result in a steady increment of the quenching rate (K_{SV}) due to a higher diffusion and collision of gas particles with the quencher. Static quenching, on the other hand, would result in a steady reduction of the quenching rate due complexed compounds dissociating.[94]

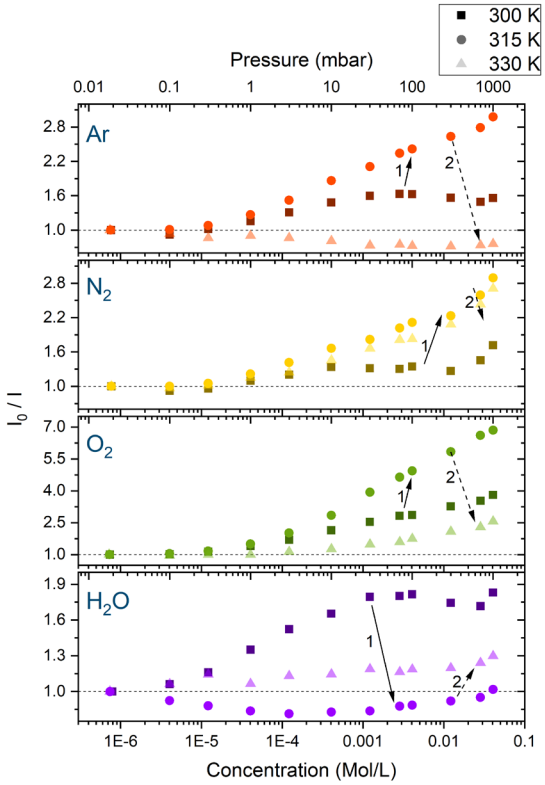

Figure 3.10. Stern-Volmer analysis of triple cation perovskite samples exposed to argon, nitrogen, oxygen, and water-enriched argon (H_2O) at temperatures of 300, 315 and 330 K.

Figure 3.10 shows the effect that temperature has on the PL quenching of the samples. Here, measurements were performed at temperatures of 315 K and 330K. Cooler temperatures were avoided to reduce other type of undesirable side-effects, like extended waiting times until thermal equilibrium was reached between the helium coolant and the heating plate of the cryostat, or the unlikely condensation of water inside of the chamber from the water-enriched argon gas.

The results showed an increment on the quenching rate at 315 K for argon, nitrogen, and oxygen. At 330 K, the behavior reversed into a decrease of the rate, showing the opposite trend for water-enriched argon. However, these results were not reproducible. Experiments on different samples showed opposite behaviors under the same conditions. We attribute the unreliability of the measurement to a phase change of the perovskite. Metal halide perovskites have a known change of lattice phase within the range of 290-350K.[159,160] For this reason, a different technique involving the PL lifetime was used to determine the type of quenching that undergoes on the MHPs under these gases.

3.4.3 SV Analysis: PL Lifetime

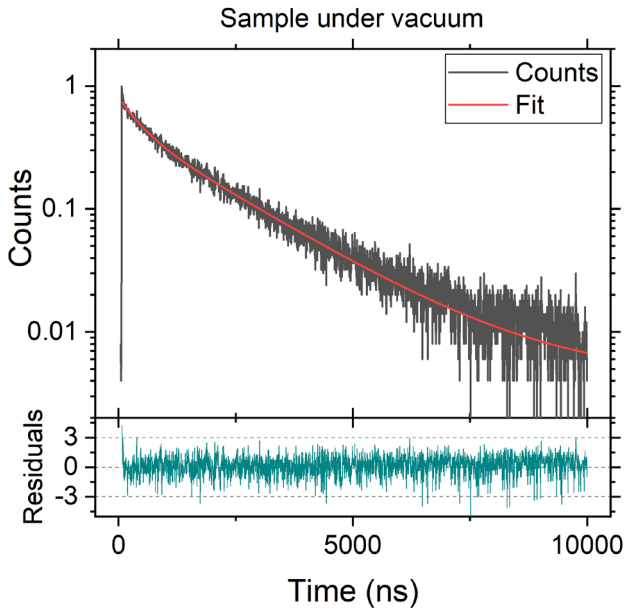

Figure 3.11. Example of lifetime data fitting. Here, a double exponential model, in red, was used to determine the lifetime of the photogenerated charges.[139]

The change of PL lifetime at different concentrations of quencher can be used to determine the type of PL quenching mechanism that is occurring. For instance, static quenching would show that the ratio of the lifetime of an unquenched sample to that of a quenched one would remain constant. This happens because unquenched emitters will continue to emit unperturbed. AT the same time, quenched emitters would remain permanently off. In the case of dynamic quenching, the ratio of the pristine and quenched lifetimes would increase with the quencher concentration. This is because the quenching rate is dependent on the collision rate of quenchers to emitters, which increases with the pressure.

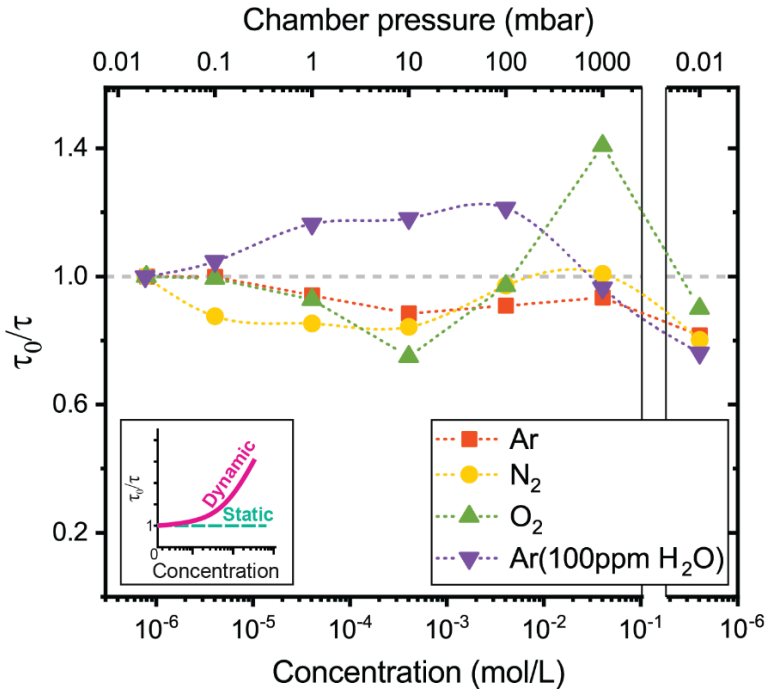

Figure 3.12. Stern-Volmer plot with respect to PL lifetime of CsMAFA in the presence of quencher molecules at pressure values of 0.02, 0.2, 1, 10, 100 and 1000 mbar.[139]

In this experiment, the PL lifetime was measured on triple cation layers that were exposed to pressures of 0.03, 0.1, 1, 10, 100, and 1000 mbar for each one of the test gases. Each PL lifetime curve was fitted with a double exponential model, as shown as a red line in Figure 3.11. The lifetime was then calculated as an intensity-weighted lifetime using eq. 2.14 from Section 2.3. Using the double decay model, the average lifetime is given by

$$\bar{\tau} = \frac{\alpha_1 t_1^2 + \alpha_2 t_2^2}{\alpha_1 t_1 + \alpha_2 t_2} \,. \qquad 3.2$$

The resulting lifetime values $\bar{\tau}$ were then plotted together, as shown in Figure 3.12. Here, the lifetime ratios remained consistently close to 1 across all concentrations for all gases. This is a strong signal that quenching occurs mostly in a static form. However, since the lifetime ratio becomes lower than 1 for argon, nitrogen, and oxygen, at different pressure ranges, there is also a sign that passivation effects are occurring. Furthermore, the small increment of PL lifetime shown by water-enriched argon suggests that the quenching mechanism was slightly more dynamic in nature than the other gases. Nevertheless, these fluctuations took place for all gases, showing that all three processes occurred simultaneously: passivation, alongside static and dynamic quenching.

3.5 PL Quenching Mechanisms

PL quenching phenomena have been widely studied on perovskites for a wide variety of gases. However, for most of them, the quenching mechanisms have not been discussed. Tian et al. introduced the issue of static and dynamic quenching in perovskites. However, the issue had not been systematically analyzed.[143]

It is known that grain boundaries play a significant role in the quenching effects of atmospheric molecules. In particular, using electron backscatter diffraction (EBSD) it has been shown that amorphous regions at the grain boundaries are sites of enhanced recombination.[161] Our interpretation of the Two-site model for the Stern-Volmer analysis, see Section 2.3.4, considers these amorphous regions as well as crystalline boundaries. Moreover, defects at the grain boundaries have also been shown to affect the efficiency of solar cells and light-emitting diodes.[141,162] Taking this into consideration, the community has developed successful measures to effectively passivate the negative effects that grain boundaries have on devices by using a diverse number of cations[46,163–166] and molecules[167–171] to the perovskite crystals.

As it will be discussed for oxygen and water in particular, the interaction of these molecules with the perovskite crystal leads to a band bending of the material, as high as a few hundreds of meV.[172] However, it has been shown that flat band conditions can be recovered by

illuminating the samples with UV or visible light.[172] Hence, all of our measurements are considered to be performed in flat band conditions.

By comparing our results with studies conducted on other materials, we have narrowed down the nature of these quenching phenomena to three different mechanisms that will be discussed in the following sections.

3.5.1 Oxygen Quenching Mechanism

In the experiments discussed in Section 3.3, oxygen has exhibited a consistent and strong quenching effect. Simultaneously, there is evidence of a photo-induced diffusion effect, as discussed by Tian et al.,[143] where oxygen bound to the perovskite lattice results in a permanent reduction of emission, of at least 20%. However, this effect is limited since successive cycles of oxygen addition did not significantly alter the PL emission trend of consecutive cycles, as shown in Figure 3.3.

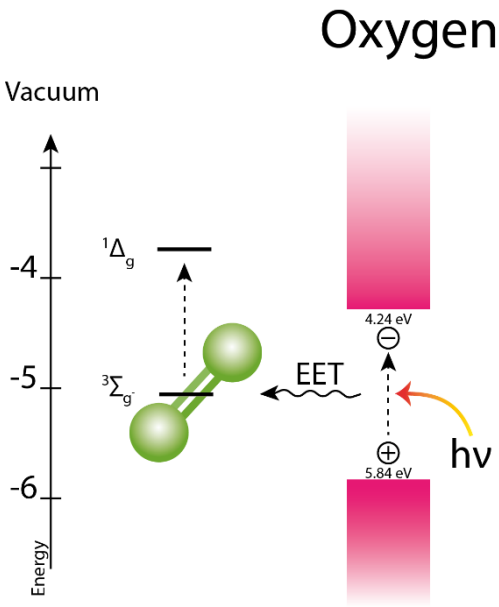

Figure 3.13. Proposed mechanism for PL quenching of molecular oxygen on CsMAFA layers. CsMAFA valence band measured by Zu et al.[139,172]

A large volume of the published literature focuses on the detrimental effect that oxygen has on MHP materials. For instance, it has been demonstrated that molecules of oxygen bind to iodide vacancies in the bulk of the perovskite, resulting in passivation of sub-bandgap states.[173] At the same time, this process leads to the formation of superoxide, an oxygen molecule that is charged by resonance energy transfer (RET) from the perovskite. Superoxide is a highly reactive

compound that can interact with the surrounding perovskite ions in the crystal, destroying the lattice and accelerating the degradation process.[150,174–176] The degradation process can be further enhanced by increasing the incident photon dose.[177] This issue directly impacts the stability of the material under light concentrators to enhance the power conversion efficiency of the devices, or during characterization using high intensity lasers.[178–180] For this reason, we have attended to accurately measuring the photon density of our characterization devices.

The PL quenching mechanism of oxygen has been widely studied in a large variety of compounds and molecules.[151,181] It has been shown that energy is transferred to oxygen at the highest occupied molecular orbital of molecular oxygen, where two degenerate antibonding pi-orbitals form. This creates a ground state in an electronic triplet state.[91] Excitation in the emitter can then be transferred to the oxygen ground triplet state via a Dexter resonance energy transfer, a type of electronic energy transfer (EET). On the other hand, the tested perovskites do not require the formation of triplet states because generated electron-hole pairs are unbound at room temperature.[182] Spin statistics demonstrate that freely recombining dissociated electron-hole pairs will produce three correlated triplet states for every singlet one. The resulting energy transfer forms dark states that slowly release photons.[93,183] Such a process is depicted in Figure 3.13, where the perovskite crystallite is de-excited to the ground state the moment an oxygen molecule touches it. During this process, the charge transfers to a singlet state which is also known in the literature as superoxide.[176] The resulting charged oxygen molecule is highly reactive, making it easy to bind to other molecules, and in the case of perovskite, to its iodide vacancies.[150] Additionally, the binding process of oxygen molecules to the perovskite crystals has been shown to reduce the n-type character of the perovskite.[184] In the short term, the binding of oxygen into the perovskite lattice induces a passivation effect. However, it leads to a faster degradation in the long term.

3.5.2 Water Quenching Mechanism

In our low-pressure experiments, the samples under water-enriched argon conditions showed a strong but reversible quenching effect. Also, when the perovskite was exposed to a flow of water-enriched argon, the PL emission reduced immediately but recovered within seconds. This recovery is supported by the Stern-Volmer analysis of the PL lifetime result, where the quenching mechanism of water appears to be more of a dynamic nature. However, the fact that

PL intensity is recovered and maintained so promptly, even when the stream of gas is still going through the sample implies that there is an additional process occurring.

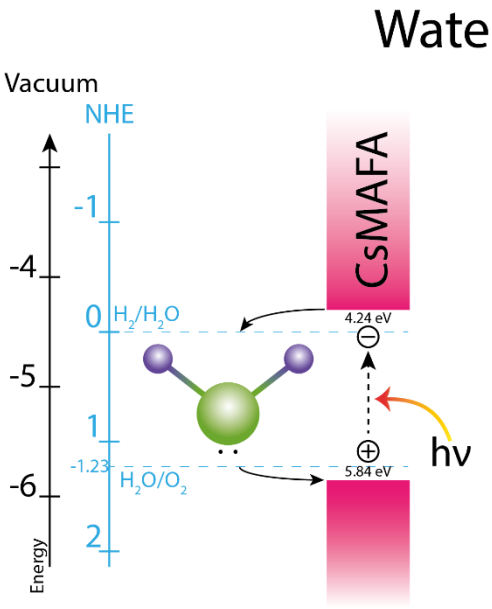

Figure 3.14. Proposed mechanism for PL quenching of water on CsMAFA layers. NHE stands for Normal Hydrogen Electrode.[185] CsMAFA valence band measured by Zu et al.[139,172]

The effect of water on perovskites has been studied in the literature extensively. Some publications have shown that exposure of perovskite layers to small concentrations of water during the preparation leads to an improvement of power conversion efficiency.[186–188] Additionally, small quantities of water have been shown to become physisorbed to the surface of the perovskite crystals, increasing the n-type nature and lowering the work function, likely due to the reduction of lead by water to Pb^0.[184] On the other hand, the large majority of publications have shown that perovskite crystals are rapidly degraded under exposure to a water atmosphere.[189–192]

The process occurring between an excited perovskite crystal and a molecule of water can be explained with standard reduction potentials of water-splitting. As shown in Figure 3.14, the H_2/H_20 and H_2O/O_2 potentials align with the valence and conduction bands of the CsMAFA perovskite.[185] Notwithstanding, water splitting is improbable because four electrons are needed to complete the redox cycle, which would result in separated oxygen and hydrogen molecules.[193] A half reaction is more likely to occur, where $2\ H_2O + 2e^- \rightarrow H_2 + 2\ OH^-$, with a more favorable potential of 0.83 V.[185] Furthermore, hydroxide anions have been reported to lead to a strong PL quenching effect via a triplet state, resulting in a Brønsted-Lowry type proton

transfer with large molecules.[194–196] With this in mind, a redox mediated PL quenching process can account for the immediate recovery of PL emission when water was still flowing into the chamber.

3.5.3 Nitrogen & Argon Quenching Mechanism

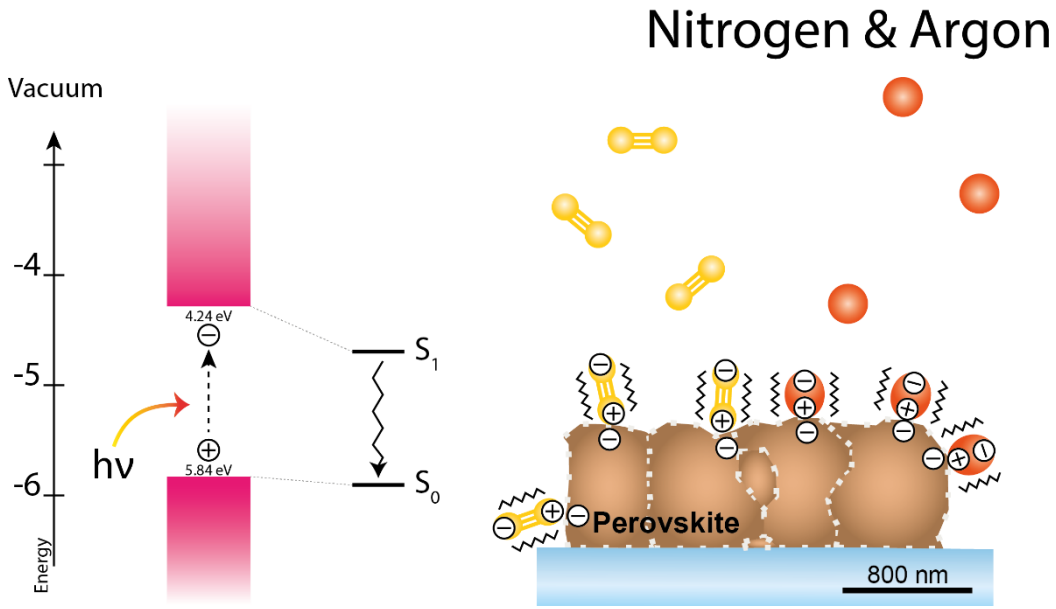

Figure 3.15. Proposed mechanism for PL quenching of nitrogen & argon on CsMAFA layers. CsMAFA valence band measured by Zu et al.[139,172]

Argon and nitrogen molecules showed a weak but consistent quenching effect in our experiments. However, there are scant reports discussing PL quenching effects of argon or nitrogen found in the literature. Argon is known to form Van der Waals (VdW) complexes with other particles under certain conditions, inducing a distortion on the electric orbitals of the emitter via VdW forces.[197–199] Electronic excitations from the emitter can be transformed into vibrational energy on the argon atoms.[200] In the case of perovskite crystals, we infer that induced surface dipoles cause the depopulation of the excited state of the emitter via electrostatic interaction, as shown in Figure 3.15. This interaction is weak, resulting in a minor reduction of PL emission.

Nitrogen molecules have been reported to quench the emission of metal oxides, as it occurs in the case of ZnO:Au.[201] However, there are no reports on the specific mechanism of this phenomenon. Nevertheless, VdW complexes could also be behind the quenching mechanism of this molecule, similar to what happens with argon atoms. In the case of nitrogen, the

combined electron cloud of the two atoms forming the nitrogen molecule can enhance the effect of the VdW forces for RET. This would translate into a stronger PL quenching effect than argon molecules, as shown in our measurements. Yet, further experiments are needed to completely understand the quenching mechanisms of argon and nitrogen.

3.6 Conclusion

In conclusion, it was shown that reversible quenching effects, as well as passivation, are present in MHP layers exposed to molecular oxygen, molecular nitrogen, argon, and water-enriched argon. By measuring the integral PL emission and PL lifetime of the samples as they were exposed to the gases, the data was later analyzed with the Stern-Volmer model to unravel the quenching mechanisms of each molecule.

The strongest bimolecular quenching effects were measured for oxygen and water, in the form of water-enriched argon. Also, small but noticeable quenching effects caused by nitrogen and argon were measured and reported for the first time. Additionally, although the quenching effect of oxygen was reversible due to the persistent recovery of PL emission when returned to vacuum conditions, there was evidence that a fraction of oxygen molecules permanently bound to the perovskite lattice and that the effect occurred mostly at the surface. Water, on the other hand, showed a more dynamic type of quenching. Additionally, a noteworthy passivation effect was measured for water since PL emission increased after consecutive cycle of water addition.

The quality of the crystal also played a role into the efficacy of the quenching molecules, where boundary defects play a unique role on the quenching effect of the molecules. In this sense, high quality crystals, that showed higher PLQY values, were more likely to show passivation effects. Also, the role of the grain boundaries for quenching is minimized as the crystal sizes increases.

Finally, using the Stern-Volmer model, the bimolecular quenching constants for each one of the tested gases were calculated, some of them for the first time in a solid-state system. These results were used to propose energy transfer mechanisms for all the molecules.

Nevertheless, further experiments are necessary to unmistakably identify the energy transfer mechanisms that occurs for nitrogen and argon. Moreover, having determined the location and nature of the quenching processes, it is imperative to implement materials and develop procedures that would diminish the negative quenching effects of these molecules and promote the passivation ones. Some of this work is currently ongoing in the perovskite community, as it is the case of growing number of publications that use diverse ions and molecules to passivate the perovskite layers. However, the Stern-Volmer analysis can be used as a tool to accelerate the development of these procedures since it allows a direct quantitative measure of their passivation effect.

4 Inkjet Printing of Metal Halide Perovskites

4.1 Introduction

Metal halide perovskites (MHPs) are well-known for their ease of preparation as a solution process. Along with that, a steep development of the power conversion efficiencies (PCE) of perovskite solar cells has sparked an interest to extend the process outside of the lab-scale into large area devices. A successful implementation of a large area deposition would allow the development of a manufacturing process that would eventually bring photoelectronic devices to consumers as low-cost products.

In a lab environment, most devices are deposited by spin coating. However, spin coating substrates with a diameter larger than 10 cm requires special considerations since larger amounts of ink are needed and the thickness of the layers can vary across the area.[202] To go beyond this limit and still maintain smooth surfaces it is necessary to use other coating techniques. In the case of perovskite devices, blade coating,[203] slot-die,[51] spray coating,[204] inkjet printing,[205] and vacuum deposition[206] have all been successfully used.

Large area solar cells are usually deposited in the form of modules, where the total printed area is broken into smaller segments of narrow width to reduce the effect of parasitic resistances. The largest demonstrated perovskite module had 25 interconnected cells with an active area of 168.75 cm² and was prepared via slot-die coating, showing a maximum PCE of 11.1%.[207] Nevertheless, techniques and materials differ from lab to lab. For this reason, solar cells with an area of 1 cm² are usually used as a standard to compare the quality of the devices. Using inkjet printing on a research scale, the maximum demonstrated efficiency of a solar cell was 12.3% with an area of 1 cm².[9] For smaller inkjet-printed devices, a maximum PCE of 20.7%

has been achieved in an area of 0.105 cm²,[208] which is also the maximum efficiency demonstrated for a non-spin coated device.[61,122,209]

The possibility of making highly efficient devices via inkjet printing makes inkjet printing attractive for preparing devices with a diameter larger than 10 cm. This technique has already been validated as a convenient method to deposit organic electronics since the 1990s and many groups around the world start to apply it for the deposition of perovskites.[210] However, unlike organic solar cells, the deposition of MHPs involves an extra post-treatment process to trigger the crystallization of the material. For instance, to accomplish a highly efficient device the drying of the wet layer must be synchronized with the crystallization process of the perovskite. For spin-coated layers, this issue is solved by applying an antisolvent to the sample at a precise moment. However, antisolvent use is discouraged in inkjet-printed layers since the buildup of solvents interferes with the crystallization process. Other techniques have been implemented to start the crystallization process of the layers, as it is the case of the two-step deposition,[211] dual-flash process,[212] vacuum annealing,[205] infrared annealing,[52] solvent engineering[213] and the use of additives and surfactants.[62,203,214]

In this thesis, the crystallization process of the inkjet-printed perovskite layers was controlled in three different ways. They are the Two-step deposition, Vacuum Annealing, and a novel self-developed technique called Flow Control. In the following sections, the strengths and weaknesses of each technique will be discussed. Additionally, the new tools and procedures that were developed for the Flow Control technique will be described in detail. A list of optimized printing parameters and a description of the best achieved devices will be provided at the end.

4.1.1 Complications when Printing

As mentioned earlier, inkjet printing of perovskites requires the careful synchronization of the drying and crystallization processes of the material. As an overview of the challenges of printing MHPs, this section will discuss the most common macroscopic and microscopic defects that must be overcome during the printing process, focusing on the microscopic ones that are unique to perovskites, and will detail steps to avoid them.

Figure 4.1 shows macroscopic defects encountered during the inkjet printing process of perovskite layers. Figure a) displays a layer that is only partially covered due to clogging of the printhead nozzles. Clogging occurs for various reasons. Most frequently, nozzles become

clogged due to gas bubbles filling up the nozzles. This is especially the case when first loading the ink reservoir. The best method to remove these bubbles is by first filling the ink reservoir with solvent. Then, the solvent is repeatedly purged until all nozzles are freed. Once the nozzles are fully working, the solvent can be replaced with the ink. At this point, it is crucial to make sure that new pockets of air are not formed during the ink refilling by, for example, letting the ink reservoir to empty, an issue that is more common than one would expect.

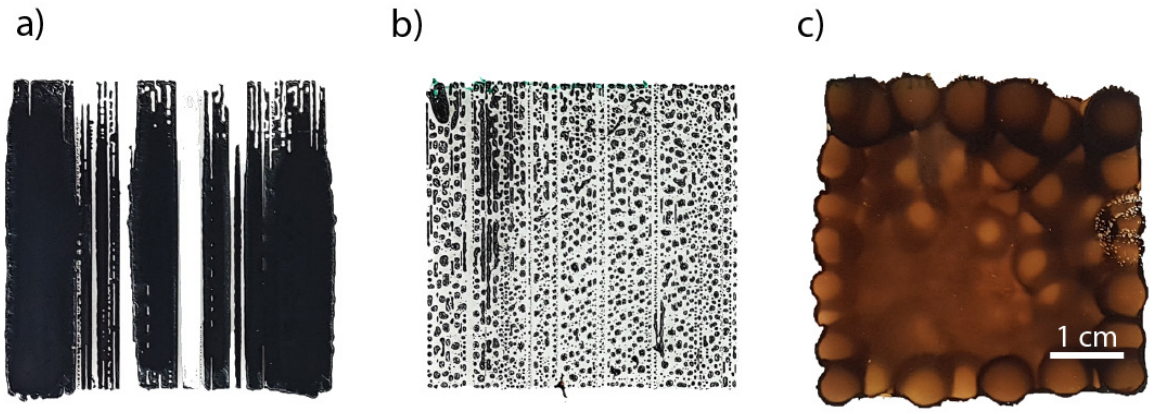

Figure 4.1. Photographic images of dried inkjet-printed samples showing macroscopic defects. Background and substrate borders were digitally removed. These undesirable layer formations correspond to a) clogged printhead nozzles, b) poor substrate wetting, and c) ultrafast-pumping rates.

Another way of nozzle clogging occurs due to ink drying inside of the nozzles. This can happen when the printhead remains idle for too long. The effect is intensified when the ink solvents have a low boiling point. The best way to avoid this problem is by continuously using the printhead, either by printing or purging. In case that nozzles still become clogged, the fastest solution is to remove the ink and clean the printhead with pure solvent using the method described above. Moreover, the nozzles could become physically clogged due to particles blocking the piezo movement. The best way to avoid this issue is by filtering any ink or solvent that will go through the printhead. Most printheads that become physically clogged by large particles are difficult to fix, although sonicating the printhead could help. On the downside, some printheads are not resistant to sonication and can break. Hence, this technique should be used with care.

In the case of our experiments, a cleaning procedure was established to ensure a fully working printhead before starting the printing process. The process was automatized using an script, see Appendix 7.9, written for AHK (AutoHotKey), which is an open source scripting language to

control the mouse and keyboard movements with code. Starting with an ink reservoir full of pure DMSO, the script drives the purging of solvent for 0.05 seconds every 15 seconds. By heating up the printhead to 70-80 °C, the unclogging process is accelerated. This method can clean the printhead within 30 to 60 minutes with all nozzles available.

Figure 4.1b shows another common artifact that is related to the substrate's wetting. In this example, triple cation perovskite was inkjet-printed on a PTAA layer, a material with poor wettability. In general, it is necessary to match the surface free energy of the substrate with the surface tension of the ink, which involves a whole analytical procedure. However, sometimes it is enough to clean the substrates with ozone plasma or oxygen plasma treatments. Yet, cleaning procedures need to be used with care since they also modify the electronic structure of the substrate and can change the physical properties of charge transport layers. Moreover, surfaces sometimes become less wettable over time, as is the case for layers that have been pre-treated to reduce their contact angle with a plasma treatment or similar techniques.

The formation of large bubbles, in the range of 3-5 mm, was also encountered in our samples, mainly on the edge of the printed pattern. This effect was mentioned in Section 4.4. The artifact only appeared when the vacuum rate was too high, of over 140 mbar/s. In this case, the air inlet was also facing directly at the substrate and the effect became amplified when the chamber was set to a higher temperature of 80 °C. It is not clear why this pattern appeared. However, the common denominator was the high pumping rate in all cases.

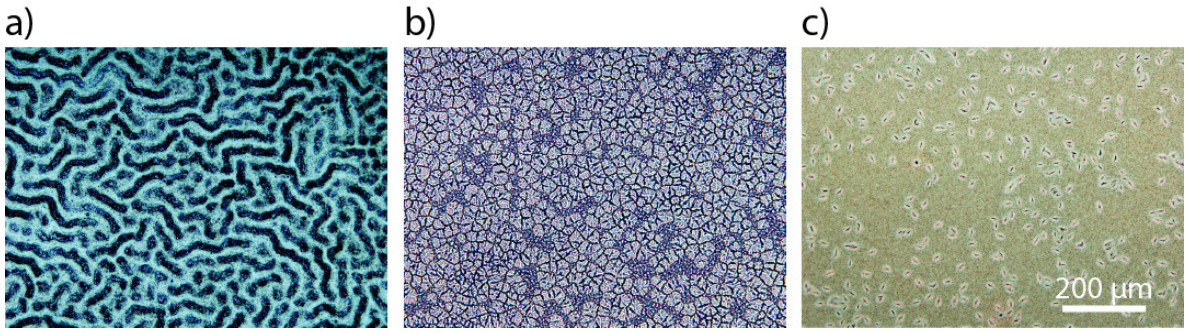

Figure 4.2. Optical microscopy images of dried inkjet-printed layers showing diverse defects, like a) wrinkled surfaces, b) medium-sized crystals and c) bulges. Layer colors are artificial.

Additionally, there are undesirable microscopic morphological problems that can occur during the printing process and which are unique to the drying process of perovskites. Figure 4.2 shows some of the most common defects we encountered. Figure 4.2a displays a wrinkled pattern that

only appeared when the printing process resulted in thick wet layers. A similar phenomenon has been linked to the concentration of cesium on spin-coated samples.[215,216] However, the effect shown here appeared exclusively on inkjet-printed layers that, when dried, had a thickness beyond 900 nm, making more prominent wrinkles as the thickness increased. They appear because, as solvent is removed during the flow process, the wet layers become more concentrated in certain areas while liquid regions continue to influence their surroundings, forming conglomerates that look like wrinkled patterns.

The pattern in Figure 4.2b shows large, delimited crystals that appeared when the sample was placed on the hotplate too early. These layers were still in a liquid phase when they were placed on the hotplate, meaning that the vacuum process was not long enough. For reference, this pattern is a smaller version of the one shown in Figure 4.8b. However, the crystals here are smaller because a larger portion of the solvent had been removed with the flow of nitrogen in the chamber.

Finally, the defect shown in Figure 4.2c only appeared when the evacuation rate was fast. Unlike the situation shown in Figure 4.1c, these samples did not show the ring bubble effect. Upon analysis with AFM, these defects appeared as little ovals that made a dip on the border and bulged outwards at the middle, appearing as dark centers in the image. It is unclear how these formations occurred, and we dismiss the possibility of them being debris since all substrates were cleaned before printing and the inks were properly filtered.

4.2 Materials and Experimental Setup

The perovskite precursors used for these experiments were the same as the ones used in Section 3.2. Materials specific to these experiments were poly(triaryl)amine (PTAA), the fullerene C_{60}, bathocuproine (BCP), imidazole, and γ-butyrolactone (GBL), all purchased from Sigma-Aldrich. [2-(9*H*-Carbazol-9-yl)ethyl]phosphonic acid (2PACz) was purchased from TCI Chemicals. Poly(3,4-ethylenedioxythiophene) polystyrene sulfonate (PEDOT:PSS) AI 4083 was purchased from Heraeus. Copper, used as contacts, was purchased from Alfa-Aesar. All chemicals were used as received, without further purification.

All glass and substrates with conductive indium tin oxide (ITO) layers were cleaned in a similar way to literature procedures.[217] All substrates were brushed with mucasol (soap) diluted in deionized water to 2 vol.%, then sonicated for 10 minutes. Later, the samples were rinsed with deionized water and consecutively sonicated with deionized water, acetone, and isopropanol for 10 minutes each. Finally, the samples were cleaned with UV ozone for 5 minutes. Notice that the cleaning procedure used on these substrates was shorter than the one described in Section 3.2.

Two Step Technique

Two inks were needed for this technique. The first one was PbI_2 dissolved on DMF at a concentration of 0.64 M. The second one was MAI dissolved in IPA at 0.08 M.

The layers were printed in air, using a Fujifilm Dimatix and 10 pL cartridges with 16 nozzles. The optimized printing procedure PbI_2 had a resolution of 726 DPI and the printhead was heated to 30 °C. MAI was printed at 1270 DPI at 55 °C.

These layers were characterized with a Veeko Dektak 150 or a Brucker Dektak XT profilometer and an optical microscope.

Vacuum Annealing Technique

The perovskite solutions, also referred to as *inks* in this chapter, were prepared similarly to the process described in Section 3.2. However, the perovskite solution used for spin coating was diluted by half, to 0.62 M, and contained a 4 vol.% of GBL. This ink had a surface tension of 37.2 mN/m and showed shear thinning behavior, reaching a shear viscosity of 1.8 mPa·s at room temperature, as shown in Figure 4.3.

This technique used a PixDro LP50 inside of a glovebox and Spectra SE printheads with 128 nozzles and capacity for 30 pL droplets. The LP50 settings for the substrate holder and printhead temperatures were 20 and 25 °C, respectively. The voltage was set to 80 V with a Rise Edge, Peak Time, and Fall Edge of 3,11 and 3 ms, respectively. The quality factor was set to 4 and resolution to 350 DPI.

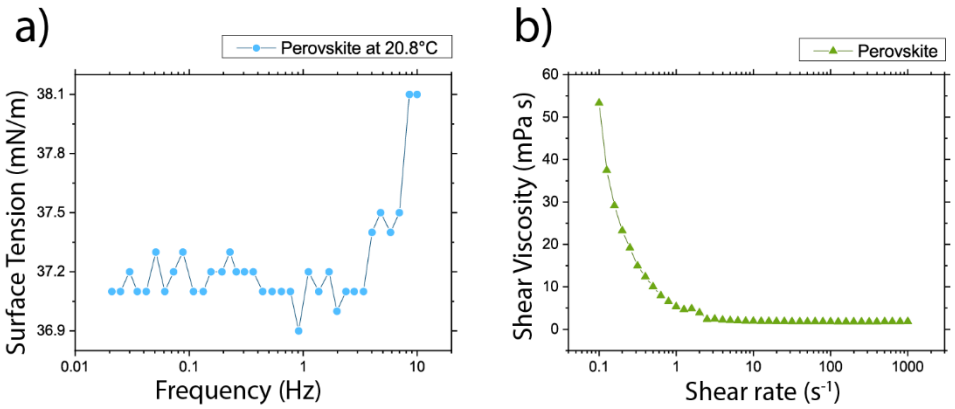

Figure 4.3. Ink properties at room temperature showing a) the surface tension and b) the shear viscosity of the perovskite ink with a concentration of 0.62 M.

Flow Control Technique

The perovskite inks were prepared similarly to the process described in Section 3.2. However, the printed mix was diluted to 0.62, 0.52, and 0.42 M and contained a 25 vol.% of GBL.

The printing process used an LP50 printer by Pixdro and Spectra SL printheads with 128 nozzles and 80 pL droplets. The process was done inside the glovebox in a nitrogen atmosphere. The LP50 settings for the substrate holder and printhead temperatures were 20 and 30 °C, respectively. The voltage was set to 100 V with a Rise Edge, Peak Time, and Fall Edge of 3,12 and 3 ms, respectively. The quality factor was set to 2 and resolution to 300 DPI.

Devices

All devices were fabricated with a p-i-n planar architecture. Different HTLs were used, namely PEDOT:PSS, PTAA, 2PACz, and NiOx.

PEDOT:PSS layers were prepared by diluting the as-purchased solution 1:1 into a mix of isopropanol, ethanol, and water in a ratio of 2:2:1. Imidazole was added to the solution right before spin-coating to 0.55 wt%. The solution was spin-coated in air at 1000 rpm and 1000 rpm/s for 45 seconds and annealed for 1 hour at 100 °C, resulting in layers with thickness of ca. 20 nm.

PTAA layers were prepared by spin coating on ITO substrates as described in ref. [218]. PTAA was diluted to a concentration of 8.1 M in chlorobenzene. The solution was spin-coated at 6000

rpm and 2000 rpm/s for 30 s and later annealed for 10 min at 100 °C, resulting in a layer of ca. 8 nm.

The SAM 2PACz layers were prepared by spin coating on ITO substrates as described in ref. [219]. Dissolved at a concentration of 3mM in anhydrous ethanol, the solution was spin coated at 3000 rpm for 30 seconds and annealed for 10 min at 100 °C.

NiOx layers were deposited to a thickness of 20 nm by magnetron sputtering at 150W under argon plasma. The process was done by partners at CSEM using a ClusterLine 200 II from Evatec.

After the perovskite was deposited, consecutive layers of C_{60}, BCP and Cu were deposited by evaporation with thicknesses of 23, 8, and 100 nm, respectively.

Other characterization, like scanning electron microscopy, using a S4100 microscope, by Hitachi and a cold emission gun were made by Carola Klimm, of Helmholtz-Zentrum Berlin. XRD measurements were done by Andreas Bohn, of Fraunhofer Institute of Advanced Polymer Research, using a Bruker-AXS, two-circle-diffractometer D500 (46 KV, 30 mA) with Cu K-alpha radiation. Contact angle measurements were made by Paul Hänsch, of Humboldt University of Berlin.

4.3 Two-step Deposition Technique

Also known as Sequential Step Deposition, this technique was implemented early on to circumvent the use of antisolvents for spin-coated devices.[220] Widely popular for the preparation of methylammonium lead iodide (MAPI) layers, the key point of this technique is to form a perovskite layer by combining two separate precursor layers. First, a highly saturated lead iodide (PbI_2) solution is place on the substrate and dried. Then, the sample is exposed to a low-concentration solution of methylammonium iodide (MAI).[221]

Multiple variations of this technique have been published throughout the years. Some use solutions with different combinations of salts to yield higher quality layers.[222] Others rely on individual pure dissolutions.[223] For instance, one of the first large area devices showing high

efficiencies was prepared using this method. Here, the first layer of lead iodide was applied by blade coating and later dipped into a bath of MAI.[224] This technique has also been successfully applied to inkjet-printed layers, yielding a high efficiency of 18.6% in an area of 0.04 cm^2.[211] On the other hand, this technique only allows the formation of simpler types of perovskite that can be formed out of two different solutions, MAPI being the most popular.

For these experiments, a Dimatix Fujifilm inkjet printer was used to deposit a perovskite layer in two steps. This printer comes with a simplified set of parameters that allows the test of various printing conditions and ink combinations in a speedy way. The printheads had a droplet volume of 10 pL and were modified to be reusable.

4.3.1 Effect of Resolution and Temperature

To inkjet-print a homogenous layer, it is necessary first to make sure that the density of the droplets is high enough for them to merge. Beyond this point, a range of densities will still form smooth layers while the thickness of the layer will increase. By keeping on increasing the density, the deposited wet layer will be so thick that the drying process will be unbalanced and will produce rough layers.

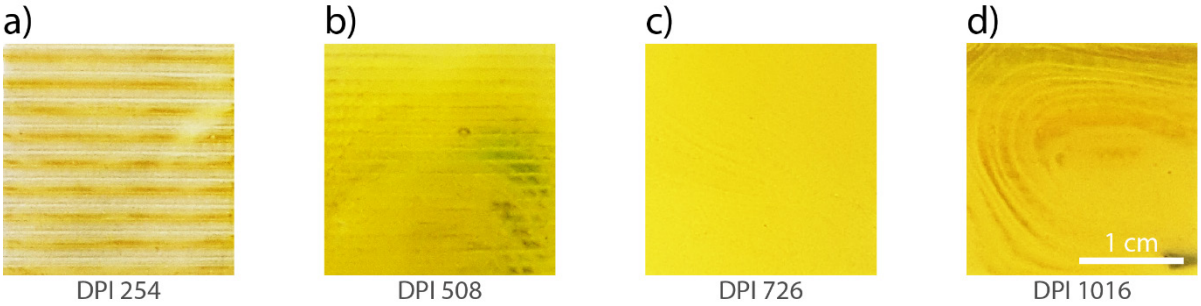

Figure 4.4. Optical photographs of lead iodide printed on a glass substrate at different resolutions of a)254, b)508, c)726 & d)1016 DPI. Optimum film properties were achieved at 726 DPI, where a minimum number of defects are visible.

The effect just mentioned is shown in Figure 4.4, where increasing resolutions of PbI_2 were printed, namely 254, 508, 726 and 1016 dots-per-inch (DPI). The solution of PbI_2 had concentration of 0.64 M on DMF. The chosen resolutions are so specific because this printer only allows precalculated resolution steps that depend on the printhead angle. Figure 4.4 shows that lower DPIs of 254 and 508 resulted in an incomplete coverage of the substrate. Increasing

the DPI to 726 led to a homogeneous-looking layer, while a much higher resolution of 1016 resulted in the formation of unwanted visible patterns.

The temperature effect of the printhead and substrate holder was also tested to explore the spreading of the ink across the substrate. From a range of 30°C to 60°C, the cooler temperatures resulted in smoother layers, as shown in Figure 4.5. At 60°C, the layers showed a repeating pattern, consistent with the nozzle separation, where regions had long crystalline structures, a sign that the layer was being dried as soon it was being deposited, this is shown in Figure 4.5b.

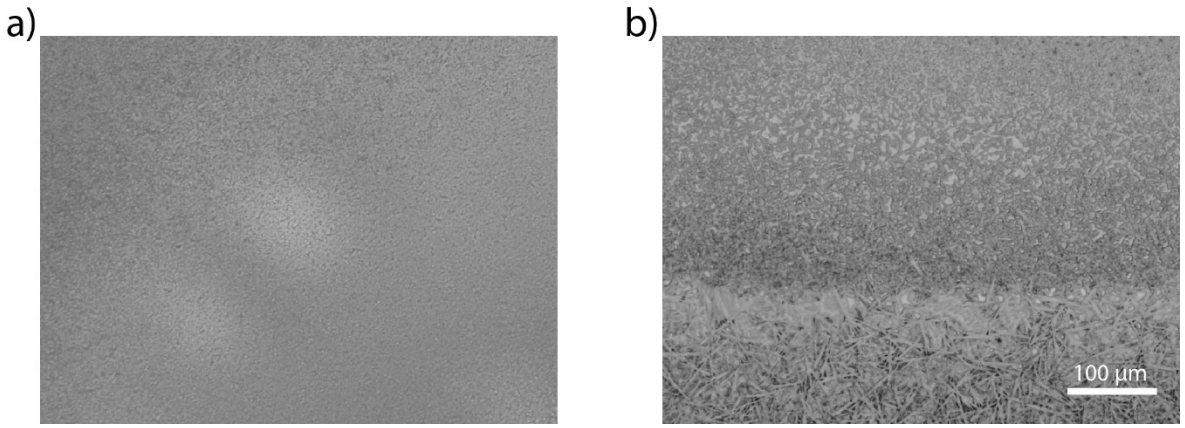

Figure 4.5. Effect of temperature on PbI_2 layers. Microscopic images of a) a layer printed on a substrate at 30 °C and b) at 60°C.

Once the PbI_2 layer was deposited, the sample was then dried on a hotplate at 100 °C for one hour to ensure the complete removal of solvents. Next, a methylammonium iodide (MAI) solution at a concentration of 0.08 M in isopropanol (IPA) was deposited via inkjet printing on top of a dried PbI_2 layer. The solvent was changed from DMF to IPA because the latter solvent is orthogonal to PbI_2, meaning that it is not able to dissolve it. Otherwise, if the PbI_2 layer is dissolved, the crystallization effect is dramatically affected, resulting in a coarse layer. To ensure the reproducibility of this test, MAI was inkjet-printed on smooth PbI_2 layers deposited by spin coated.

The deposition of MAI layers was also optimized by fine-tuning the printing resolution. In this case, the printhead was not heated because the low boiling point of IPA resulted in the rapid clogging of the nozzles. The resulting printed layers are shown in Figure 4.6. Here, the tracks of the nozzles are visible for all resolutions, namely 1016, 1270, 1693 & 2540, finding the smoothest layer at 1270 DPI. However, the microscopic images make it clear that none of these layers is truly smooth. The lined patterns appeared because IPA evaporates soon after it is

placed on the substrate. And although this problem can be minimized by adjusting the density of the droplets, this fix is not enough by itself to achieve completely smooth layers. Ethylene glycol was also tested as a medium to deposit MAI. However, this deposition did not react with the dried PbI_2 layer to form a perovskite.

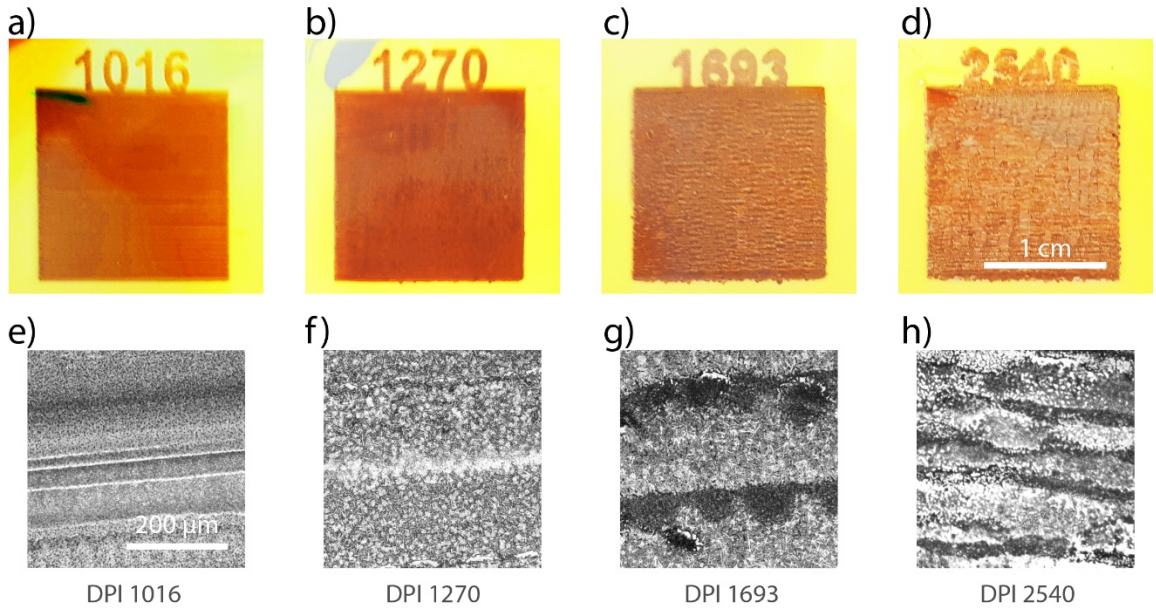

Figure 4.6. Pictures and microscopic images of MAI layers printed on top of a dry lead iodide layer with DPI resolutions of a) & e) 1016, b) & f) 1270, c) & g1693, and d) & h)2540. The images have been modified to enhance the visibility of the defects. Best film properties were achieved at a DPI of 1270, where horizontal lines were kept to a minimum.

4.3.2 Combination of Printed Layers

Finally, we combined the optimized processes of both printing steps. The outcomes are visualized in Figure 4.7. The macroscopic result of the two printed layers is shown in Figure 4.7a, where the chemical interaction of both inks is visible as a dark-brown area. Figure 4.7b shows a microscope image of the combined layer, where nozzle trails are clearly noticeable. Here, the darker lines are consistent with the nozzle separation of the printhead at this resolution, showing that these are the tracks of the nozzle movement where MAI was deposited.

Figure 4.7c shows the height profile of the layer. Here, the roughness is such that steps of almost 1 mm were formed. Such intense roughness makes these layers unusable for device preparation. Coarse layers like this would result in segmented top layers, which are usually in the tens of nm range, creating shunts across the device.

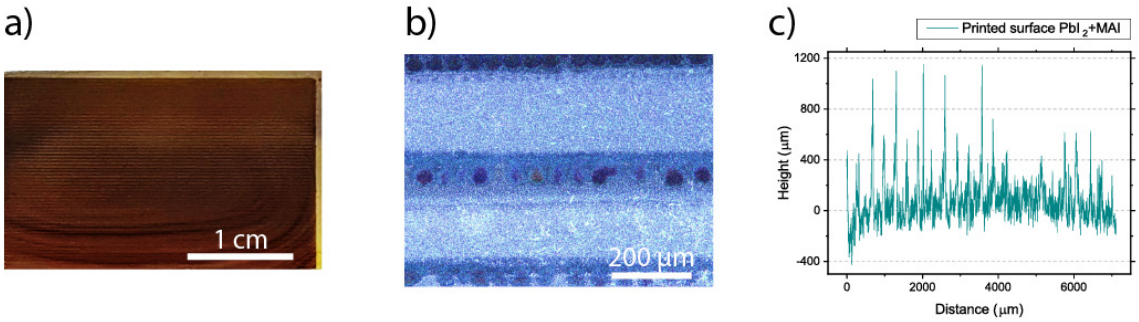

Figure 4.7. Result of combining the optimized printing procedures of lead iodide and MAI. Showing a) the macroscopic quality of the joint layers, b) the microscopic quality of the layers and c) the profilometer measurement displaying the roughness of the printed layer with a depth as high as 1 mm.

These experiments showed the viability of the two-step deposition technique. However, the combination of both printing procedures resulted in rough and unusable layers. Furthermore, a single deposition of ink was preferable because this would simplify and speed up the deposition and post-treatment processes of the layers. For these reasons, another new promising technique involving a single printing step and the use of vacuum was pursued: The Vacuum Annealing technique.

4.4 Vacuum Annealing Technique

Annealing is a standard procedure used to enhance the crystallinity of certain materials, usually by applying high temperatures.[225] For this technique, we will also use the concept of annealing as the reduction of the atmospheric pressure around the sample. Throughout this section, we will refer to each annealing technique as heat annealing or vacuum annealing to differentiate these two processes.

4.4.1 Initial Tests

Annealing by a change of pressure was reported in the literature early on with spin-coated samples of MAPI, reaching a performance efficiency higher than 20%.[226] However, the technique did not gain traction until a few years later, when a different group demonstrated a dual-flash process on inkjet-printed layers.[212] This approach was called “flash” because it involved the abrupt use of an evacuation step. Here, the sample was exposed to a pressure of 0.3 mbar in less than 10 seconds, followed by a quick annealing step at 300 °C for 10 additional

seconds. Our first reproduction attempt using films printed with the Dimatix Fujifilm showed promising results with a triple cation ink – a mix containing cations of cesium, methylammonium, formamidinium, as well as lead, iodine and bromide as anions.[23]

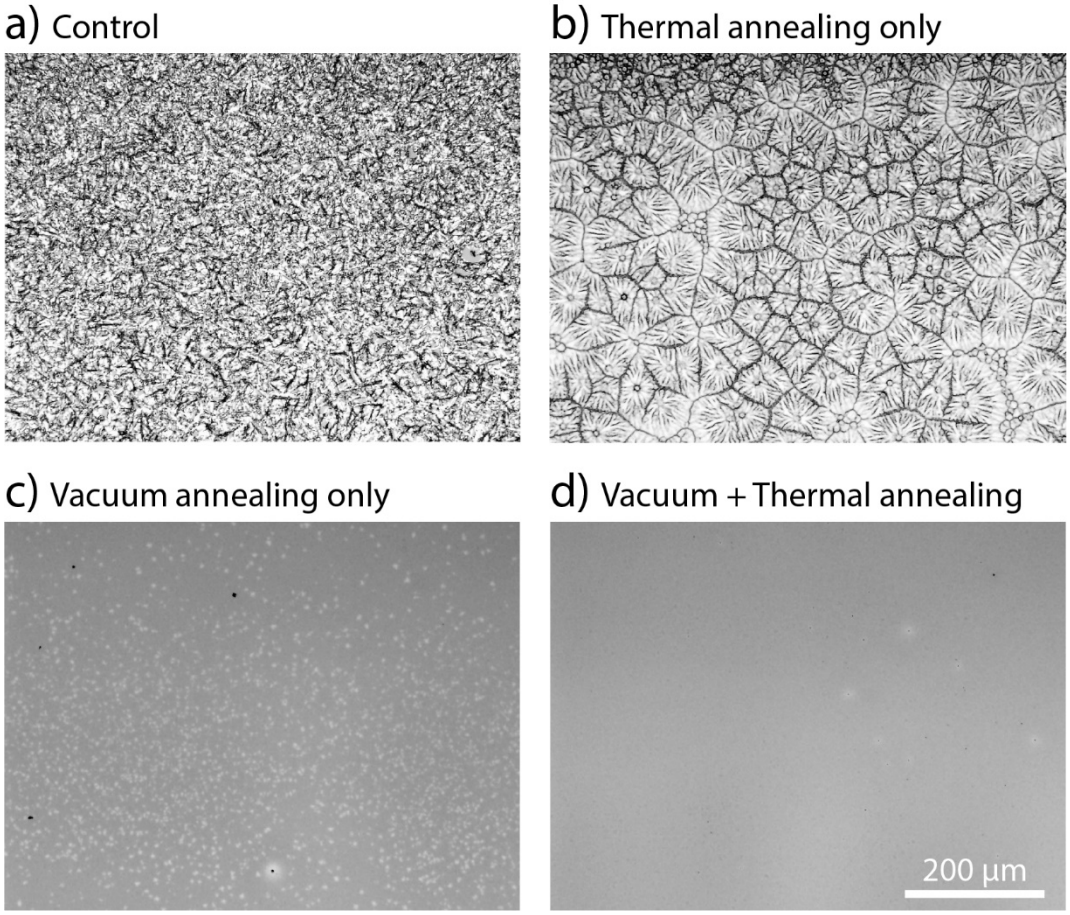

Figure 4.8. Optical microscope images showing the layer qualities achieved by different combinations of the annealing processes. Figure a) is the control sample, where the wet layer was left to dry in air by itself, resulting in rough layers. Figure b) shows the effect of only heat annealing the layers, resulting in large crystals. Figure c) shows the effect of only using vacuum annealing, resulting in an improvement on the layers homogeneity and figure d) shows the effect of applying both: vacuum and heat annealing to the samples. Here, a reduced number of defects is achieved, as compared to the other three methods.

Triple cation layers crystallized using this technique displayed greater homogeneity, as compared to the two-step deposition technique. Correspondingly, to better understand the effect of the annealing steps, Figure 4.8 shows optical microscope images of the resulting layers. The first image shows a control layer which was left to dry in air for a few hours, showing needle-like structures with a high roughness. Although these layers were much less rough than the ones obtained from the two-step technique, they were still rough enough that subsequent layers would be porous, creating recombination sites and reducing the charge transfer across the

layers. Additionally, these layers were not fully converted to a perovskite crystal in some regions. Figure 4.8b shows similarly rough surface that occurs when the printed layers are annealed only by using temperature, forming large crystals. These crystals are irregular and form large gaps in between them, making them also impractical for device use.

On the other hand, when only vacuum annealing is applied, see Figure 4.8c, the large crystals disappear, leaving a homogeneous background with small white dots on the surface. These dots are likely leftover solvent droplets, which are undesirable since they can later dissolve the crystals around them. However, by combining both annealing steps: vacuum and temperature, the layer quality increased, the resulting layers show barely noticeable defects that led to highly homogeneous layers, as shown in Figure 4.8d.

Having found a successful technique to crystallize inkjet-printed layers, the procedure was moved into a pilot plant for further optimization. The transition was necessary since one of the end goals was to demonstrate the inkjet printing process of perovskite solar cells in areas as large as 15x15 cm^2. However, the dual-flash technique involved a couple of obstacles. First, the initial fast evacuation of the chamber resulted in a particular ring effect on the border of many samples. This effect was discussed in Section 4.1.1. Also, a hot plate at 300 °C inside of the glovebox could evolve into problems with the laminar flow or damage components inside of the box.

4.4.2 Pilot Plant Process

The move into the pilot plant also included an upgrade of the printing process to a more customizable printer, the PixDro LP50. The printer used Spectra SE printheads, with a droplet volume of 30 pL, and an automated robot arm was used to transport substrates from the printer into the annealing chambers; one for vacuum- and another for heat annealing.

During the migration to the pilot plant, the procedure had to be adjusted to the new setup. This included the optimization of the printing- and crystallization processes. For instance, the previous setup used a handheld vacuum chamber, with a volume of 0.78 L, while the new pilot plant chamber had a volume of 23 L. The upgrade involved the increment of the evacuation time by a factor of ca. 24 to reach the required low-pressure of 0.2 mbar. The increment of time

from the new setup resulted in microscopic, large crystals and visible layer gaps across the sample, similar to what is shown in Figure 4.8b. Hence, the pilot plant setup was also upgraded by modifying the original pilot plant pump system with two fast oil pumps located next to the chamber. As shown in Figure 4.9, this dramatically reduce the pumping time from 240 to 40 seconds to reach a 0.2 mbar pressure. Compared to the flash procedure, the new upgraded setup still resulted in a pumping time that was 4 times longer, however, the process still yielded smooth crystallized layers. The importance of the pumping time will be discussed later.

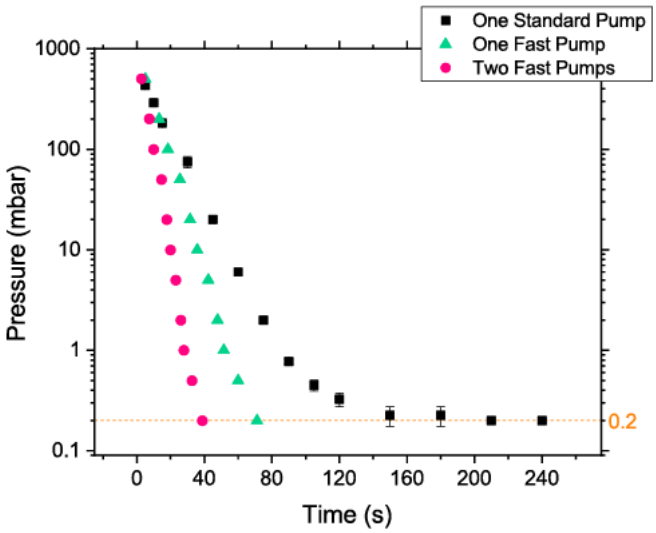

Figure 4.9. Evacuation rates of different vacuum pumps used with the vacuum annealing chamber. Updating the system to two fast oil pumps resulted in a shortening of the evacuation process from 200 to 40 seconds to reach 0.2 mbar. This timing is crucial to achieve a high-quality crystallinity of the samples.

As highlighted earlier in Section 4.3, the right combination of solvents is necessary to allow the proper wetting and coverage of the substrates with the ink. Ideally, an ink should not spread much farther than the position where it was placed. This means that the contact angle should be lower than 90°. Yet, super-wetting conditions, with a contact angle <30°, could also be problematic since layers tend to spread beyond the intended area and are also thinner than expected.[126,131]

The initial experiments used a solution developed for spin-coating. However, poor wettability of the original solvent mix, consisting of DMF:DMSO in a ratio of 4:1, formed a striped pattern when inkjet-printed, as shown in Figure 4.10a. The pattern appears because jetted droplets merged but dried before spreading over the substrate. To remove this pattern, the solution mix was modified by adding a high boiling point solvent. This type of solvents delays the

crystallization process and allow for proper spreading of the droplets. By looking to literature, NMP and GBL were found to be good candidates.[42,227] Ultimately, GBL was chosen due to its higher boiling point of 204 °C as well as compatibility with our mixture. Furthermore, GBL has a lower toxicity level as compared to NMP, and even when the original mix is based on DMF:DMSO, keeping toxicity level as low as possible was prioritized.[228]

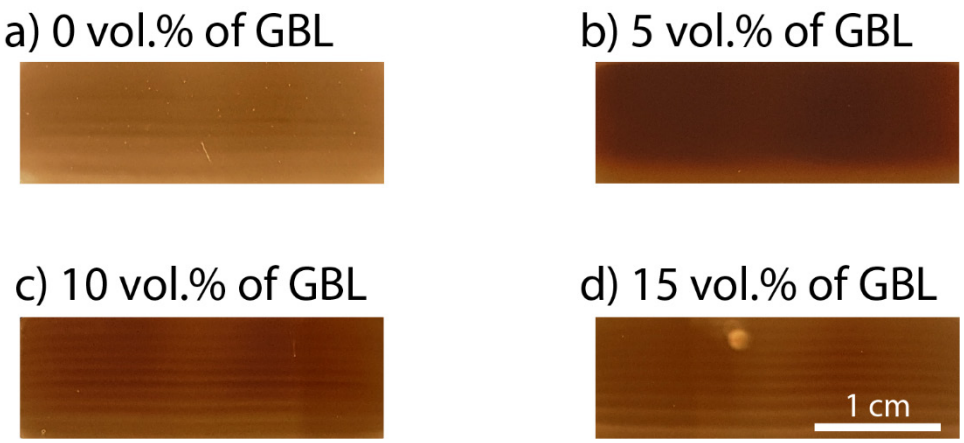

Figure 4.10. Effect of GBL content on the printing ink. The ink had a) 0 vol.%, b) 5 vol.%, c) 10 vol.% and d) 15 vol.% of GBL. A concentration of 5 vol.% GBL gave the best results.

Figure 4.10 shows the effect of adding GBL to the perovskite ink. As mentioned before, 0 vol.% of GBL resulted in a striped pattern. Adding 5 vol.% of GBL to the ink led to the smoothest layers. Further increasing the concentration to 10 and 15 vol.% resulted in a darker but striped pattern. In fact, more recent publications have also adopted GBL as the preferred additive solvent for inkjet printing applications, using as much as 50 vol.% on their final ink formulation.[9,229] The reason as to why 5 vol.% worked better in our setup, as opposed to 50 vol.% , will be further discussed in Section 4.5. Apart from this, the high boiling point solvents discussed here would have not worked with the two-step deposition technique, addressed in Section 4.3. This is because all the perovskite-forming salts are soluble in GBL and NMP, and the other technique required the solvents to be orthogonal with the lead salt.[228]

4.4.3 Analytical Method

Having accomplished a homogeneous layer, an optimization process followed. However, optimizing the process by making solar cells results in a large temporal and financial cost. For reference, a batch of solar cells takes about 2-3 days to prepare. Additionally, the cost of an 8 samples batch can range anywhere between 80 to 200 euros. The type of hole transport layers

used, like PTAA and Spiro-MeOTAD as well as the material used for the contacts, like gold, and the ITO substrates can inflate the price. For the optimization process, we focused instead on a morphological approach where the goal was to reduce the number and size of the microscopic defects of the layer.

The types of microscopic defects that we tried to reduce were pinholes. Pinholes are tiny gaps across the perovskite layer that form due to an uneven arrangement of nucleation sites and irregular crystallite sizes. They are a problem because electron and hole transport layers can contact through these gaps. If the gaps are large enough, they can create short circuits destroying the functionality of the solar cells. Smaller gaps would reduce the fill factor and overall performance of the solar cells. Pinholes are also a problem in spin-coated samples and many techniques have been developed to remove them.[230–233]

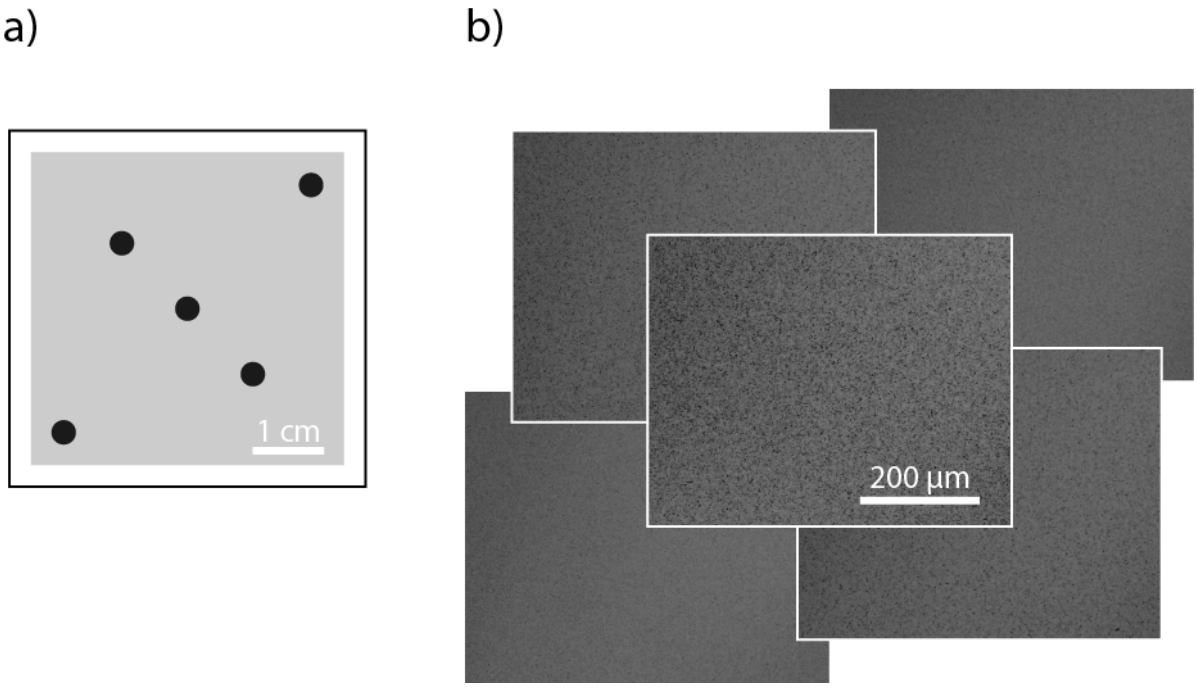

Figure 4.11. Layer morphology optimization. Figure a) shows a diagram with the positions on the substrate where pictures were taken, having two images near the corners, one at the middle and two more a distance in between. Image b) shows an example of the images taken at these positions, notice the increment of dark spots towards the middle of the sample.

A procedure was developed to study the morphology of the samples and to speed up the optimization process. Here, images were taken across the surface of the samples on five distinct places using a standard optical microscope, as depicted in Figure 4.11. Then, imageJ, an open-source software, was used to count and measure the defect areas detected by the software.[234]

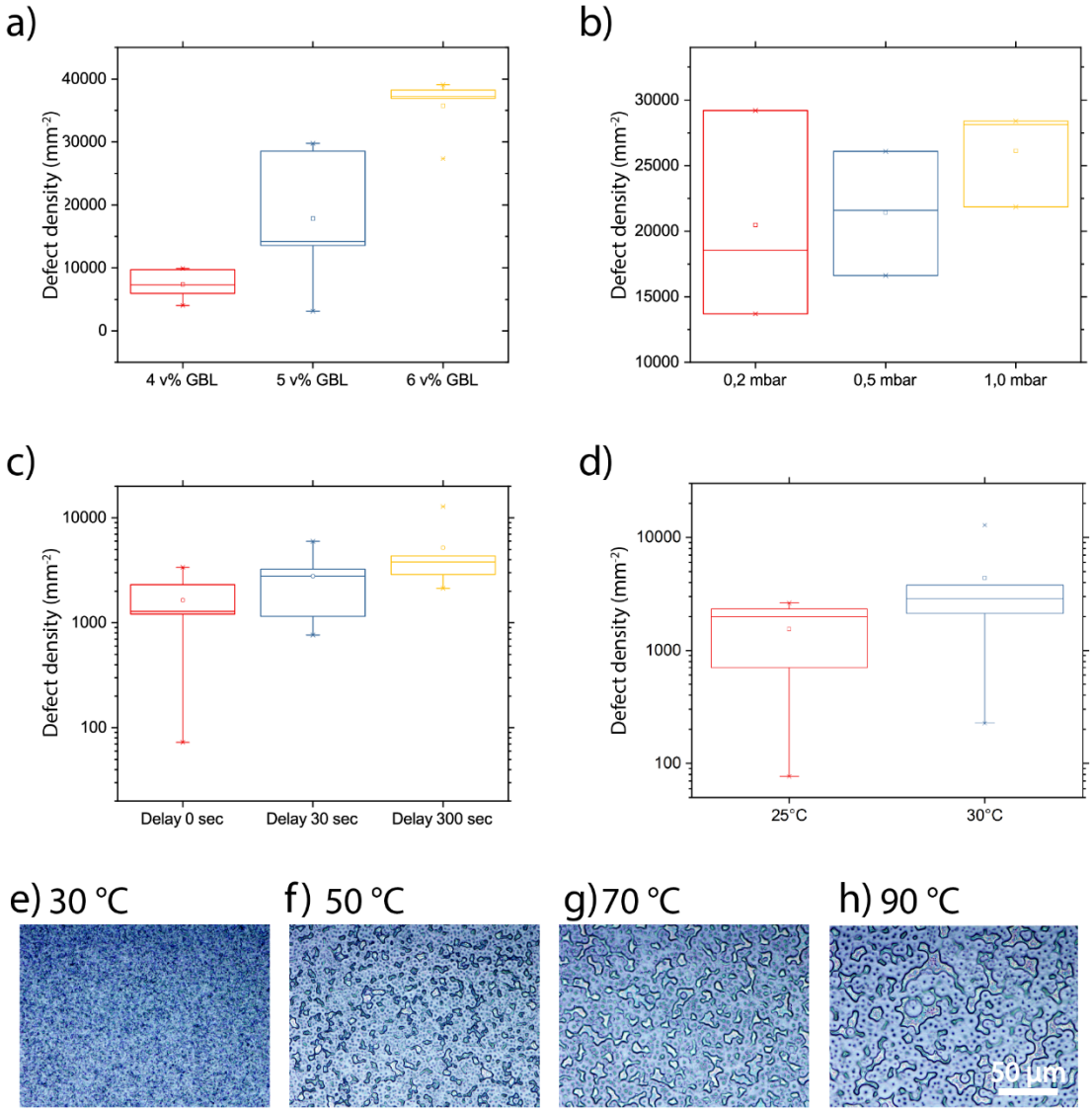

Figure 4.12. Defect density on the samples by each condition. Image a) shows the effect of GBL, where the best conditions occurred at 4 vol.%. Figure b) tested the minimum pressure needed, showing better conditions at 0.2 mbar. Figure c) shows the effect of delaying the vacuum process, where the delay should be ideally as short as possible. Figure d) shows the effect of temperature, where cooler is better. Additional images where the algorithm could not count the defects are shown e) at 30°C for reference, f) 50°C, g) 70°C and h) 90°C.

These images, however, were taken with an uneven source of light which the algorithm is not compatible with. For this reason, all images were flattened with a polynomial fit function, so that shadows resulting from the uneven lighting would be removed. This flattening process is commonly performed on atomic force microscope (AFM) images. Then, a threshold was used to differentiate the defects from crystallites. This step required a manual adjustment to correctly identify the defects on each image. Then the software automatically counted and measured all the recognized defects. The process was partially automatized with a macro, which reduced the

analysis time to about 10 seconds per picture. The analytical procedure was later enhanced and fully automated with a python program which will be described in detail in Section 4.5.2.

The image analysis allowed us to quickly characterize the layers and streamlined the optimization process. Figure 4.12 shows box plots with the distribution of defects for different conditions tested. For reference, the average size of these pinholes was 2 μm^2. First, the content of GBL was optimized from the best value of the previous experiment, shown in Figure 4.10. In this case, a lower amount of GBL, namely 4 vol.% led to cleaner layers. When looking at the effect of the lowest pressure value reached, a pressure of 0.2 mbar led to the most homogeneous layers. It should be noted that pressures as low as 0.05 mbar were reachable with our setup. However, getting to these low-pressure values required exponentially longer amounts of time, for example, of up to 5 minutes to reach 0.1 mbar.

Another important tested parameter was the effect of delaying the start of the vacuum step, shown in Figure 4.12c. This variable is critical because it is directly connected to the sensitivity of the entire process to small delays. The results show that the delay between deposition and vacuum annealing should be as short as possible. It is worth noting that the movement of the robot arm in the pilot plant added an inherent delay of about 65 seconds, which is not considered in these values. Finally, the effect of the vacuum chamber temperature was also tested, finding that the chamber should remain as cool as possible. By increasing the temperature beyond 30 °C, the defect gaps were so large that they did not appear dark enough for the defect-counting algorithm to recognize them, as shown in figures f, g, and h.

The analysis procedure developed for the Vacuum Annealing technique eventually led to the preparation of 1 cm^2 cells with a PCE as high as 10.8%. More information about these and other devices can be found in Section 4.6. Furthermore, some of the improvements accomplished during the optimization process were not fully understood until an in-situ measurement was implemented. For this reason, a more in-detail discussion of these results will be presented alongside the ones obtained with the Flow Control Technique, in Section 4.5.3.

4.5 Flow Control Technique

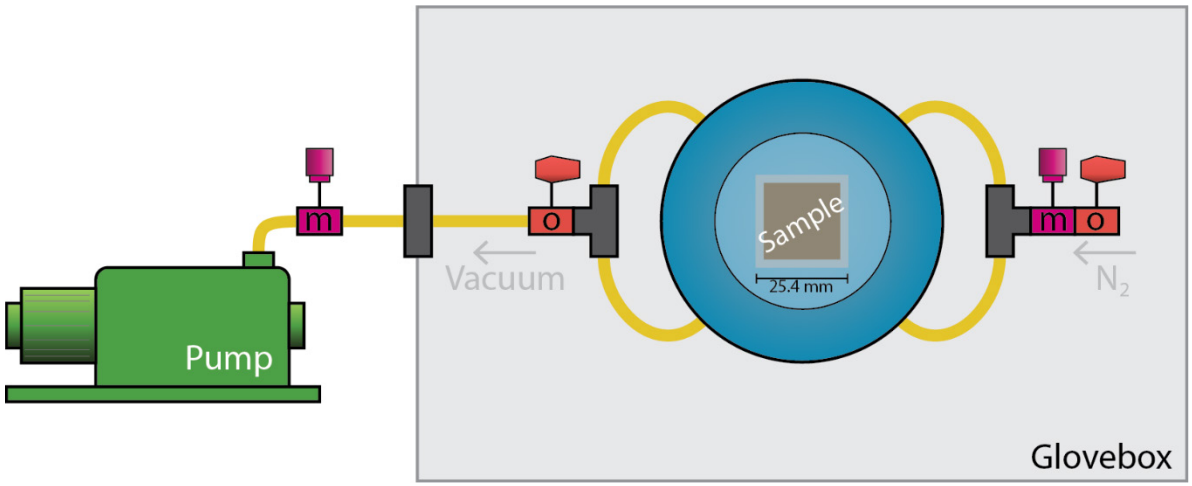

Figure 4.13. Schematic of the Flow Control process. During the drying procedure, a pump (in green) evacuates the nitrogen inside of the chamber (in blue). The pumping rate is controlled with a metric valve (m) and the flow is restricted by a ball valve (o). The freshly printed sample is set to vacuum for 10 seconds. Then, nitrogen from the glovebox refills the chamber through a ball valve (o). The nitrogen flow equalizes with the pumping rate into a specific pressure which is regulated by an additional metric valve (m). This flow continues until the layer becomes dark.

The Flow Control technique was developed to understand the drying and crystallization processes of the inkjet-printed layers. The new chamber is smaller, and samples can be directly inkjet-printed in it. The addition of a quartz glass to the chamber allows a direct view of the sample during the crystallization process. A diagram of this setup is shown in Figure 4.13 and a 3D render of the chamber is found in Appendix 7.4.

In-situ measurements were performed through the quartz glass window in the chamber. Three different sensors were used to characterize the crystallization process of the films: A VD84 pressure gauge by Thyracont, which was connected to the main setup and had a sensitivity range of 100 to 0.001 mbar. Two other probes were used through the quartz window: one was a HD digital microscope that had the possibility of being used as a normal HD camera, and a PL probe attached to an Ocean Optics Flame spectrometer. The PL setup used an excitation light of 475 nm as well as short- and long-pass filters to clean the PL emission signal, as shown in Figure 4.14.

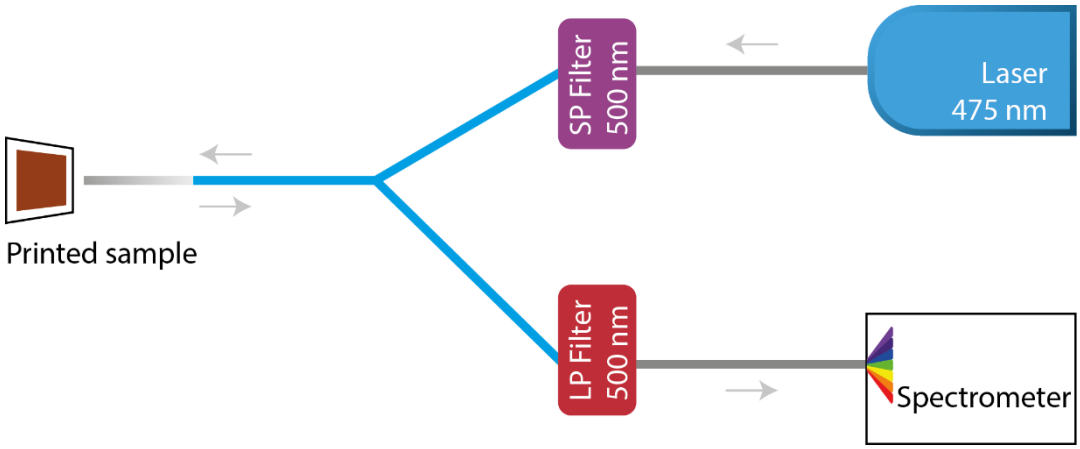

Figure 4.14. Diagram of the PL setup. The light of a 475 nm laser passes through a short-pass filter and then into a reflection probe to excite the sample. The PL emission from the sample goes back through a long-pass filter and into the detector.

To allow the synchronized collection of data from all sensors during the crystallization process, a graphical user interface was developed in python. Other relevant metadata values, like the printer's configuration and the oxygen and water values in the glovebox were also automatically gathered by the program. The code can be found in Appendix 1.1.

4.5.1 Optical In-situ Monitoring

Our earlier understanding of the crystallization process was that solvent evaporation, triggered by a low pressure, was what caused the crystallization on the samples. However, to our surprise this was not the case. The original design of the vacuum chamber considered four vacuum outlets to enable a symmetric extraction of air. Our first tests using this version of the chamber resulted in permanently uncrystallized wet layers. During the process, the wet layers were exposed to a pressure below 1 mbar for as long as 15 minutes without showing a phase change. After carefully analyzing the setup, it was decided to shift two of the chamber outlets into inlets. This allowed us to direct a constant stream of nitrogen from the glovebox into the sample inside the chamber, as shown in Figure 4.13. The flow of nitrogen inside of the chamber is what led to the crystallization of the layers.

Figure 4.15a depicts the effect of the nitrogen flow on the crystallization process. The change of pressure inside of the chamber is shown as a blue line. The change of hue, as recorded by the camera, is shown as an orange line. The pressure inside the chamber goes from 1000 to 1 mbar within 6 seconds and a minimum pressure of 0.35 mbar was held for ca. 100 seconds. To clarify,

the perovskite ink is a translucent yellow liquid that becomes a dark solid after crystallization. This type of absorption, induced by the layer's change of color, is what is being depicted by the orange line in the graph. The repeating spikes of the orange line, after the maximum has been reached, occurred due to the automatic white balance feature of the camera. The camera software compensates the sensitivity of the CCD for lower illumination conditions, a function that cannot be disabled. After 120 seconds, the inlet valve was opened, and the inner pressure of the chamber was equalized to 20 mbar with the entering flow of nitrogen. Here, Figure 4.15a shows a sudden increase of the orange line ca. 13 seconds after the valve was opened, marking the darkening of the layer.

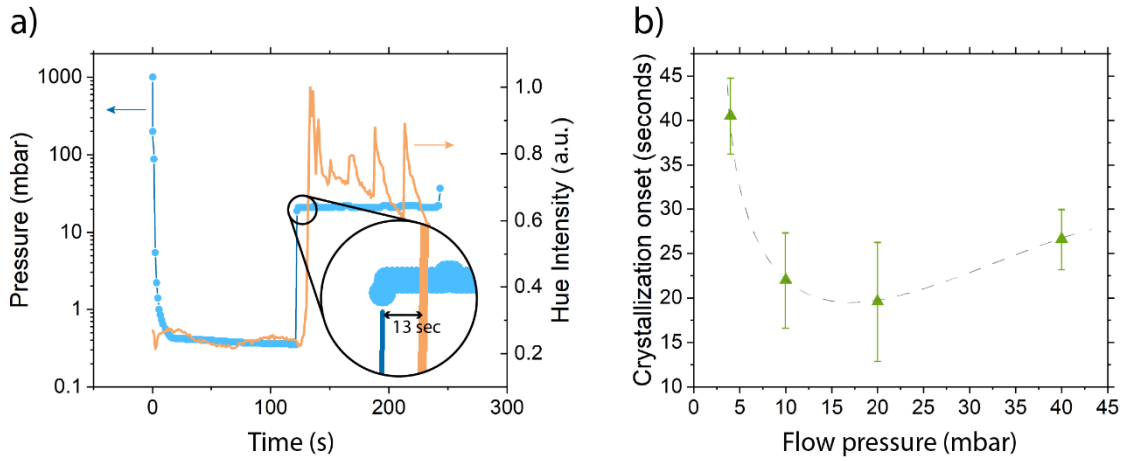

Figure 4.15. Crystallization process of perovskite layers using the Flow Control technique. Figure a) shows the change of pressure and hue intensity as recorded by the camera. Here, the layer turns dark after about 13 seconds from the moment the valve was open. Figure b) shows the time of crystallization on set with respect of the flow pressure, where a 20-mbar pressure resulted in the fastest crystallization.

The equalization pressure, which we call flow pressure, is a novel feature of our process and our setup allows to precisely adjust it within the range of 4 to 46 mbar. Figure 4.15b shows the crystallization onset at flow pressures of 4, 10, 20 and 40 mbar, showing that the crystallization occurs fastest at 20 mbar. Please note that the time of 13 seconds, shown by the example from Figure 4.15a, is considered within the error bars of the Figure 4.15b for a flow of 20 mbar. The increment of crystallization time at a higher flow pressure of 40 mbar corresponds to the nitrogen stream remaining laminar for a longer distance inside of the chamber. In other words, the stream does not touch the sample for a longer distance and time, resulting in an extended crystallization time. This conclusion is supported by the simulations presented in Appendix 7.3, where the flow velocity of nitrogen was set to 0.01, 0.10, and 1.00 L/s. The velocity vectors in the simulation become more parallel with the surface as the flow velocity increases.

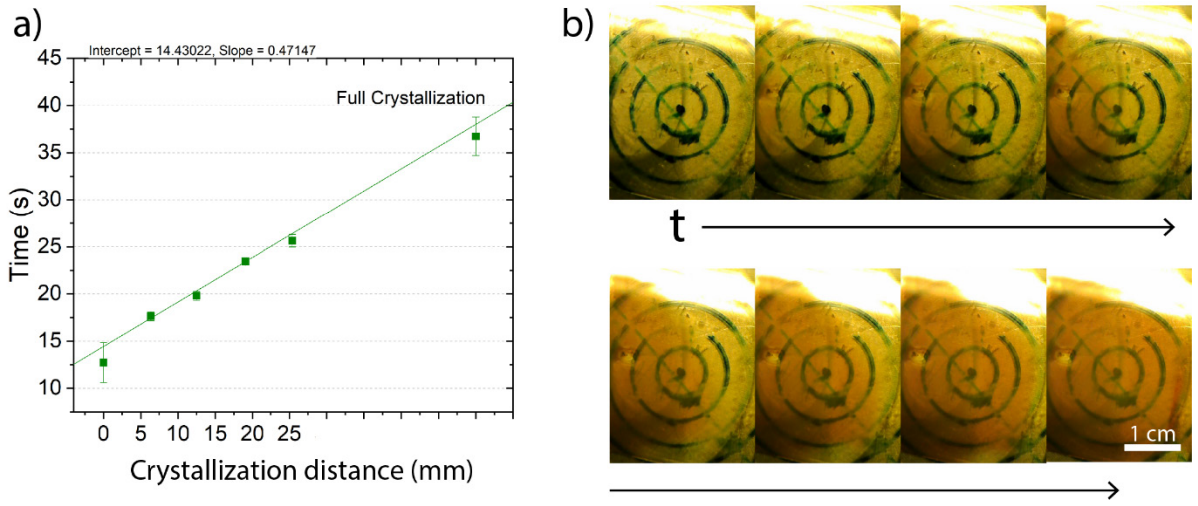

Figure 4.16. Figure a) shows the crystallization speed across the substrate. This process is not homogeneous; hence the "full crystallization" marks the time at which the layers were darker. Figure b) shows pictures of the crystallization process. The concentric rings are guides to the eye. Yellow tones are due to the lighting inside of the glovebox.

The crystallization speed was also measured, having fixed the flow pressure to 20 mbar, as shown in Figure 4.16a. On the substrate, the ink starts to crystallize from the edges nearest to the air inlets. For reference, a simulation of the nitrogen flow inside the chamber is shown in Appendix 7.4. As time passes, the sample then continues to crystallize radially towards the center, as shown in Figure 4.16b. It should be mentioned that the darkening of the layers on these pictures is not so apparent due to the yellow light used to illuminate the glovebox. The crystallization process of the samples occurs mostly linearly. However, it is not uniform since there are some spots that stay translucent for a few seconds longer. This is the reason for the final data point marking the full darkening of the layer, or crystallization.

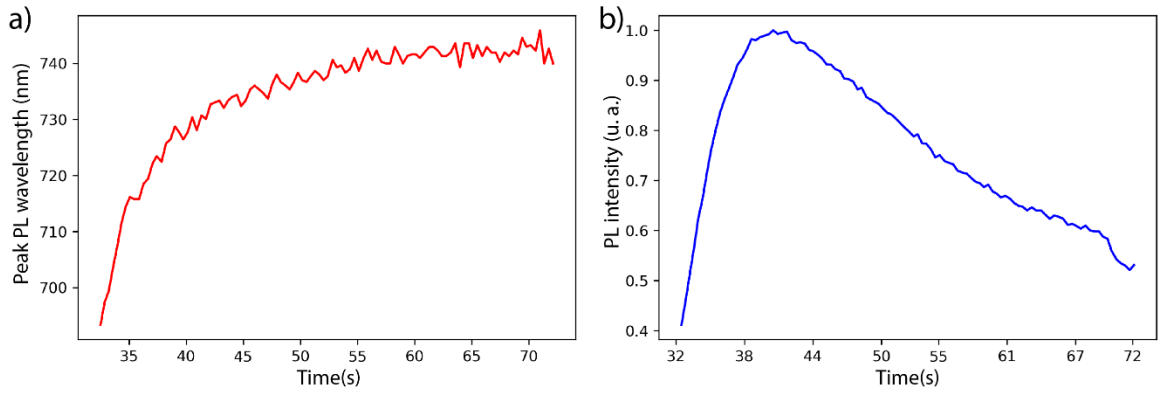

Figure 4.17. In-situ measurements using a PL probe with the Flow Control technique. The graphs show the evolution of a) PL emission and b) PL intensity over time.

The PL probe provides a whole array of novel insight into the crystallization process of the perovskite layers. Figure 4.17 shows the evolutions of PL emission and intensity over time. The curves only encompass the data recorded from the moment nitrogen flows into the chamber. These plots show the existence of emitting species that form in solution during the drying process. Starting with a PL emission at about 690 nm, the PL slowly red shifts as the intensity increases to a maximum when the emission reaches ca. 730 nm. This increment is probably related to the creation of DMSO:PbI_2 adducts during the crystallization process. As DMSO is removed from the layer, the PL emission slowly reduces in intensity as it continues to red shift towards 740 nm. Only after hot annealing the sample at 100 °C for at least 30 minutes, the PL emission of the dry layer at room temperature becomes 760 nm, the typical emission of triple cation perovskite. However, at this point the PL intensity is so low that the spectrometer's integration time must be increased from 100 ms to at least 600 ms to be able to detect a signal.

It is currently not possible to record a video of the PL emission change since the intensity of the excitation light of 475 nm oversaturates the CCD of the camera. However, it is possible to record separate parts of the sample simultaneously.

4.5.2 Pinhole analysis

As discussed in Section 4.4, perovskite layers must be homogeneous and pinhole-free to be able to produce highly efficient devices. To be able to quickly characterize the quality of the printed layers, another program was developed using python. The code can be found in Appendix 7.8. This program took control of the substrate-alignment camera of the LP50 printer to automatically take pictures across the surface of the sample. Additionally, it takes into consideration the size of the substrate, the active area, and the desired number of pictures per side. Our standard procedure contemplates a side of 25.4 mm per substrate with an active area of 20 mm per side. A total of 25 pictures are taken across the sample, as shown in Figure 4.18a.

The pictures are taken across the sample using two different types of light: coaxial and ring. Coaxial light uses a single light source pointed perpendicularly to the surface. This type of light provides a morphological visualization of the surface, as shown in Figure 4.18b. On the other hand, the ring light uses three light sources in a triangular shape equidistant to the center. This type of lighting enhances the view of reflective surfaces, as it is the case of the substrate. Hence,

this light is used to quantify the number of pinholes, or gaps, that cross over the sample's surface.

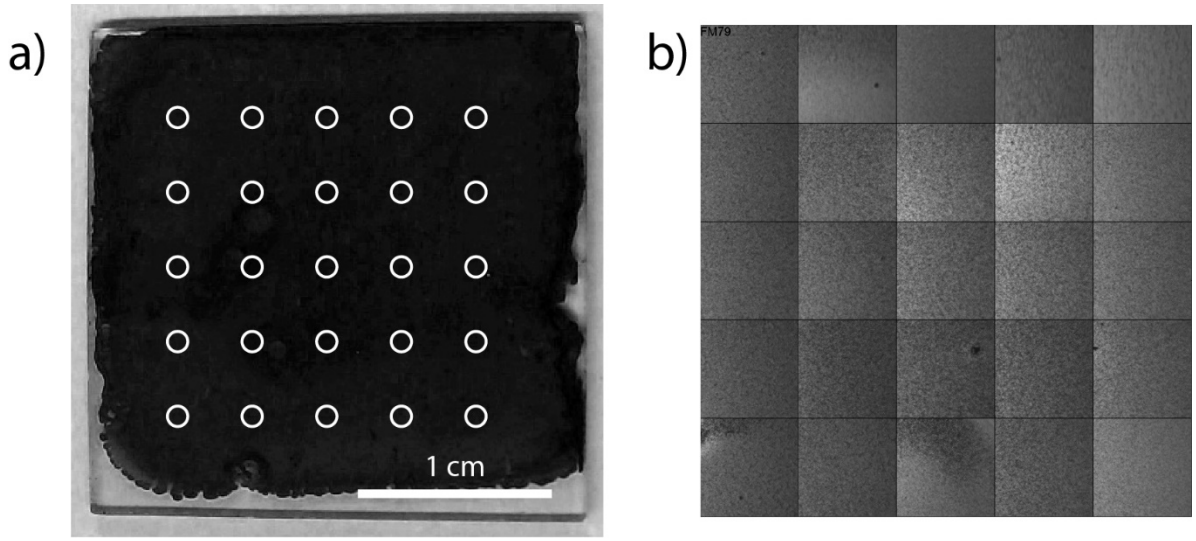

Figure 4.18. Images of a) the substrate, showing the 25 spots where pictures are automatically taken across the surface of the sample and b) a composite image showing the central region of the 25 pictures taken with the program.

After the pictures have been taken, the python program analyzes the images. Here, the images are converted to grayscale to facilitate the recognition of dark spots. Due to the inhomogeneity of the images lightning, as seen in Figure 4.19a, each pixel value is divided by a reference image to flatten the images' light variation. The contrast of the shadowless images is then mathematically enhanced by normalizing the value of the pixels. Finally, an algorithm that uses the library OpenCV and adaptive thresholding is applied to identify, count, and measure the size of the defects.

The python program is able to quantify and measure all the patterns that stand out the threshold, as shown as magenta for the coaxial light in Figure 4.19a, and yellow for the ring light in Figure 4.19b. Unfortunately, this process is not perfect. Sometimes there are false positives and defects that are not counted. We assume that in 25 pictures the number of false positives and negatives cancel each other out. The program then returns the total number of defects and their average area for each picture taken. An example of the number of defects found on each one of the 25 pictures for each light is shown in Figure 4.19d and e. The statistics of the data is later compared for each one of the tested conditions.

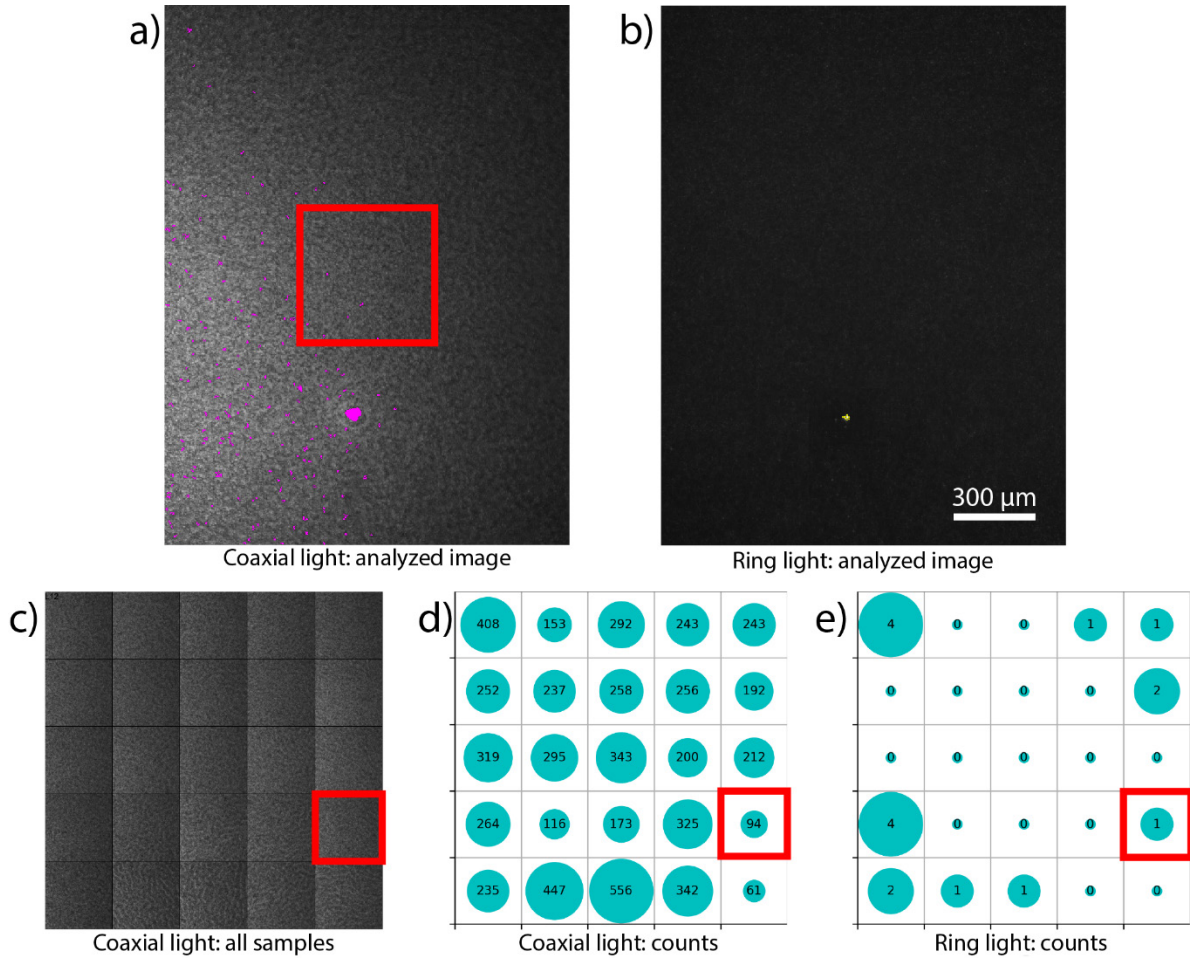

Figure 4.19. Analysis of defects using a) coaxial and b) ring lights. The fact that b) is mostly black is positive since this type of light enhances the number of pinholes that traverse the layer. Image c) shows a composed image of the 25 pictures taken across the sample. Each one of the images here correspond to an area equal to the red square, with side of 500 microns, marked on figure a). The total number of defects counted for each type of light are shown in d) and e). The red squares on these images show the counts from the images shown on a) & b), respectively.

4.5.3 Parameter Optimization

The first step on our process was to find the best printing resolution and ink concentration to achieve a complete substrate coverage and layer thickness. This is shown in Figure 4.20. Resolutions of 250, 300, 350 and 400 DPI were tested, having all showed a complete coverage of the substrate. By increasing the density of printed droplets with the resolution, the thickness of the layer increases, as shown in Figure 4.20a. However, as the layer becomes thicker, it also becomes rougher, as marked by the large error bars. However, this roughness was not clearly visible by eye, as shown in Section 4.1.1, where a worm-like pattern appears if the layers are thicker than 900 mm.

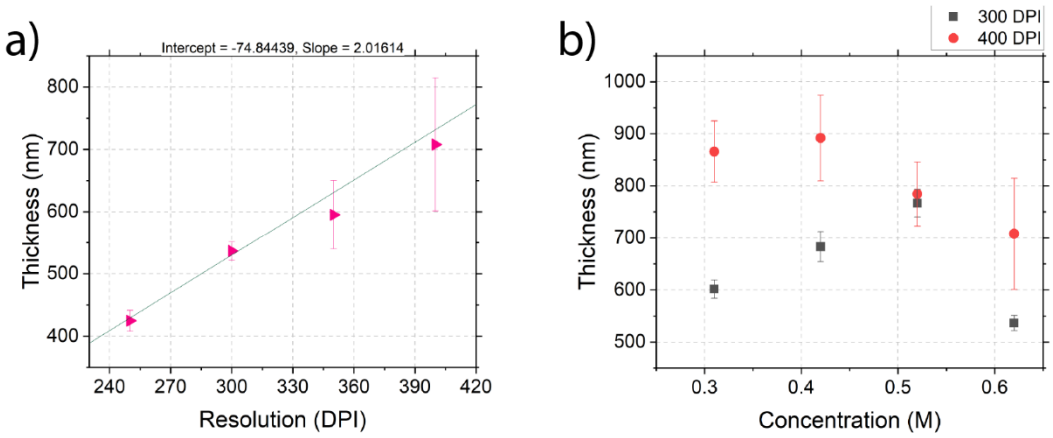

Figure 4.20. Effect of the printing resolution and the ink concentration on the thickness of the dry printed layers.

Moreover, by changing the concentration of the precursors on the ink a couple of unexpected effects happen. As shown in Figure 4.20b, a higher DPI results on a thicker layer overall. However, the dry layer thickness reduces with concentration when printing with 400 DPI. On the other hand, for a lower DPI of 300, the dry thickness of the layers partially increases with concentration, but it reduces when the concentration is 0.62 M. This is due to the drying mechanics of the ink. As mentioned in Section 2.1.3, there is a strong interaction of the precursors with the solvent. The concentration of the precursors seems to directly affect the way in which the solvent is removed. When the concentration of solutes is too high, the viscosity likely increases enough to limit the movement of ions, resulting in smaller crystals. Further experiments are needed to conclusively prove this effect.

The content of GBL on perovskite inks was examined by two metrics using the Flow Control technique: the time until the layers became completely dark – time until full crystallization, and the thickness of the dry layers, shown in Figure 4.21. By keeping the perovskite concentration constant to 0.52M and the solvent ratio of DMF:DMSO to 4:1, GBL was added to the solution in concentrations of 10, 25, and 40 vol.%. The results showed that a higher amount of GBL present on the perovskite ink reduces the crystallization time. At the same time, the dried layers emerging from the lower amounts of GBL had comparable thicknesses but larger error bars, showing that these layers are rougher. The reason that a larger amount of GBL leads to longer crystallization times is because DMSO forms strong complexes with the perovskite salts, which are harder to break.[235] By increasing the amount of GBL, the complexation of the lead salts to DMSO becomes more diluted and less tightly bound.

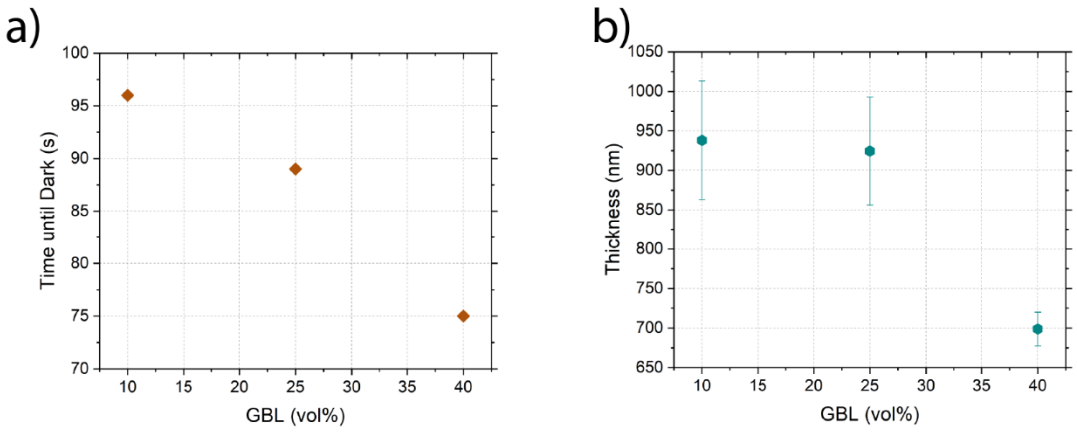

Figure 4.21. Effect of GBL on crystallization of perovskite layers on the a) crystallization time and b) the dry layer thickness. Crystallization time is higher for a large concentration of GBL on the ink. However, for the two lowest concentrations of 10 and 25 vol.%, the layer thicknesses were comparable.

By comparing the effect of GBL measured using the Flow Control technique with the one obtained with the Vacuum Annealing technique, where the optimized process contained a GBL concentration of 4 vol.%, we conclude that the best GBL content is highly dependent on three aspects: the vacuum chamber size, the refilling rate, and the direction of the refilling flow. For instance, when the glovebox antechamber was used as a Vacuum Annealing chamber, an ink containing 50 vol.% of GBL led to good quality layers. This antechamber had a volume of about 14 L and a slow evacuation rate of about 2-3 minutes to reach 0.2 mbar. Also, the refilling inlet is located at one of the edges of the chamber, not pointing directly at the sample. In a different case, when using a large vacuum chamber of 23 L, with a fast evacuation rate of about 40 seconds until 0.2 mbar was reached, an ink with 4 vol.% of GBL lead to good quality layers. The refilling inlet in this case was also not pointing to the sample. Alternatively, the Flow Control technique was done in a chamber of about 0.25 L with an evacuation time of about 10 seconds and two streams of air that pointed directed at the sample. The content of GBL required for high efficiency cells in this situation was 25 vol.%. In other words, while using the same printer and ink solutions, the required content of GBL changed with the chamber specifications.

The effect of the flow pressure on the crystal quality was tested by first setting the vacuum chamber to a pressure below 1 mbar and after 10 seconds letting a stream of nitrogen with pressures of 4, 10, 20 and 46 mbar into the chamber. The results are shown in Figure 4.22a. In general, most samples show less than 100 defects per image. However, a flow pressure of 20 mbar led to fewer defects, being below 10 defects per image. With a high flow pressure of 46 mbar, the number of defect increases slightly, although there were samples that showed more

than 100 defects per image, probably due to the movement of the wet layer induced by the stream of nitrogen as it dries. Since this is an ongoing research topic, we do not have sufficient data yet to say how many defects per sample are acceptable for a highly efficient device.

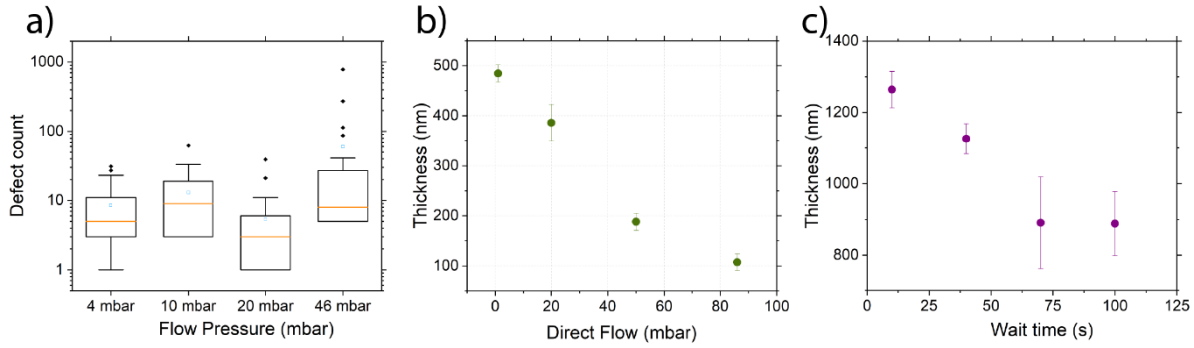

Figure 4.22. Results from the Flow Control technique. Figure a) shows the number of defects per images using the coaxial light. It compares the effect of the flow pressure intensity at which the layers are dried, finding that 20 mbar led to fewer defects. Figure b) shows the effect of the flow process. When the process starts with a vacuum, it leads to larger crystal sizes than by just applying a direct flow to the sample. Figure c) shows the change of layer thickness with respect to the delay time to start the vacuum process, finding that the shortest delay time led to the thickest layers.

As mentioned earlier, our process considers a first vacuum step before applying a stream of nitrogen to the sample. The importance of this vacuum step was tested in a different experiment, where the results are shown in Figure 4.22b. The data shown at 0 mbar followed the standard procedure of leaving the sample 10 seconds under an active vacuum. All the other samples were subjected to a direct flow of 20, 45, and 84 mbar as soon as the printing process finished. The results showed that the sample that was held first on a vacuum resulted in thicker layers, a sign of better crystal formation. It should be mentioned that streams higher than 40 mbar resulted in a visible movement of the wet layer in direction of the nitrogen flow, resulting in a considerable thickness reduction of the final dry layer.

The effect of delaying the start of the vacuum process was also tested on both techniques, the Flow Control, and the Vacuum Annealing techniques. Our results showed that the best quality layers were obtained when the delay was as small as possible, as shown in Figure 4.22c. The fastest reproducible time for the Flow Control technique was 10 seconds since the chamber needed to be closed and the valves set. Lower wait times resulted in the largest crystals and thickest layers for both techniques. Additional supporting SEM images are found in Appendix 7.1, where top and cross-sectional images of the layers are shown. On the other hand, long delay times resulted in uneven layers, as shown on the increasing error bars shown on the plot.

The list of all optimized parameters used for the Flow Control technique is shown in Table 4.1. Optimized parameters for the other techniques are found in Section 4.2.

Table 4.1. Optimized parameters for the Flow Control technique.

Optimized parameter	Value	Comments
Wait Time	10 seconds	Smallest reproducible amount of time
Vacuum time	10 seconds	
Vacuum rate	99 mbar/s	To a minimum pressure of 0.4 mbar
Resolution	300 DPI	
Ink concentration	0.42 M	
Solvent mix	DMF:DMSO:GBL with ratio of 4:1:1.667	This is 25 vol.% GBL
Flow temperature	20 °C	Glovebox temperature
Flow pressure	20 mbar	
Flow time	60 seconds	
Hot annealing temperature	100 °C	
Hot annealing time	30 minutes	

4.6 Solar Cell Devices

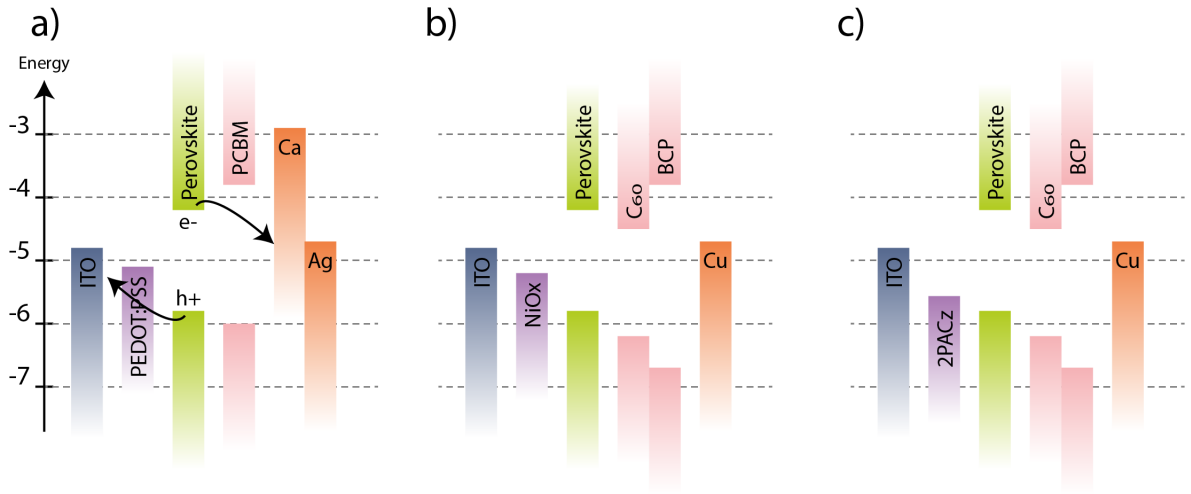

Figure 4.23. Energy levels of materials used for solar cells in an n-i-p architecture.

Devices were prepared using a triple cation ink that was crystallized using only two techniques: Vacuum Annealing and Flow Control. All devices had a p-i-n architecture, see Section 2.2.1. The inkjet printing process was optimized for four hole transport layers (HTLs): poly(3,4-ethylene dioxythiophene) polystyrene sulfonate (PEDOT:PSS),[236] nickel oxide (NiOx),[237] poly(triaryl amine) (PTAA),[238] and a self-assembled monolayer (SAM) of [2-(9H-carbazol-9-yl)ethyl]phosphonic acid (2PACz).[239]

Samples prepared with PEDOT:PSS as HTL were later spin-coated with $PC_{60}BM$ as electron transport layer (ETL) and evaporated combination of calcium and silver as metallic contacts. All other devices were evaporated with fullerene C_{60} and bathocuproine (BCP) as ETLs, and copper as the metallic contact. For more details, see Section 4.2. The structures and energy levels of the materials used on these devices are shown in Figure 4.23.[217] All of these HTL layers showed strengths and weaknesses, and they will be discussed in the following paragraphs.

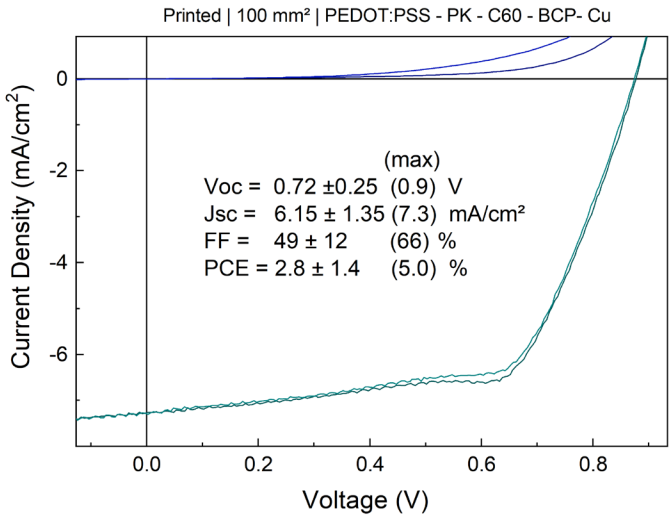

Figure 4.24. JV characteristics of best inkjet-printed devices using an HTL of PEDOT:PSS.

PEDOT:PSS is a biocompatible material[240] that is usually dissolved in water, and that has been widely used in photovoltaics. Deposition has been demonstrated by inkjet printing.[241] Some additives can be used to improve the efficiency of perovskites devices, as it is the case for imidazole, which is used to tune the work function of the material and to increase the wetting of the perovskite.[242] Even without additives, this layer showed good wetting properties with the perovskite inks. On the downside, the PSS part of the material is highly hygroscopic and tends to absorb of water from the surroundings.[243] This reduces the stability of the perovskite structure

over time.[244] Hence, this setup requires robust encapsulation methods and very high purity atmosphere levels on the gloveboxes. PEDOT:PSS-based devices fabricated with the Vacuum Annealing process showed decent fill factors above 60%. However, low short circuit currents of at most 8 mA/cm² and an open circuit voltage below 0.9 V, resulted in low efficiency devices, with a maximum of 5% PCE, as shown in Figure 4.24.

PTAA is an easy to prepare HTL whose deposition has only been shown by spin coating. It became widely popular due to its superior charge transport characteristics and after reproducible 20% cells were demonstrated.[238] On the downside, the wetting of the perovskite ink is extremely poor. Such poor wetting is manageable for spin-coated samples because a generous amount of the perovskite solution can be manually spread across the substrate before processing. However, inkjet droplets would not merge on these layers, as shown in Figure 4.1b. These layers can be treated to enhance their wettability, for example, by ozone plasma treatment. However, this process effectively changes the surface properties of the material, dramatically reducing the charge transfer characteristics and leading to poor efficiencies below 4%.

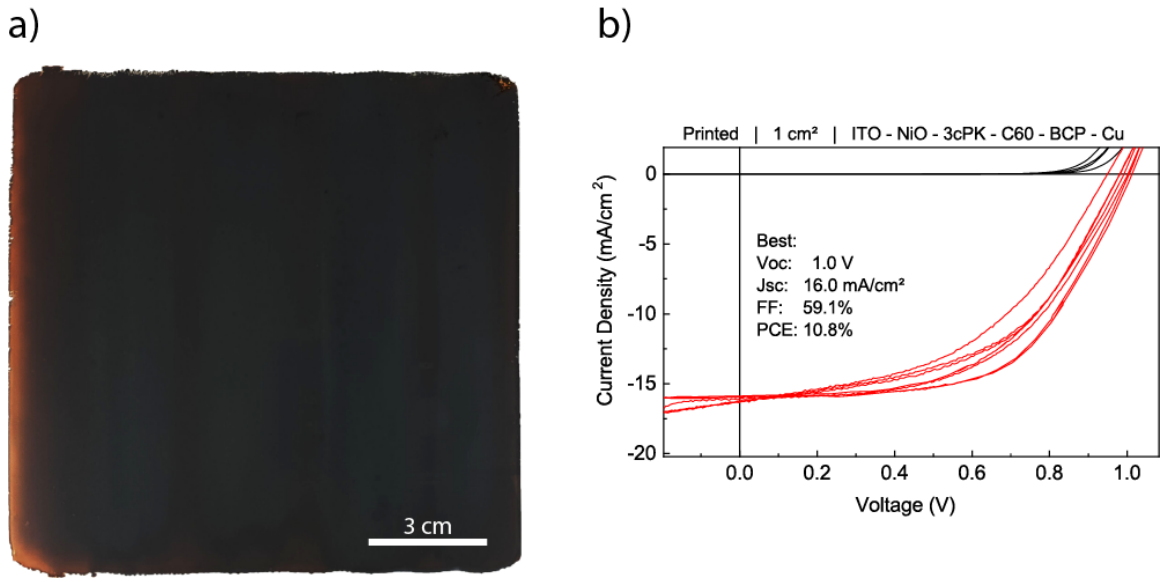

Figure 4.25. a) Picture of layer quality printed on a 15x15 cm² substrate. The lack of features or defects manifests the high quality of the layer. Figure b) shows the JV characteristics of the best inkjet-printed cell using the Vacuum Annealing technique on NiOx with an active area of 1x1 cm². 3cPK stands for triple cation perovskite.

NiOx is a material that showed many advantages, such as the chemical stability, a good energy band alignment with the perovskite, and its low cost.[245] It also showed good wetting with inkjet-

printed layers. However, it was not possible to coat the substrates with NiOx in our lab and had to depend on project partners to get a supply of substrates.

Using the Vacuum Annealing technique we demonstrated the successful deposition of homogeneous perovskite layers on a 15x15 cm² area, as shown in Figure 4.25a. Furthermore, a maximum PCE of 10.8% on a 1 cm² solar cell was achieved, shown in Figure 4.25b. Noteworthy is the low fill factor, mostly due to the high shunt and low series resistances. However, the short circuit current on these layers was still too low, at about 17 mA/cm².

Figure 4.26 contains x-ray diffractograms and SEM images from the large sample with an area of 15x15 cm². The diffractogram in Figure a) shows a small peak near 12° and a large one near 14°, corresponding to a reflection of [002] of lead iodide and [110] of a cubic perovskite phase, respectively.[246] This suggest that the crystallization process is appropriate. However, the small crystals shown in Figure b), with average diameter of 100 nm, suggest that drying process could be further optimized to obtain larger crystals that would allow more light absorption and increase the current from the devices.

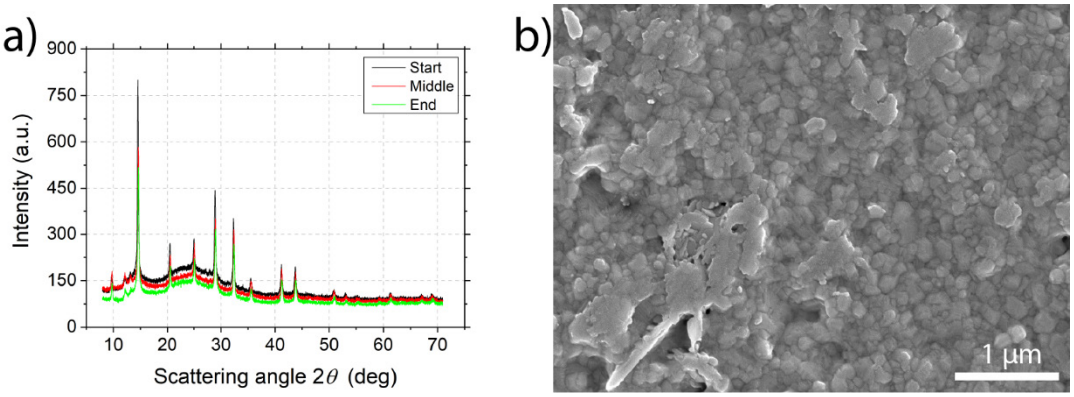

Figure 4.26. Figure a) shows x-ray diffractograms of a triple cation perovskite printed on a 15x15 cm² substrate. The diffraction patterns correspond to a point near the place where the printing process started, the middle and the end. Figure b) shows an SEM image of the texture typically seen throughout the same sample.

Best Device

The successful use of 2PACz SAM as HTL was first demonstrated by one of our colleagues. This layer aligns energetically with the perovskite and avoids non-radiative losses.[219] The layers are deposited by spin-coating and the material is compatible with a large variety of substrates. On the downside, perovskite needs to be deposited on these layers as fast as possible, since the

wettability reduces within hours of having prepared them. The typical stack of these devices is shown in Figure 4.27.

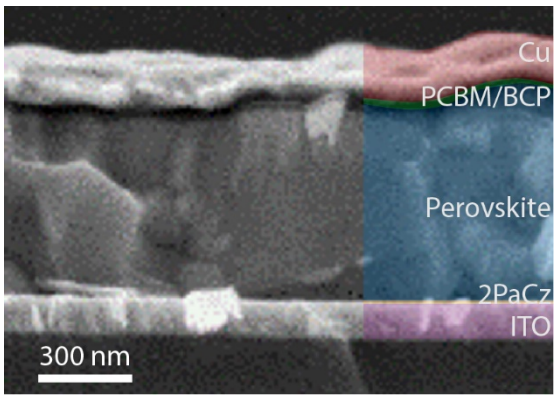

Figure 4.27. Cross-sectional SEM image of an inkjet-printed solar cell. False colors are used to identify the layer materials used on these devices.

Using the Flow Control technique, devices prepared with this SAM have shown the best performance yet. As shown in Figure 4.27, the crystal size of the samples prepared with this technique are larger than the ones prepared with the Vacuum Annealing technique. The best solar cell showed a maximum PCE of 16.8% was achieved on an area of 0.16 cm², as shown in Figure 4.28.

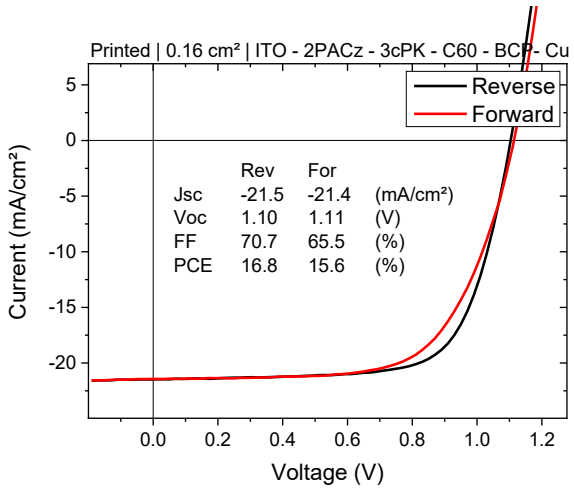

Figure 4.28. JV characteristics of a 0.16 cm² cell inkjet printed on a 2PACz SAM.

Stabilized MPP tracking was achieved at 16%, shown in Figure 4.29a. Also, the distribution of efficiencies achieved by all printed samples, depicted in Figure 4.29b, show that the average performance was 11.3%. Worth noting is that a large number of devices had efficiencies above 15%. The distributions of other parameters are found in Appendix 7.5.

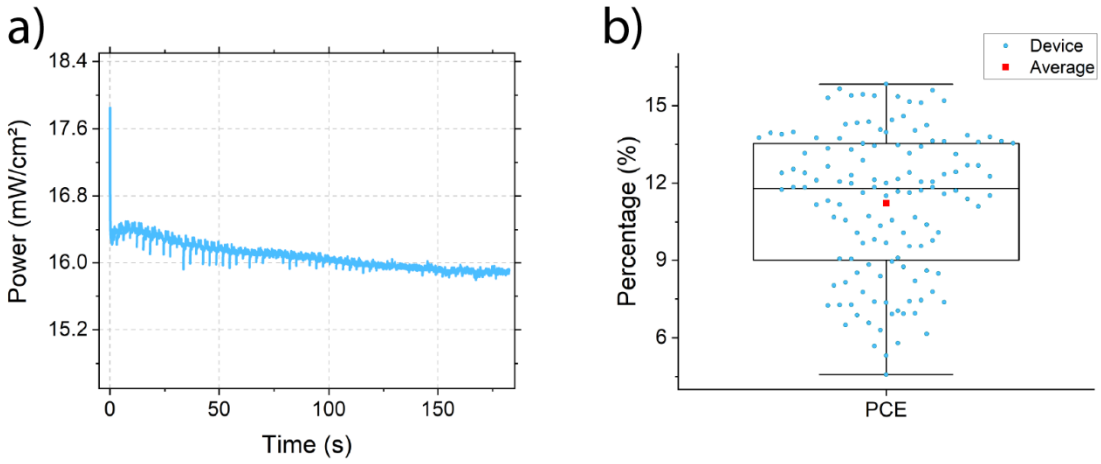

Figure 4.29. a) Plot of MPP tracking of best device and b) distribution of efficiencies achieved by all samples crystallized with the Flow Control technique.

The Flow Control technique is still under development. The results presented here show that this technique is a promising candidate for the preparation of high efficiency devices. However, as discussed on the previous results, it is still necessary to finalize the optimization process to increase the reproducibility of the results and the efficiency of the devices. The efforts are focused on reducing the number of defects on the layers and increasing the crystal sizes, so that the short circuit current is increased. Moreover, increasing the quality of the crystals will also result in the enhancement of the short circuit current as well as the open circuit voltage.

4.7 Conclusion

To summarize, we tested three methods to enhance the crystallization of deposited perovskite layers by inkjet printing. The first method required a two-step deposition of the precursors: first a highly concentrated ink of PbI_2 and a second less concentrated ink of MAI. The individual printing process of these inks led to visibly good layers. However, by combining the printing processes of the two inks, the resulting layers were too rough to be used for devices.

Next, two other crystallization techniques were used on inkjet-printed layers that were deposited by a single step. The first one was the Vacuum Annealing process, where a large chamber with a volume of 23 L was used for the vacuum process. Using this technique and a comprehensive optimization process, devices based on a NiOx HTL reached a maximum

efficiency of 10.8% in a 1 cm² area. Additionally, the deposition of a smooth layer on an area of 15x15 cm² was demonstrated.

Finally, the Flow Control technique implemented a new chamber with valves that allowed the precise control of nitrogen flow inside the chamber. The addition of a quartz glass to the chamber allowed the direct visualization of the crystallization process. With this, we found that the crystallization process is triggered by the nitrogen flow and not by the low pressure, as previously thought. Additionally, we found that during the flow process emitting species are formed in solution and that their emission red-shifted and reduced in intensity as the layer dried. Using a self-developed analysis of layer defects and other characterization methods, the deposition of the layers was optimized. A sample with an efficiency of 16.8% on an area of 0.16 cm² on a 2PACz SAM was achieved.

Future work will encompass the further optimization of the drying process, since key changes can result in the formation of larger crystals and reduction of defects. Moreover, additives like FACl will be tested to enhance the quality of the layers, as shown by other experiment done by spin coating. Lastly, the process will be extended to larger areas. First, by demonstrating a higher efficiency than the current record of 12.3% on an area of 1 cm², and by elaborating modules with active areas of 5x5 cm², 15x15 cm², and 40x40 cm².

5 Conclusion & Outlook

Metal halide perovskites (MHPs) are versatile materials that have unique characteristics, like bandgap tunability, a high absorption coefficient, extended lifetimes, long diffusion lengths, and a high defect tolerance. Although the perovskite structure has been known for more than a century, their development as semiconductors was accelerated in the last couple of decades. Today, MHPs show power conversion efficiencies that are comparable to other well-established photovoltaics materials. Yet, there are still issues that need to be addressed, like poor stability under ambient conditions as well as limited efficiencies as the active area increases.

The work presented in this thesis investigated these two aspects. First, the stability of metal halide perovskites was studied by measuring the photoluminescence quenching mechanisms of common atmospheric gases. Second, the large area deposition of highly efficient perovskite photovoltaics was explored via inkjet printing.

The effect that common atmospheric gases like molecular oxygen, molecular nitrogen, argon, and water in the form of water-enriched argon had on metal halide perovskite layers was analyzed in chapter 3. It was found that the photoluminescence (PL) emission of MHP crystals strongly decreased under the presence of oxygen and water. Furthermore, nitrogen and argon also induced a reduction of PL intensity, albeit small. The quenching effect of these inert gases had not been previously reported. It is necessary to note that the PL quenching effect was fully reversible for all gas molecules, except for oxygen, which showed a minor permanent reduction of PL intensity after having been exposed to the gas for the first time. By using higher quality crystals, that is with a higher PL quantum yield, a passivation effect was found at pressures above 300 mbar for all molecules. Moreover, by comparing the emission of a single crystal and polycrystalline layers, it was found that boundary defects play a key role on the quenching and passivation effects. Gas molecules can easily bind to these regions and allow energy to be

transferred. Applying the Stern-Volmer analysis to the results revealed key aspects of the quenching mechanisms. For instance, it was found that PL quenching occurs mostly in a static manner, meaning that the gas molecules temporarily bind to the perovskite crystals. However, in the case of oxygen, a portion of these molecules bind to iodide vacancies in the lattice permanently, reducing the PL emission of the layers by about 20%. In the same token, it was found that water molecules have a slightly more dynamic type of quenching, meaning that a larger portion of water molecules do not bind to the perovskite crystals, but tend to bounce more off them. Evidence of passivation effects on multiple experimental results show that all static and dynamic quenching, as well as passivation effects are taking place simultaneously with distinct strengths at different concentration ranges. The bimolecular quenching coefficients of each one of the gases were calculated, showing that they are all below the diffusion limit of 10^{10} M^{-1} s^{-1}. This indicates that the quenching processes are not efficient. Moreover, the coefficient for oxygen is comparable to what has been measured on other materials, like the Poly(3-hexylthiophen-2,5-diyl) (P3HT). By analyzing the results obtained from the measurements and calculations, energy transfer mechanisms were proposed for each one of the tested molecules. Namely, energy is transferred to oxygen molecules by electronic energy transfer, to water the energy transfer is redox mediated, and to argon and nitrogen, the energy transfer occurs as Van der Waals induced distortions with the perovskite lattice. This information is builds up on the understanding of the quenching mechanisms that occur on perovskite materials and introduces the Stern-Volmer model as a tool to quantify the passivation effects of molecules and materials used to reduce non-radiative recombination and increase the overall stability of perovskite devices.

On the second part of the thesis, the deposition of MHPs via inkjet printing was explored in Chapter 4. Three different techniques to enhance the crystallization process of metal halide perovskites were discussed. The first one encompassed the deposition of two separate inks that react to form a perovskite layer when combined. Although this technique resulted in smooth layers when printing each step separately, combining the printing process of both resulted in rough layers, of up to 1 mm in height, making these layers unsuitable for device preparation. The second and third techniques involved a single deposition of ink, simplifying the overall process of deposition. These techniques were successfully used on the preparation of devices and varied by the way in which crystallization was induced. The first one, a Vacuum Annealing technique, resulted in smooth layers that after optimization resulted in 1 cm^2 area devices with a power conversion efficiency of 10.8%. This technique later evolved into the Flow Control

technique, where a specially designed chamber permitted the control of nitrogen flow inside a chamber. This chamber also contained a quartz glass window that allowed in-situ measurements during the crystallization process. With this, it was found that the crystallization is induced by the flow of nitrogen inside of the chamber, as opposed to evaporation induced by a low pressure. Additionally, the formation of emitting species in solution was found during the crystallization process. Starting with an emission of about 690 nm, the emission slowly red-shifted. An emission of 760 nm, the typical emission of triple cation perovskite, was only reached after the layers were hot annealed for at least 30 minutes. At this point, the intensity reduced in such a way that the integration time of the spectrometer needed to be increased by 6 times to be able to measure a distinguishable signal. For the characterization of these layers, an analytic process was developed where images were automatically taken across the dried layers, and an algorithm later analyzed and quantified the number of defects found. Using this approach, alongside to SEM images and profilometer measurements, the layers were optimized to finally produce inkjet-printed devices with an efficiency of 16.8% on an area of 0.16 cm^2 using a self-assembled monolayer as hole transport layer. From these results, the viability of using inkjet printing as an upscaling method to accomplish high performance devices was demonstrated.

Outlook

Understanding the PL quenching mechanisms on MHPs is a crucial step to enhance the stability of perovskite devices under different atmospheres. For this, three different energy transfer mechanisms were proposed for each one of the molecules evaluated. However, further experiments are necessary to unmistakably identify these processes, especially in the case of argon and nitrogen, where the energy transfer mechanisms have not been thoroughly investigated.

Having understood the energy transfer pathways from an excited perovskite crystal to a quencher molecule, it is also necessary to find the proper ways of avoiding them. In this sense, many groups have already proposed additional molecules and ions that can be used to enhance the stability of the MHPs. However, this thesis introduces the use of the Stern-Volmer analysis, a tool that can be used to quantify the passivation efficacy of the different proposed procedures and thus find the best molecules and techniques to override the effect of atmospheric molecules on the crystals.

Regarding the inkjet printing process, the implementation of the new Flow Control technique opened a new window into the understanding of the crystallization process. However, it is still necessary to continue with the optimization process to reach efficiencies comparable to the ones done by spin coating. The use of additives, like formamidinium chloride (FACl), can also be explored to enhance the wettability, stability, and efficiency of the devices. Using advanced characterization techniques such as x-ray diffraction alongside the in-situ PL spectroscopy, could be used to identify the exact composition of the emitting species in solution formed during the drying process of the layers to deepen the understanding of this process. Additional work is also necessary to demonstrate consistent high efficiencies, first on a 1 cm^2 area, and then on modules of 5x5, and 40x40 cm^2.

6 References

1. Appunn, K., Haas, Y. & Wettengel, J. Germany's energy consumption and power mix in charts. https://www.cleanenergywire.org/factsheets/germanys-energy-consumption-and-power-mix-charts (2020).

2. Chen, Y., Zhang, L., Zhang, Y., Gao, H. & Yan, H. Large-area perovskite solar cells – a review of recent progress and issues. *RSC Adv.* **8**, 10489–10508 (2018).

3. Case, C., Beaumont, N. & Kirk, D. Industrial Insights into Perovskite Photovoltaics. *ACS Energy Lett.* **4**, 2760–2762 (2019).

4. Wohlgemuth, J. H. *Photovoltaic Module Reliability*. *Photovoltaic Module Reliability* (Wiley, 2020). doi:10.1002/9781119459019.

5. Rötger, A. World Record: Efficiency of perovskite silicon tandem solar cell jumps to 29.15 per cent. *HZB Press releases* https://www.helmholtz-berlin.de/pubbin/news_seite?nid=21020;sprache=en;seitenid=72384 (2020).

6. Best Research-Cell Efficiency Chart. *NREL* https://www.nrel.gov/pv/cell-efficiency.html (2020).

7. Islam, M. B., Yanagida, M., Shirai, Y., Nabetani, Y. & Miyano, K. Highly stable semi-transparent MAPbI3 perovskite solar cells with operational output for 4000 h. *Sol. Energy Mater. Sol. Cells* **195**, 323–329 (2019).

8. Zhang, M. *et al.* Electrode Design to Overcome Substrate Transparency Limitations for Highly Efficient 1 cm2 Mesoscopic Perovskite Solar Cells. *Joule* **2**, 2694–2705 (2018).

9. Paetzold, U. W., Richards, B. S. & Hernandez-sosa, G. Perovskite Solar Cells with All-Inkjet-Printed Absorber and Charge Transport Layers. (2020) doi:10.1002/admt.202000271.

10. Alexandra Navrotsky, D. J. W. Perovskite: A Structure of Great Interest to Geophysics and Materials Science. *Geophys. Monogr. Ser.* (1873) doi:10.1029/GM045.

11. *Perovskite Oxide for Solid Oxide Fuel Cells*. (Springer US, 2009). doi:10.1007/978-0-387-77708-5.

12. MØLLER, C. K. Crystal Structure and Photoconductivity of Cæsium Plumbohalides. *Nature* **182**, 1436–1436 (1958).

13. Mitzi, D. B., Wang, S., Feild, C. A., Chess, C. A. & Guloy, A. M. Conducting Layered Organic-inorganic Halides Containing <110>-Oriented Perovskite Sheets. *Science (80-.).* **267**, 1473–1476 (1995).

14. Mitzi, D. B., Chondroudis, K. & Kagan, C. R. Organic-inorganic electronics. *IBM J. Res. Dev.* **45**, 29–45 (2001).

15. Abstracts, E. C. S. M. Novel Photoelectrochemical Cell with Mesoscopic Electrodes Sensitized by Lead-halide Compounds (11). *ECS Meet. Abstr.* (2008) doi:10.1149/MA2008-02/1/27.

16. Kim, H.-S. *et al.* Lead Iodide Perovskite Sensitized All-Solid-State Submicron Thin Film Mesoscopic Solar Cell with Efficiency Exceeding 9%. *Sci. Rep.* **2**, 591 (2012).

17. Lee, M. M., Teuscher, J., Miyasaka, T., Murakami, T. N. & Snaith, H. J. Efficient Hybrid Solar Cells Based on Meso-Superstructured Organometal Halide Perovskites. *Science (80-.).* **338**, 643–647 (2012).

18. Tilley, R. J. D. *Perovskites*. *Perovskites: Structure-Property Relationships* (John Wiley & Sons, Ltd, 2016). doi:10.1002/9781118935651.

19. Ramos-Terrón, S., Jodlowski, A. D., Verdugo-Escamilla, C., Camacho, L. & de Miguel, G. Relaxing the Goldschmidt Tolerance Factor: Sizable Incorporation of the Guanidinium Cation into a Two-Dimensional Ruddlesden–Popper Perovskite. *Chem.*

Mater. **32**, 4024–4037 (2020).

20. Tschauner, O. *et al.* Discovery of bridgmanite, the most abundant mineral in Earth, in a shocked meteorite. *Science (80-.).* **346**, 1100–1102 (2014).

21. Bhalla, A. S., Guo, R. & Roy, R. The perovskite structure—a review of its role in ceramic science and technology. *Mater. Res. Innov.* **4**, 3–26 (2000).

22. Jung, M., Ji, S.-G., Kim, G. & Seok, S. Il. Perovskite precursor solution chemistry: from fundamentals to photovoltaic applications. *Chem. Soc. Rev.* (2019) doi:10.1039/C8CS00656C.

23. Saliba, M. *et al.* Cesium-containing triple cation perovskite solar cells: improved stability, reproducibility and high efficiency. *Energy Environ. Sci.* **9**, 1989–1997 (2016).

24. Jacobsson, J. T. *et al.* An exploration of the compositional space for mixed lead halogen perovskites for high efficiency devices. *Energy Environ. Sci.* **41**, 1–35 (2016).

25. Levchuk, I. *et al.* Brightly Luminescent and Color-Tunable Formamidinium Lead Halide Perovskite FAPbX3 (X = Cl, Br, I) Colloidal Nanocrystals. *Nano Lett.* **17**, 2765–2770 (2017).

26. Roy, A., Ghosh, A., Bhandari, S., Sundaram, S. & Mallick, T. K. Perovskite Solar Cells for BIPV Application: A Review. *Buildings* **10**, 129 (2020).

27. Rühle, S. Tabulated values of the Shockley–Queisser limit for single junction solar cells. *Sol. Energy* **130**, 139–147 (2016).

28. Green, M. A., Ho-Baillie, A. & Snaith, H. J. The emergence of perovskite solar cells. *Nat. Photonics* **8**, 506–514 (2014).

29. deQuilettes, D. W. *et al.* Charge-Carrier Recombination in Halide Perovskites. *Chem. Rev.* **119**, 11007–11019 (2019).

30. Yin, W.-J., Shi, T. & Yan, Y. Unusual defect physics in CH 3 NH 3 PbI 3 perovskite solar cell absorber. *Appl. Phys. Lett.* **104**, 063903 (2014).

31. Giorgi, G. & Yamashita, K. Organic–inorganic halide perovskites: an ambipolar class of

materials with enhanced photovoltaic performances. *J. Mater. Chem. A* **3**, 8981–8991 (2015).

32. Giorgi, G., Fujisawa, J.-I., Segawa, H. & Yamashita, K. Small Photocarrier Effective Masses Featuring Ambipolar Transport in Methylammonium Lead Iodide Perovskite: A Density Functional Analysis. *J. Phys. Chem. Lett.* **4**, 4213–4216 (2013).

33. Staub, F. *et al.* Beyond Bulk Lifetimes: Insights into Lead Halide Perovskite Films from Time-Resolved Photoluminescence. *Phys. Rev. Appl.* **6**, 1–13 (2016).

34. Chirvony, V. S. *et al.* Short Photoluminescence Lifetimes in Vacuum-Deposited CH3NH3PbI3 Perovskite Thin Films as a Result of Fast Diffusion of Photogenerated Charge Carriers. *J. Phys. Chem. Lett.* **10**, 5167–5172 (2019).

35. Richter, J. M. *et al.* Enhancing photoluminescence yields in lead halide perovskites by photon recycling and light out-coupling. *Nat. Commun.* **7**, 13941 (2016).

36. Zhumekenov, A. A. *et al.* Formamidinium Lead Halide Perovskite Crystals with Unprecedented Long Carrier Dynamics and Diffusion Length. *ACS Energy Lett.* **1**, 32–37 (2016).

37. Zhao, Y., Nardes, A. M. & Zhu, K. Solid-State Mesostructured Perovskite CH 3 NH 3 PbI 3 Solar Cells: Charge Transport, Recombination, and Diffusion Length. *J. Phys. Chem. Lett.* **5**, 490–494 (2014).

38. Manser, J. S. & Kamat, P. V. Band filling with free charge carriers in organometal halide perovskites. *Nat. Photonics* **8**, 737–743 (2014).

39. Umari, P., Mosconi, E. & De Angelis, F. Infrared Dielectric Screening Determines the Low Exciton Binding Energy of Metal-Halide Perovskites. *J. Phys. Chem. Lett.* **9**, 620–627 (2018).

40. Liu, Y. *et al.* Investigation on binding energy and reduced effective mass of exciton in organic–inorganic hybrid lead perovskite films by a pure optical method. *Opt. Lett.* **44**, 3474 (2019).

41. Yan, K. *et al.* Hybrid Halide Perovskite Solar Cell Precursors: Colloidal Chemistry and

Coordination Engineering behind Device Processing for High Efficiency. *J. Am. Chem. Soc.* **137**, 4460–4468 (2015).

42. Hamill, J. C., Schwartz, J. & Loo, Y. L. Influence of Solvent Coordination on Hybrid Organic-Inorganic Perovskite Formation. *ACS Energy Lett.* **3**, 92–97 (2018).

43. Jo, Y. *et al.* High Performance of Planar Perovskite Solar Cells Produced from PbI 2 (DMSO) and PbI 2 (NMP) Complexes by Intramolecular Exchange. *Adv. Mater. Interfaces* **3**, 1500768 (2016).

44. Chen, H. *et al.* Forming Intermediate Phase on the Surface of PbI 2 Precursor Films by Short-Time DMSO Treatment for High-Efficiency Planar Perovskite Solar Cells via Vapor-Assisted Solution Process. *ACS Appl. Mater. Interfaces* **10**, 1781–1791 (2018).

45. Zhang, W. *et al.* Ultrasmooth organic-inorganic perovskite thin-film formation and crystallization for efficient planar heterojunction solar cells. *Nat. Commun.* **6**, (2015).

46. Hu, Y. *et al.* [Supp] Understanding the Role of Cesium and Rubidium Additives in Perovskite Solar Cells: Trap States, Charge Transport, and Recombination. *Adv. Energy Mater.* **1703057**, 1703057 (2018).

47. Zhang, M. *et al.* Suppressed phase transition of a Rb/K incorporated inorganic perovskite with a water-repelling surface. *Nanoscale* **12**, 6571–6581 (2020).

48. Konstantakou, M., Perganti, D., Falaras, P. & Stergiopoulos, T. Anti-Solvent Crystallization Strategies for Highly Efficient Perovskite Solar Cells. *Crystals* **7**, 291 (2017).

49. Wang, S., Yu, W., Zhang, L. & Yang, Y. Crystallization process of PbI2 solution in two-step deposition of CH3NH3PbI3 for high-performance perovskite solar cells. *Sol. Energy Mater. Sol. Cells* **161**, 444–448 (2017).

50. Li, X. *et al.* A vacuum flash–assisted solution process for high-efficiency large-area perovskite solar cells. *Science (80-.).* **353**, 58–62 (2016).

51. Kim, J.-E. *et al.* Slot die coated planar perovskite solar cells via blowing and heating assisted one step deposition. *Sol. Energy Mater. Sol. Cells* **179**, 80–86 (2018).

52. Sanchez, S., Hua, X., Phung, N., Steiner, U. & Abate, A. Flash Infrared Annealing for Antisolvent-Free Highly Efficient Perovskite Solar Cells. *Adv. Energy Mater.* **1702915**, 1702915 (2018).

53. Kang, D. & Park, N. On the Current–Voltage Hysteresis in Perovskite Solar Cells: Dependence on Perovskite Composition and Methods to Remove Hysteresis. *Adv. Mater.* **31**, 1805214 (2019).

54. Flora, G., Gupta, D. & Tiwari, A. Toxicity of lead: a review with recent updates. *Interdiscip. Toxicol.* **5**, 47–58 (2012).

55. Babayigit, A. *et al.* Assessing the toxicity of Pb- and Sn-based perovskite solar cells in model organism Danio rerio. *Sci. Rep.* **6**, 18721 (2016).

56. Miyasaka, T., Kulkarni, A., Kim, G. M., Öz, S. & Jena, A. K. Perovskite Solar Cells: Can We Go Organic-Free, Lead-Free, and Dopant-Free? *Adv. Energy Mater.* **10**, (2020).

57. Green, M. A. *et al.* Solar cell efficiency tables (version 54). *Prog. Photovoltaics Res. Appl.* **27**, 3–12 (2019).

58. Roose, B., Wang, Q. & Abate, A. The Role of Charge Selective Contacts in Perovskite Solar Cell Stability. *Adv. Energy Mater.* **9**, 1803140 (2018).

59. Unger, E. L., Shargaieva, O., Braunger, S. & Docampo, P. CHAPTER 4. Solution-processed Solar Cells: Perovskite Solar Cells. in 153–192 (2019). doi:10.1039/9781788013512-00153.

60. Galagan, Y., Coenen, E. W. C., Verhees, W. & Andriessen, R. Towards scaling up of perovskite solar cells and modules. *J. Mater. Chem. A* **4**, 5700–5705 (2016).

61. Zhao, Y. *et al.* Research progress in large-area perovskite solar cells. *Photonics Res.* **8**, A1 (2020).

62. Hermerschmidt, F. *et al.* Finally, inkjet-printed metal halide perovskite LEDs – utilizing seed crystal templating of salty PEDOT:PSS. *Mater. Horizons* **7**, 1773–1781 (2020).

63. Senanayak, S. P. *et al.* A general approach for hysteresis-free, operationally stable metal

halide perovskite field-effect transistors. *Sci. Adv.* **6**, eaaz4948 (2020).

64. Dong, H., Zhang, C., Liu, X., Yao, J. & Zhao, Y. S. Materials chemistry and engineering in metal halide perovskite lasers. *Chem. Soc. Rev.* **49**, 951–982 (2020).

65. Hsiao, Y.-W., Wang, S.-Y., Huang, C.-L., Leu, C.-C. & Shih, C.-F. Resistive Switching Property of Organic–Inorganic Tri-Cation Lead Iodide Perovskite Memory Device. *Nanomaterials* **10**, 1155 (2020).

66. Zhao, Z. *et al.* Preparation and testing of anisotropic MAPbI3 perovskite photoelectric sensors. *ACS Appl. Mater. Interfaces* acsami.0c10062 (2020) doi:10.1021/acsami.0c10062.

67. Dai, G. *et al.* Perovskite Quantum Dots Based Optical Fabry–Pérot Pressure Sensor. *ACS Photonics* acsphotonics.0c01109 (2020) doi:10.1021/acsphotonics.0c01109.

68. Cho, M. *et al.* Perovskite-Induced Ultrasensitive and Highly Stable Humidity Sensor Systems Prepared by Aerosol Deposition at Room Temperature. *Adv. Funct. Mater.* **30**, 1907449 (2020).

69. Lang, F. *et al.* Proton Radiation Hardness of Perovskite Tandem Photovoltaics. *Joule* **4**, 1054–1069 (2020).

70. Holzhey, P. *et al.* A chain is as strong as its weakest link – Stability study of MAPbI3 under light and temperature. *Mater. Today* **29**, 10–19 (2019).

71. Fahrenbruch, A. L., Bube, R. H. & D'Aiello, R. V. Fundamentals of Solar Cells (Photovoltaic Solar Energy Conversion). *J. Sol. Energy Eng.* **106**, 497–498 (1984).

72. Colinge, J. P. & Colinge, C. A. *Physics of Semiconductor Devices*. (Kluwer Academic Publishers, 2002). doi:10.1007/b117561.

73. *Silicon Materials Science and Technology: Proceedings of the Eighth International Symposium on Silicon Materials Science and Technology, Volume 1*. (The Electrochemical Society, 1998).

74. Würfel, P. & Würfel, U. *Physics of Solar Cells*. *Physics of Solar Cells* (Wiley-VCH

Verlag GmbH, 2005). doi:10.1002/9783527618545.

75. Chopra, K. L., Paulson, P. D. & Dutta, V. Thin-film solar cells: an overview. *Prog. Photovoltaics Res. Appl.* **12**, 69–92 (2004).

76. Yoshihiro Hamakawa. *Thin-Film Solar Cells Next Generation Photovoltaics and Its Applications*. *Igarss 2014* (2003).

77. Poortmans, J. & Arkhipov, V. *Thin Film Solar Cells*. *Thin Film Solar Cells Fabrication, Characterization and Applications* (John Wiley & Sons, Ltd, 2006). doi:10.1002/0470091282.

78. Green, M. a. *Third generation photovoltaics: advanced solar energy conversion*. *Energy Conversion* vol. 10 (2006).

79. Thangadurai, P., Joicy, S., Beura, R., Santhosh Kumar, J. & Chitrarasu, K. Emerging Nanomaterials in Energy and Environmental Science: An Overview. in 1–49 (2019). doi:10.1007/978-3-030-04474-9_1.

80. Conibeer, G. Third-generation photovoltaics. *Mater. Today* **10**, 42–50 (2007).

81. *Third Generation Photovoltaics*. (InTech, 2012). doi:10.5772/1386.

82. Nelson, J. *The Physics of Solar Cells*. *The Physics of Solar Cells* (PUBLISHED BY IMPERIAL COLLEGE PRESS AND DISTRIBUTED BY WORLD SCIENTIFIC PUBLISHING CO., 2003). doi:10.1142/p276.

83. Sze, S. M. *Semiconductor Devices: Physics and Technology*. *Technology* (2006). doi:10.1016/S0026-2692(82)80036-0.

84. Sze, S. M. & Ng, K. K. *Physics of Semiconductor Devices*. vol. 1 (John Wiley & Sons, Inc., 2006).

85. Yeboah, D. & Singh, J. Dependence of Exciton Diffusion Length and Diffusion Coefficient on Photophysical Parameters in Bulk Heterojunction Organic Solar Cells. *J. Electron. Mater.* **46**, 6451–6460 (2017).

86. Chen, Y. & Ma, D. Organic semiconductor heterojunctions as charge generation layers

and their application in tandem organic light-emitting diodes for high power efficiency. *J. Mater. Chem.* **22**, 18718 (2012).

87. Benghanem, M. & Almohammedi, A. Organic Solar Cells: A Review. in *Applied Energy* 81–106 (2020). doi:10.1007/978-3-030-43473-1_5.

88. Shi, D. *et al.* Low trap-state density and long carrier diffusion in organolead trihalide perovskite single crystals. *Science (80-.).* **347**, 519–522 (2015).

89. Sun, X. *et al.* Influence of the Porosity of the TiO 2 Film on the Performance of the Perovskite Solar Cell. *Int. J. Photoenergy* **2017**, 1–10 (2017).

90. Gray, J. L. The Physics of the Solar Cell. in *Handbook of Photovoltaic Science and Engineering* 61–112 (John Wiley & Sons, Ltd, 2005). doi:10.1002/0470014008.ch3.

91. Köhler, A. & Bässler, H. *Electronic Processes in Organic Semiconductors*. *Electronic Processes in Organic Semiconductors: An Introduction* (Wiley-VCH Verlag GmbH & Co. KGaA, 2015). doi:10.1002/9783527685172.

92. Lakhwani, G., Rao, A. & Friend, R. H. Bimolecular Recombination in Organic Photovoltaics. *Annu. Rev. Phys. Chem.* **65**, 557–581 (2014).

93. Valeur, B. & Berberan-Santos, M. N. *Molecular Fluorescence*. *John Wiley & Sons* (Wiley-VCH Verlag GmbH & Co. KGaA, 2012). doi:10.1002/9783527650002.

94. Lakowicz, J. R. *Principles of Fluorescence Spectroscopy*. *Principles of Fluorescence Spectroscopy* (Springer US, 2006). doi:10.1007/978-0-387-46312-4.

95. Becker, W. *Advanced Time-Correlated Single Photon Counting Applications*. vol. 111 (Springer International Publishing, 2015).

96. Kautsky, H. Quenching of luminescence by oxygen. *Trans. Faraday Soc.* **35**, 216 (1939).

97. You, Z. Q. & Hsu, C. P. Theory and calculation for the electronic coupling in excitation energy transfer. *Int. J. Quantum Chem.* **114**, 102–115 (2014).

98. Nacht, B. *et al.* Integrated catheter system for continuous glucose measurement and simultaneous insulin infusion. *Biosens. Bioelectron.* **64**, 102–110 (2014).

99. Zhang, H., Tao, F., Cui, Y. & Wu, H. Super-quenching: Multiple migration channels of excitons cause “area quenching”. *Mater. Chem. Phys.* **243**, 122657 (2020).

100. Li, H. & Han, C. Sonochemical synthesis of cyclodextrin-coated quantum dots for optical detection of pollutant phenols in water. *Chem. Mater.* **20**, 6053–6059 (2008).

101. Smith, C. S. & Mann, K. R. Void space containing crystalline Cu(I) phenanthroline complexes as molecular oxygen sensors. *Chem. Mater.* **21**, 5042–5049 (2009).

102. Stern, O. & Volmer, M. über Die Abklingzeit der Fluoreszenz. *Zeitschrift für Phys.* **20**, 183–188 (1919).

103. Popov, A. V., Gladkikh, V. S. & Burshtein, A. I. Stern-Volmer law in competing theories and approximations. *J. Phys. Chem. A* **107**, 8177–8183 (2003).

104. Ou, J. Z. *et al.* Physisorption-Based Charge Transfer in Two-Dimensional SnS2 for Selective and Reversible NO2 Gas Sensing. *ACS Nano* **9**, 10313–10323 (2015).

105. Chen, J. K., Yang, S. M., Li, B. H., Lin, C. H. & Lee, S. Fluorescence Quenching Investigation of Methyl Red Adsorption on Aluminum-Based Metal-Organic Frameworks. *Langmuir* **34**, 1441–1446 (2018).

106. Wu, W. *et al.* Tuning the emissive triplet excited states of platinum(ii) Schiff base complexes with pyrene, and application for luminescent oxygen sensing and triplet-triplet-annihilation based upconversions. *Dalt. Trans.* **40**, 11550–11561 (2011).

107. Kuramoto, N. The role of excited singlet molecular oxygen in the photodegradation of functional squarylium dyes. *J. Soc. Dye. Colour.* **106**, 181–186 (1990).

108. Hintz, H. *et al.* Photodegradation of P3HT−A Systematic Study of Environmental Factors. *Chem. Mater.* **23**, 145–154 (2011).

109. Geddes, C. D. Optical halide sensing using fluorescence quenching: theory, simulations and applications - a review. *Meas. Sci. Technol.* **12**, R53–R88 (2001).

110. Demas, J. N., DeGraff, B. A. & Xu, W. Modeling of Luminescence Quenching-Based Sensors: Comparison of Multisite and Nonlinear Gas Solubility Models. *Anal. Chem.* **67**,

1377–1380 (1995).

111. Sacksteder, L., Demas, J. N. & DeGraff, B. A. Design of oxygen sensors based on quenching of luminescent metal complexes: Effect of ligand size on heterogeneity. *Anal. Chem.* **65**, 3480–3483 (1993).

112. Carraway, E. R., Demas, J. N., DeGraff, B. A. & Bacon, J. R. Photophysics and Photochemistry of Oxygen Sensors Based on Luminescent Transition-Metal Complexes. *Anal. Chem.* **63**, 337–342 (1991).

113. Kipphan, H. *Hand Book of Print Media*. *Handbook of Print Media* (2001).

114. *Fundamentals of Inkjet Printing*. *Fundamentals of Inkjet Printing* (Wiley-VCH Verlag GmbH & Co. KGaA, 2016). doi:10.1002/9783527684724.

115. Peng, X. *et al.* Perovskite and Organic Solar Cells Fabricated by Inkjet Printing: Progress and Prospects. *Adv. Funct. Mater.* **1703704**, (2017).

116. Plateau, J. Experimental and Theoretical Statics of Liquids subject to Molecular Forces only. *Gauthier-Villars Paris* (1873) doi:10.1136/adc.2003.044073.

117. Rayleigh, Lord. On the instability of jets. *Proc. London Math. Soc.* (1878) doi:10.1112/plms/s1-10.1.4.

118. Rune, E. Measuring instrument of the recording type. (1951).

119. Bao, Z., Feng, Y., Dodabalapur, A., Raju, V. R. & Lovinger, A. J. High-Performance Plastic Transistors Fabricated by Printing Techniques. *Chem. Mater.* **9**, 1299–1301 (1997).

120. Hoth, C. N., Schilinsky, P., Choulis, S. A. & Brabec, C. J. Printing Highly Efficient Organic Solar Cells. *Nano Lett.* **8**, 2806–2813 (2008).

121. Cui, Z. *Printed Electronics*. *MRS Bulletin* vol. 42 (John Wiley & Sons Singapore Pte. Ltd, 2016).

122. Mathies, F., List-Kratochvil, E. J. W. & Unger, E. L. Advances in Inkjet-Printed Metal Halide Perovskite Photovoltaic and Optoelectronic Devices. *Energy Technol.* **8**, 1900991

(2020).

123. Klug, A. *et al.* Recent progress in printed 2/3D electronic devices. in *Smart Systems Integration - 8th International Conference and Exhibition on Integration Issues of Miniaturized Systems - MEMS, NEMS, ICs and Electronic Components, SSI 2014* (ed. List Kratochvil, E. J. W.) vol. 9569 95690N (2015).

124. Tsai, M. H. & Hwang, W. S. Effects of pulse voltage on the droplet formation of alcohol and ethylene glycol in a piezoelectric inkjet printing process with bipolar pulse. *Mater. Trans.* **49**, 331–338 (2008).

125. Liu, Y. F., Pai, Y. F., Tsai, M. H. & Hwang, W. S. Investigation of driving waveform and resonance pressure in piezoelectric inkjet printing. *Appl. Phys. A Mater. Sci. Process.* **109**, 323–329 (2012).

126. Zapka, W. *Handbook of Industrial Inkjet Printing: A Full System Approach*. *Handbook of Industrial Inkjet Printing: A Full System Approach* (2017). doi:10.1002/9783527687169.

127. Derby, B. Inkjet Printing of Functional and Structural Materials: Fluid Property Requirements, Feature Stability, and Resolution. *Annu. Rev. Mater. Res.* **40**, 395–414 (2010).

128. Jang, D., Kim, D. & Moon, J. Influence of Fluid Physical Properties on Ink-Jet Printability. *Langmuir* **25**, 2629–2635 (2009).

129. Ganjei, J., Sawoska, D. & Krol, A. Digital inkjet printing for etching circuits. in *2007 International Microsystems, Packaging, Assembly and Circuits Technology* 359–362 (IEEE, 2007). doi:10.1109/IMPACT.2007.4433636.

130. Ralston, J. Solid-Liquid Interactions and Functional Surface Wettability. *Aust. J. Chem.* **58**, 644 (2005).

131. Law, K. Y. & Zhao, H. *Surface wetting: Characterization, contact angle, and fundamentals*. *Surface Wetting: Characterization, Contact Angle, and Fundamentals* (2015). doi:10.1007/978-3-319-25214-8.

132. Twardowski, T. E. *Introduction to Nanocomposite Materials: Properties, Processing, Characterization*. (DEStech Publications, Inc, 2007).

133. Soltman, D. & Subramanian, V. Inkjet-printed line morphologies and temperature control of the coffee ring effect. *Langmuir* **24**, 2224–2231 (2008).

134. Polzinger, B. *et al.* UV-sintering of inkjet-printed conductive silver tracks. in *2011 11th IEEE International Conference on Nanotechnology* 201–204 (IEEE, 2011). doi:10.1109/NANO.2011.6144541.

135. Mitra, K. Y., Weise, D., Hartwig, M. & Baumann, R. R. Infra-red curing methodology for Roll-to-Roll (R2R) manufacturing of conductive electrodes through inkjet technology applicable for devices in the field of flexible electronics. *MRS Proc.* **1791**, 1–6 (2015).

136. Perelaer, J., Klokkenburg, M., Hendriks, C. E. & Schubert, U. S. Microwave flash sintering of inkjet-printed silver tracks on polymer substrates. *Adv. Mater.* **21**, 4830–4834 (2009).

137. Park, J. *et al.* Highly Customizable All Solution–Processed Polymer Light Emitting Diodes with Inkjet Printed Ag and Transfer Printed Conductive Polymer Electrodes. *Adv. Funct. Mater.* **29**, 1902412 (2019).

138. Angmo, D., Larsen-Olsen, T. T., Jørgensen, M., Søndergaard, R. R. & Krebs, F. C. Roll-to-roll inkjet printing and photonic sintering of electrodes for ITO free polymer solar cell modules and facile product integration. *Adv. Energy Mater.* **3**, 172–175 (2013).

139. Nandayapa, E. R., Hirselandt, K., Boeffel, C., Unger, E. L. & List-Kratochvil, E. J. W. Unraveling Reversible Quenching Processes of O 2 , N 2 , Ar, and H 2 O in Metal Halide Perovskites at Moderate Photon Flux Densities. *Adv. Opt. Mater.* **2001317**, 2001317 (2020).

140. Rankin, D. W. H. CRC handbook of chemistry and physics, 89th edition, edited by David R. Lide. *Crystallogr. Rev.* **15**, 223–224 (2009).

141. Grancini, G. *et al.* CH 3 NH 3 PbI 3 perovskite single crystals: surface photophysics and their interaction with the environment. *Chem. Sci.* **6**, 7305–7310 (2015).

142. Hoye, R. L. Z. *et al.* Perovskite-Inspired Photovoltaic Materials: Toward Best Practices in Materials Characterization and Calculations. *Chem. Mater.* **29**, 1964–1988 (2017).

143. Tian, Y. *et al.* Mechanistic insights into perovskite photoluminescence enhancement: light curing with oxygen can boost yield thousandfold. *Phys. Chem. Chem. Phys.* **17**, 24978–24987 (2015).

144. Brenes, R., Eames, C., Bulović, V., Islam, M. S. & Stranks, S. D. The Impact of Atmosphere on the Local Luminescence Properties of Metal Halide Perovskite Grains. *Adv. Mater.* **30**, 1706208 (2018).

145. Galisteo-López, J. F., Anaya, M., Calvo, M. E. & Míguez, H. Environmental Effects on the Photophysics of Organic–Inorganic Halide Perovskites. *J. Phys. Chem. Lett.* **6**, 2200–2205 (2015).

146. Fang, H. H., Wang, F., Adjokatse, S., Zhao, N. & Loi, M. A. Photoluminescence Enhancement in Formamidinium Lead Iodide Thin Films. *Adv. Funct. Mater.* **26**, 4653–4659 (2016).

147. Motti, S. G. *et al.* Photoinduced Emissive Trap States in Lead Halide Perovskite Semiconductors. *ACS Energy Lett.* **1**, 726–730 (2016).

148. Huang, Y., Zhao, L., Li, J., Lu, F. & Wang, S. Effects of methylamine doping on the stability of triple cation (FA 0.95−x MA x Cs 0.05)PbI 3 single crystal perovskites. *Nanoscale Adv.* **2**, 332–339 (2020).

149. Ding, J. *et al.* Design Growth of MAPbI3 Single Crystal with (220) Facets Exposed and Its Superior Optoelectronic Properties. *J. Phys. Chem. Lett.* **9**, 216–221 (2018).

150. Aristidou, N. *et al.* Fast oxygen diffusion and iodide defects mediate oxygen-induced degradation of perovskite solar cells. *Nat. Commun.* **8**, 1–10 (2017).

151. Kasha, M. & Khan, A. U. THE PHYSICS, CHEMISTRY, AND BIOLOGY, OF SINGLET MOLECULAR OXYGEN. *Ann. N. Y. Acad. Sci.* **171**, 5–23 (1970).

152. Azpiroz, J. M., Mosconi, E., Bisquert, J. & De Angelis, F. Defect migration in methylammonium lead iodide and its role in perovskite solar cell operation. *Energy*

Environ. Sci. **8**, 2118–2127 (2015).

153. Stranks, S. D. *et al.* Recombination Kinetics in Organic-Inorganic Perovskites: Excitons, Free Charge, and Subgap States. *Phys. Rev. Appl.* **2**, 1–8 (2014).

154. Koocher, N. Z., Saldana-Greco, D., Wang, F., Liu, S. & Rappe, A. M. Polarization Dependence of Water Adsorption to CH3NH3PbI3 (001) Surfaces. *J. Phys. Chem. Lett.* **6**, 4371–4378 (2015).

155. Jin, H. *et al.* It's a trap! On the nature of localised states and charge trapping in lead halide perovskites. *Mater. Horizons* (2020) doi:10.1039/C9MH00500E.

156. Levine, I. *et al.* Deep Defect States in Wide-Band-Gap ABX 3 Halide Perovskites. *ACS Energy Lett.* **4**, 1150–1157 (2019).

157. Dodge, Y. *The Concise Encyclopedia of Statistics*. *The Concise Encyclopedia of Statistics* (Springer New York, 2008). doi:10.1007/978-0-387-32833-1.

158. Lakowicz, J. R. & Weber, G. Quenching of Fluorescence by Oxygen. a Probe for Structural Fluctuations in Macromolecules. *Biochemistry* **12**, 4161–4170 (1973).

159. Chen, T. *et al.* Entropy-driven structural transition and kinetic trapping in formamidinium lead iodide perovskite. *Sci. Adv.* **2**, 1–6 (2016).

160. Milot, R. L., Eperon, G. E., Snaith, H. J., Johnston, M. B. & Herz, L. M. Temperature-Dependent Charge-Carrier Dynamics in CH3NH3PbI3 Perovskite Thin Films. *Adv. Funct. Mater.* **25**, 6218–6227 (2015).

161. Adhyaksa, G. W. P. *et al.* Understanding Detrimental and Beneficial Grain Boundary Effects in Halide Perovskites. *Adv. Mater.* **30**, 1804792 (2018).

162. Yun, J. S. *et al.* Benefit of grain boundaries in organic-inorganic halide planar perovskite solar cells. *J. Phys. Chem. Lett.* **6**, 875–880 (2015).

163. Abdi-Jalebi, M. *et al.* Potassium- and Rubidium-Passivated Alloyed Perovskite Films: Optoelectronic Properties and Moisture Stability. *ACS Energy Lett.* acsenergylett.8b01504 (2018) doi:10.1021/acsenergylett.8b01504.

164. Abdi-Jalebi, M. *et al.* Maximizing and stabilizing luminescence from halide perovskites with potassium passivation. *Nat. Publ. Gr.* **555**, 497–501 (2018).

165. Turren Cruz, S. H. *et al.* Enhanced charge carrier mobility and lifetime suppress hysteresis and improve efficiency in planar perovskite solar cells. *Energy Environ. Sci.* (2017) doi:10.1039/c7ee02901b.

166. Philippe, B. *et al.* Chemical Distribution of Multiple Cation (Rb + , Cs + , MA + , and FA +) Perovskite Materials by Photoelectron Spectroscopy. *Chem. Mater.* **29**, 3589–3596 (2017).

167. Zong, Y. *et al.* Continuous Grain-Boundary Functionalization for High-Efficiency Perovskite Solar Cells with Exceptional Stability. *Chem* **4**, 1404–1415 (2018).

168. Chen, B., Rudd, P. N., Yang, S., Yuan, Y. & Huang, J. Imperfections and their passivation in halide perovskite solar cells. *Chem. Soc. Rev.* (2019) doi:10.1039/C8CS00853A.

169. Li, Y. *et al.* Direct Observation of Long Electron-Hole Diffusion Distance in CH3NH3PbI3 Perovskite Thin Film. *Sci. Rep.* **5**, 14485 (2015).

170. Jiang, Q. *et al.* Surface passivation of perovskite film for efficient solar cells. *Nat. Photonics* **13**, 460–466 (2019).

171. Kegelmann, L. *et al.* Mixtures of Dopant-Free Spiro-OMeTAD and Water-Free PEDOT as a Passivating Hole Contact in Perovskite Solar Cells. *ACS Appl. Mater. Interfaces* **11**, 9172–9181 (2019).

172. Zu, F. *et al.* Unraveling the Electronic Properties of Lead Halide Perovskites with Surface Photovoltage in Photoemission Studies. *ACS Appl. Mater. Interfaces* **11**, 21578–21583 (2019).

173. Senocrate, A. *et al.* Interaction of oxygen with halide perovskites. *J. Mater. Chem. A* **6**, 10847–10855 (2018).

174. Aristidou, N. *et al.* The Role of Oxygen in the Degradation of Methylammonium Lead Trihalide Perovskite Photoactive Layers. *Angew. Chemie Int. Ed.* **54**, 8208–8212 (2015).

175. Bryant, D. *et al.* Light and oxygen induced degradation limits the operational stability of methylammonium lead triiodide perovskite solar cells. *Energy Environ. Sci.* **9**, 1655–1660 (2016).

176. Lin, C.-T. *et al.* Evidence for surface defect passivation as the origin of the remarkable photostability of unencapsulated perovskite solar cells employing aminovaleric acid as a processing additive. *J. Mater. Chem. A* **7**, 3006–3011 (2019).

177. Anaya, M., Galisteo-López, J. F., Calvo, M. E., Espinós, J. P. & Míguez, H. Origin of Light-Induced Photophysical Effects in Organic Metal Halide Perovskites in the Presence of Oxygen. *J. Phys. Chem. Lett.* **9**, 3891–3896 (2018).

178. Wang, Z. *et al.* High irradiance performance of metal halide perovskites for concentrator photovoltaics. *Nat. Energy* **3**, 855–861 (2018).

179. Law, C. *et al.* Performance and stability of lead perovskite/TiO2, polymer/PCBM, and dye sensitized solar cells at light intensities up to 70 suns. *Adv. Mater.* **26**, 6268–6273 (2014).

180. Dar, M. I. *et al.* Origin of unusual bandgap shift and dual emission in organic-inorganic lead halide perovskites. *Sci. Adv.* **2**, e1601156 (2016).

181. Ayers, M. R. & Hunt, A. J. Molecular oxygen sensors based on photoluminescent silica aerogels. *J. Non. Cryst. Solids* **225**, 343–347 (1998).

182. Baranowski, M. & Plochocka, P. Excitons in Metal-Halide Perovskites. *Adv. Energy Mater.* **1903659**, (2020).

183. D'Innocenzo, V. *et al.* Excitons versus free charges in organo-lead tri-halide perovskites. *Nat. Commun.* **5**, 3586 (2014).

184. Ralaiarisoa, M., Salzmann, I., Zu, F. S. & Koch, N. Effect of Water, Oxygen, and Air Exposure on CH3NH3PbI3–xClx Perovskite Surface Electronic Properties. *Adv. Electron. Mater.* **4**, 1–8 (2018).

185. Zoski, C. G. *Handbook of Electrochemistry*. *Handbook of Electrochemistry* (Elsevier, 2007). doi:10.1016/B978-0-444-51958-0.X5000-9.

186. Gong, X. *et al.* Controllable Perovskite Crystallization by Water Additive for High-Performance Solar Cells. *Adv. Funct. Mater.* **25**, 6671–6678 (2015).

187. Zhang, J., Zhou, P., Liu, J. & Yu, J. New understanding of the difference of photocatalytic activity among anatase, rutile and brookite TiO2. *Phys. Chem. Chem. Phys.* **16**, 20382–20386 (2014).

188. Ling, L. *et al.* Precisely Controlled Hydration Water for Performance Improvement of Organic–Inorganic Perovskite Solar Cells. *Adv. Funct. Mater.* **26**, 5028–5034 (2016).

189. Frost, J. M. *et al.* Atomistic Origins of High-Performance in Hybrid Halide Perovskite Solar Cells. *Nano Lett.* **14**, 2584–2590 (2014).

190. Mosconi, E., Azpiroz, J. M. & De Angelis, F. Ab Initio Molecular Dynamics Simulations of Methylammonium Lead Iodide Perovskite Degradation by Water. *Chem. Mater.* **27**, 4885–4892 (2015).

191. Joo, J. H., Merkle, R. & Maier, J. Effects of water on oxygen surface exchange and degradation of mixed conducting perovskites. *J. Power Sources* **196**, 7495–7499 (2011).

192. Yang, J. *et al.* Oxygen- and Water-Induced Energetics Degradation in Organometal Halide Perovskites. *ACS Appl. Mater. Interfaces* **10**, 16225–16230 (2018).

193. Kisch, H. *Semiconductor Photocatalysis*. *Semiconductor Photocatalysis: Principles and Applications* (Wiley-VCH Verlag GmbH & Co. KGaA, 2014). doi:10.1002/9783527673315.

194. Frink, M. E., Magde, D., Sexton, D. & Ford, P. C. Reaction dynamics and hydroxide ion quenching of rhodium(III) ligand field excited states: photoreactions of iodopentaamminerhodium(2+). *Inorg. Chem.* **23**, 1238–1240 (1984).

195. Cuquerella, M. C., Boscá, F. & Miranda, M. A. Photonucleophilic aromatic substitution of 6-fluoroquinolones in basic media: Triplet quenching by hydroxide anion. *J. Org. Chem.* **69**, 7256–7261 (2004).

196. Simoncelli, S., Kuzmanich, G., Gard, M. N. & Garcia-Garibay, M. A. Photochemical reaction mechanisms and kinetics with molecular nanocrystals: surface quenching of

triplet benzophenone nanocrystals. *J. Phys. Org. Chem.* **23**, 376–381 (2010).

197. Martin, M. M. & Hynes, J. T. *Femtochemistry and Femtobiology*. *Femtochemistry and Femtobiology: Ultrafast Events in Molecular Science* (Elsevier, 2004). doi:10.1016/B978-0-444-51656-5.X5000-2.

198. Manz, J. & Wöste, L. *Femtosecond Chemistry*. *Journal of the American Chemical Society* vol. 118 (Wiley, 1994).

199. Amirav, A., Even, U. & Jortner, J. Spectroscopy of large molecules in inert gas clusters. *Chem. Phys. Lett.* **72**, 16–20 (1980).

200. Sambursky, S. & Wolfsohn, G. Quenching of Fluorescence by Van Der Waals Forces. *Nature* **157**, 228–229 (1946).

201. Zhyrovetsky, V. M., Popovych, D. I., Savka, S. S. & Serednytski, A. S. Nanopowder Metal Oxide for Photoluminescent Gas Sensing. *Nanoscale Res. Lett.* **12**, 132 (2017).

202. Sahu, N., Parija, B. & Panigrahi, S. Fundamental understanding and modeling of spin coating process: A review. *Indian J. Phys.* **83**, 493–502 (2009).

203. Deng, Y. *et al.* Surfactant-controlled ink drying enables high-speed deposition of perovskite films for efficient photovoltaic modules. *Nat. Energy* **3**, 560–566 (2018).

204. Park, M. *et al.* Highly Reproducible Large-Area Perovskite Solar Cell Fabrication via Continuous Megasonic Spray Coating of CH3NH3PbI3. *Small* **15**, 1–7 (2019).

205. Mathies, F. *et al.* Inkjet-Printed Triple Cation Perovskite Solar Cells. *ACS Appl. Energy Mater.* acsaem.8b00222 (2018) doi:10.1021/acsaem.8b00222.

206. Borchert, J. *et al.* Large-Area, Highly Uniform Evaporated Formamidinium Lead Triiodide Thin Films for Solar Cells. *ACS Energy Lett.* **2**, 2799–2804 (2017).

207. Di Giacomo, F. *et al.* Up-scalable sheet-to-sheet production of high efficiency perovskite module and solar cells on 6-in. substrate using slot die coating. *Sol. Energy Mater. Sol. Cells* **181**, 53–59 (2018).

208. Abzieher, T. *et al.* Electron-Beam-Evaporated Nickel Oxide Hole Transport Layers for

Perovskite-Based Photovoltaics. *Adv. Energy Mater.* **9**, 1–13 (2019).

209. Park, N. G. & Zhu, K. Scalable fabrication and coating methods for perovskite solar cells and solar modules. *Nat. Rev. Mater.* (2020) doi:10.1038/s41578-019-0176-2.

210. Krebs, F. C. Fabrication and processing of polymer solar cells: A review of printing and coating techniques. *Sol. Energy Mater. Sol. Cells* **93**, 394–412 (2009).

211. Li, P. *et al.* Inkjet manipulated homogeneous large size perovskite grains for efficient and large-area perovskite solar cells. *Nano Energy* **46**, 203–211 (2018).

212. Huang, F. *et al.* Fast fabricated high performance antisolvent-free perovskite solar cells via dual-flash process. *Electrochim. Acta* **259**, 402–409 (2018).

213. Giuri, A. *et al.* Rheological Tunability of Perovskite Precursor Solutions: From Spin Coating to Inkjet Printing Process. *Nanomaterials* **9**, 582 (2019).

214. Hashmi, S. G. *et al.* [Supp]Air Processed Inkjet Infiltrated Carbon Based Printed Perovskite Solar Cells with High Stability and Reproducibility. *Adv. Mater. Technol.* **4**, 1600183 (2016).

215. Bercegol, A. *et al.* Spatial Inhomogeneity Analysis of Cesium-rich Wrinkles in Triple Cation Perovskite. (2018) doi:10.1021/acs.jpcc.8b07436.

216. Braunger, S. *et al.* Cs x FA1- xPb(I1- yBr y)3 Perovskite Compositions: The Appearance of Wrinkled Morphology and its Impact on Solar Cell Performance. *J. Phys. Chem. C* **122**, 17123–17135 (2018).

217. Saliba, M. *et al.* How to Make over 20% Efficient Perovskite Solar Cells in Regular (n–i–p) and Inverted (p–i–n) Architectures. *Chem. Mater.* **30**, 4193–4201 (2018).

218. Stolterfoht, M. *et al.* Visualization and suppression of interfacial recombination for high-efficiency large-area pin perovskite solar cells. *Nat. Energy* **3**, 847–854 (2018).

219. Al-Ashouri, A. *et al.* Conformal monolayer contacts with lossless interfaces for perovskite single junction and monolithic tandem solar cells. *Energy Environ. Sci.* **12**, 3356–3369 (2019).

220. Burschka, J. *et al.* Sequential deposition as a route to high-performance perovskite-sensitized solar cells. *Nature* **499**, 316–319 (2013).

221. Ummadisingu, A. & Grätzel, M. Revealing the detailed path of sequential deposition for metal halide perovskite formation. *Sci. Adv.* **4**, e1701402 (2018).

222. Lian, X. *et al.* Highly Efficient Sn/Pb Binary Perovskite Solar Cell via Precursor Engineering: A Two-Step Fabrication Process. *Adv. Funct. Mater.* **1807024**, 1807024 (2018).

223. Trifiletti, V., Cannavale, A., Listorti, A., Rizzo, A. & Colella, S. Sequential deposition of hybrid halide perovskite starting both from lead iodide and lead chloride on the most widely employed substrates. *Thin Solid Films* #pagerange# (2018) doi:10.1016/j.tsf.2018.05.022.

224. Razza, S. *et al.* Perovskite solar cells and large area modules (100 cm2) based on an air flow-assisted PbI2 blade coating deposition process. *J. Power Sources* **277**, 286–291 (2015).

225. Geoghegan, M. & Hadziioannou, G. *Polymer Electronics*. *Polymer Electronics* (2013). doi:10.1093/acprof:oso/9780199533824.001.0001.

226. Li, X. *et al.* A vacuum flash-assisted solution process for high-efficiency large-area perovskite solar cells. *Science (80-.).* **353**, 58–62 (2016).

227. Bu, T. *et al.* Synergic Interface Optimization with Green Solvent Engineering in Mixed Perovskite Solar Cells. *Adv. Energy Mater.* **1700576**, 1700576 (2017).

228. Gardner, K. L. *et al.* Nonhazardous Solvent Systems for Processing Perovskite Photovoltaics. *Adv. Energy Mater.* **6**, 1–8 (2016).

229. Mathies, F. *et al.* Multipass inkjet printed planar methylammonium lead iodide perovskite solar cells. *J. Mater. Chem. A* **4**, 19207–19213 (2016).

230. Qiu, W. *et al.* Pinhole-free perovskite films for efficient solar modules. *Energy Environ. Sci.* **9**, 484–489 (2016).

231. Zhang, H. *et al.* Pinhole-free and surface-nanostructured niox film by room-Temperature solution process for high-performance flexible perovskite solar cells with good stability and reproducibility. *ACS Nano* **10**, 1503–1511 (2016).

232. Masood, M. T. *et al.* Investigation of well-defined pinholes in TiO2 electron selective layers used in planar heterojunction perovskite solar cells. *Nanomaterials* **10**, 1–16 (2020).

233. Ge, Q.-Q. *et al.* Promoting Crystalline Grain Growth and Healing Pinholes by Water Vapor Modulated Post-annealing for Enhancing the Efficiency of Planar Perovskite Solar Cells. *J. Mater. Chem. A* (2016) doi:10.1039/C6TA05288F.

234. Rueden, C. T. *et al.* ImageJ2: ImageJ for the next generation of scientific image data. *BMC Bioinformatics* **18**, 529 (2017).

235. Fu, W. *et al.* Controlled crystallization of CH3NH3PbI3 films for perovskite solar cells by various PbI2(X) complexes. *Sol. Energy Mater. Sol. Cells* **155**, 331–340 (2016).

236. Heo, J. H., Han, H. J., Kim, D., Ahn, T. K. & Im, S. H. Hysteresis-less inverted CH 3 NH 3 PbI 3 planar perovskite hybrid solar cells with 18.1% power conversion efficiency. *Energy Environ. Sci.* **8**, 1602–1608 (2015).

237. Park, I. J. *et al.* Highly efficient and uniform 1 cm^2 perovskite solar cells with an electrochemically deposited NiOx hole-extraction layer. *ChemSusChem* (2017) doi:10.1002/cssc.201700612.

238. Stolterfoht, M. *et al.* Approaching the fill factor Shockley–Queisser limit in stable, dopant-free triple cation perovskite solar cells. *Energy Environ. Sci.* **7**, 1829–1849 (2017).

239. Al-Ashouri, A. *et al.* Conformal monolayer contacts with lossless interfaces for perovskite single junction and monolithic tandem solar cells. *Energy Environ. Sci.* **12**, 3356–3369 (2019).

240. Asplund, M. *et al.* Toxicity evaluation of PEDOT/biomolecular composites intended for neural communication electrodes. *Biomed. Mater.* **4**, (2009).

241. Eom, S. H. *et al.* Polymer solar cells based on inkjet-printed PEDOT:PSS layer. *Org. Electron.* **10**, 536–542 (2009).

242. Wang, Q., Chueh, C.-C., Eslamian, M. & Jen, A. K.-Y. Modulation of PEDOT:PSS pH for Efficient Inverted Perovskite Solar Cells with Reduced Potential Loss and Enhanced Stability. *ACS Appl. Mater. Interfaces* acsami.6b11757 (2016) doi:10.1021/acsami.6b11757.

243. Zhanshayeva, L., Favaron, V. & Lubineau, G. Macroscopic Modeling of Water Uptake Behavior of PEDOT:PSS Films. *ACS Omega* **4**, 21883–21890 (2019).

244. Tong, C. J. *et al.* Uncovering the Veil of the Degradation in Perovskite CH3NH3PbI3 upon Humidity Exposure: A First-Principles Study. *J. Phys. Chem. Lett.* **6**, 3289–3295 (2015).

245. Sajid, S. *et al.* Breakthroughs in NiOx-HTMs towards stable, low-cost and efficient perovskite solar cells. *Nano Energy* **51**, 408–424 (2018).

246. Kavadiya, S., Strzalka, J., Niedzwiedzki, D. M. & Biswas, P. Crystal reorientation in methylammonium lead iodide perovskite thin film with thermal annealing. *J. Mater. Chem. A* **7**, 12790–12799 (2019).

7 Appendix

7.1 PL Quantum Yield Measurements

Measurement and calculation of photoluminescence quantum yield (PLQY) for samples described in Section 3.3.3.

The image on the left corresponds to the measured PLQY for a sample with poor crystalline quality while the one on the right has a better crystal quality, as shown by the PLQY values.

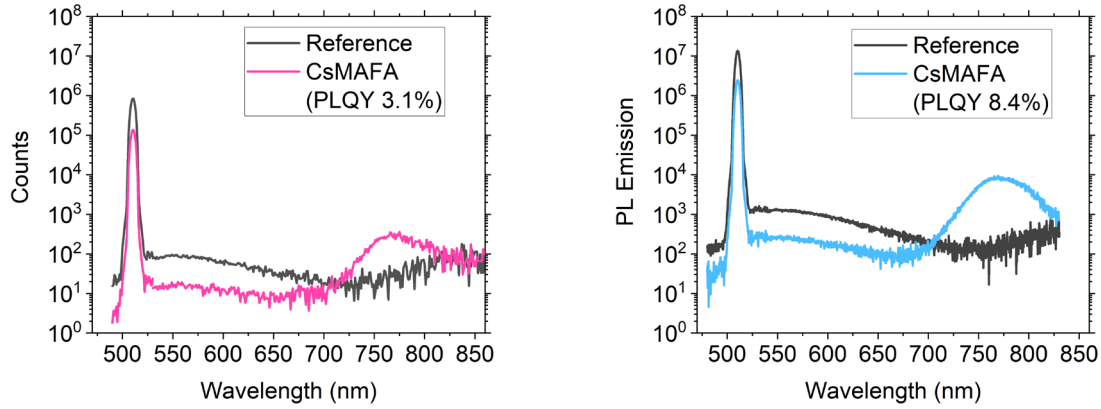

Using the "direct excitation" method (see Section 2.3.2), the curves are separated into two regions: scatter and emission. The area under the curve is then measured for both regions of a reference and a test sample. Eq. 2.15 is then applied to the resulting values. The values corresponding to the samples shown on the images above are shown in the table below. To enhance the emission of the sample, a neutral density filter was used to attenuate the scatter portion of the signal.

	Curve Integral (a.u.)	
	Sample 1	Sample 2
Sample emission	1.85E+04	4.74E+05
Reference emission	4.65E+03	2.66E+04
Sample scatter	1.35E+05	1.16E+07
Reference scatter	4.57E+06	6.48E+07
Filter (factor)	10	10
PLQY	3.1%	8.4%

On average, poor quality crystal samples showed a PLQY of 2.8 ± 0.2% while better quality crystals showed 8.3 ± 0.1%.

7.2 SEM Images and XRD of Triple Cation Layers

Supporting Images for Section 3.2. Figures a) and b) show surface and cross-section SEM images, respectively, as well as c) an XRD diffractogram of a typical CsMAFA layer used for the PL quenching experiments.[139]

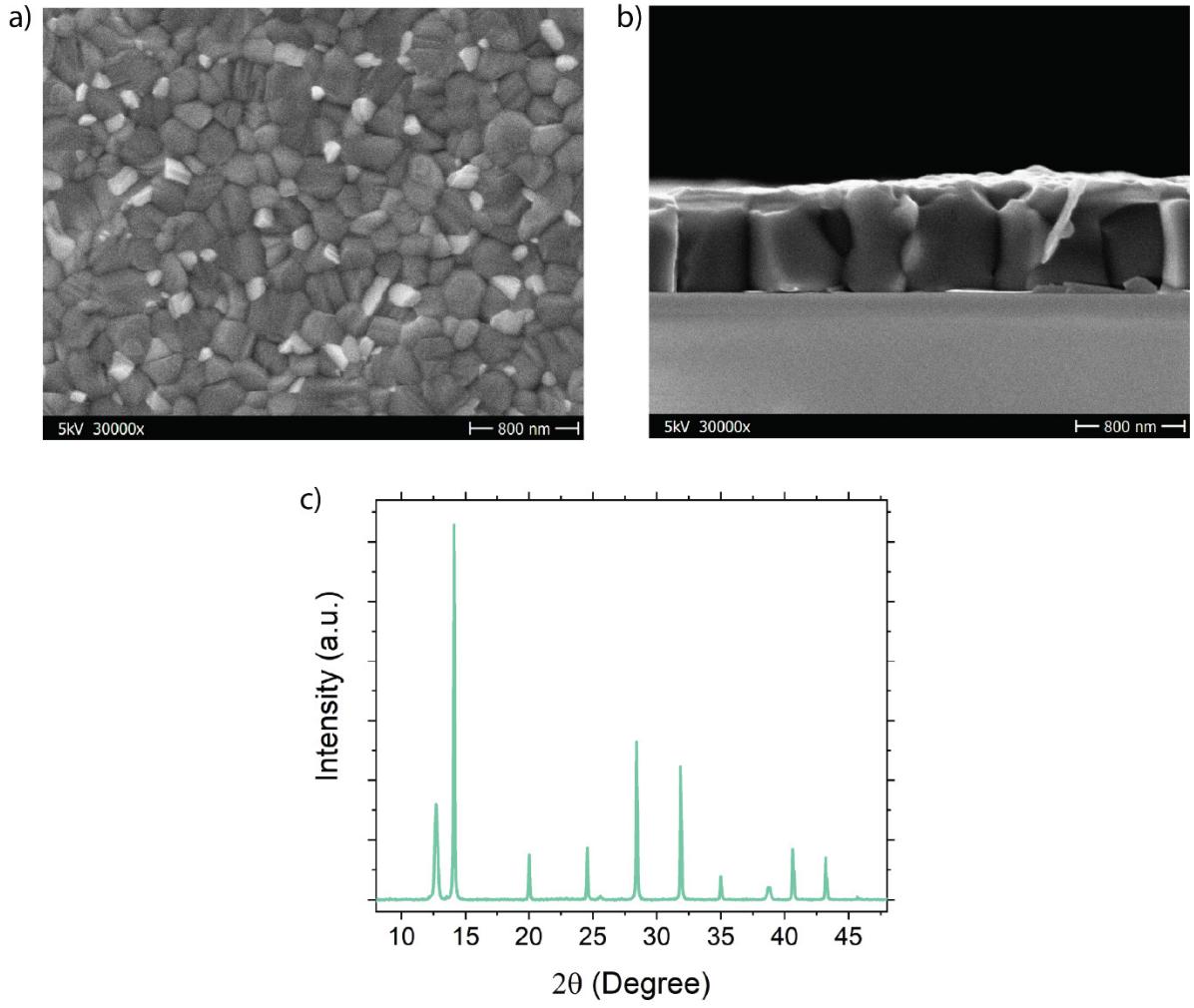

7.3 Simulations of Nitrogen Flow Velocity

Section cut view of the vacuum chamber 3D model. Done on Autodesk Inventor by Paul Zybarth and modified by Edgar Nandayapa.

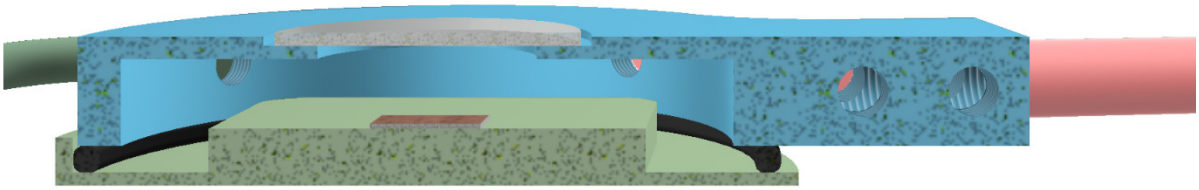

Simulations of nitrogen flow inside of the vacuum chamber on the XY plane. Using Autodesk CFD Ultimate 2019, the chamber was set to 20 °C and 20 mbar. Increasing flow velocities of 0.01, 0.10, and 1.00 L/s were set to the in- and outlets. Additionally, the inlets were set to a pressure of 20 mbar and the outlets to 0 mbar.

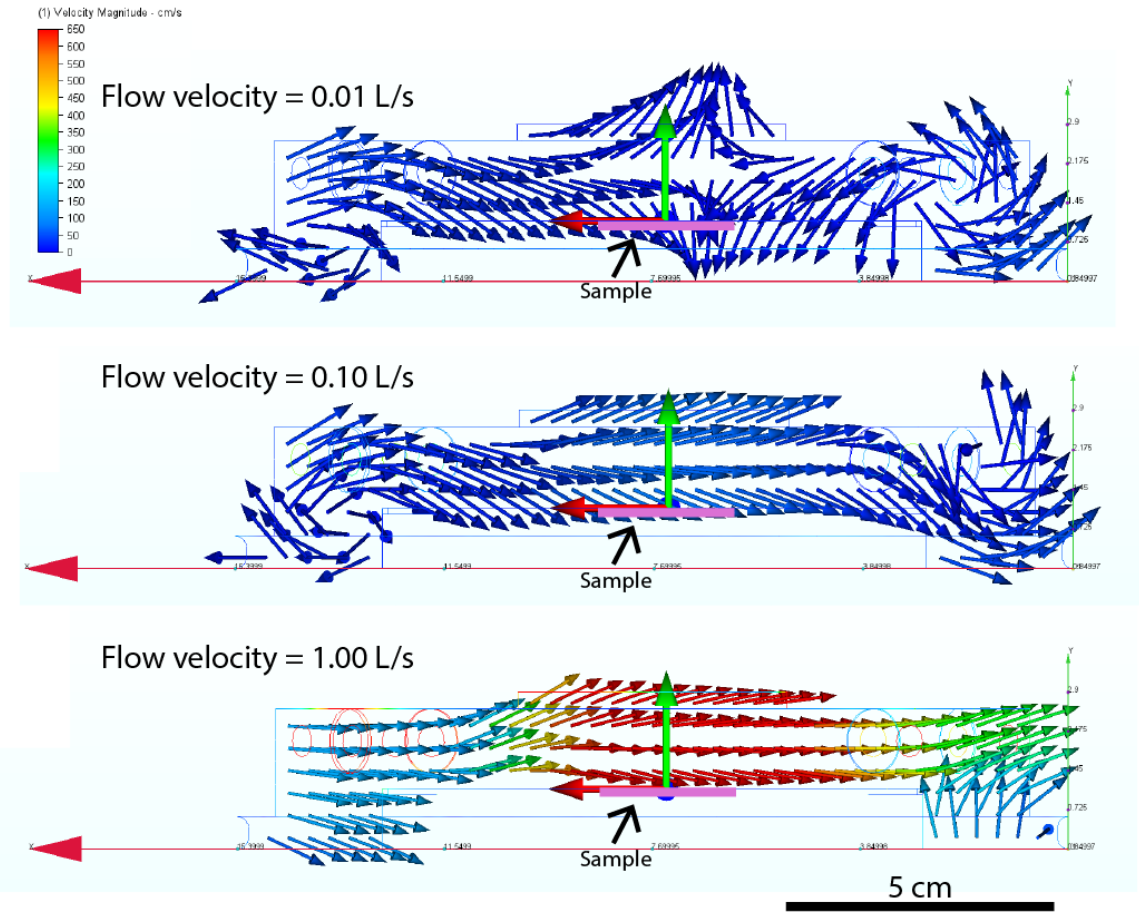

7.4 Simulations of Nitrogen Flow Inside of the Chamber

(Top) 3D model of the vacuum chamber used for the Flow Control technique. The design was done on Autodesk Inventor by Paul Zybarth and modified by Edgar Nandayapa. (Bottom) Simulation showing the nitrogen flow inside of the chamber, performed on Autodesk CFD Ultimate 2019.

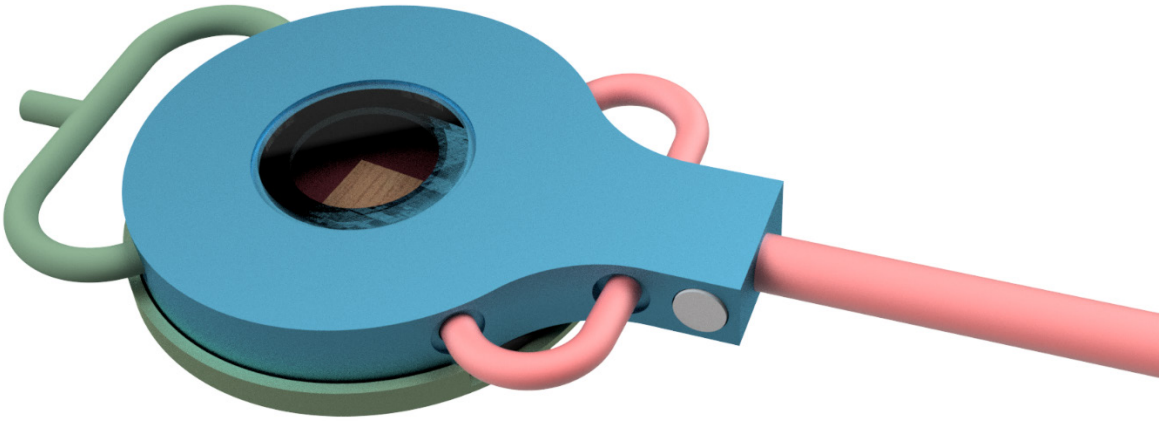

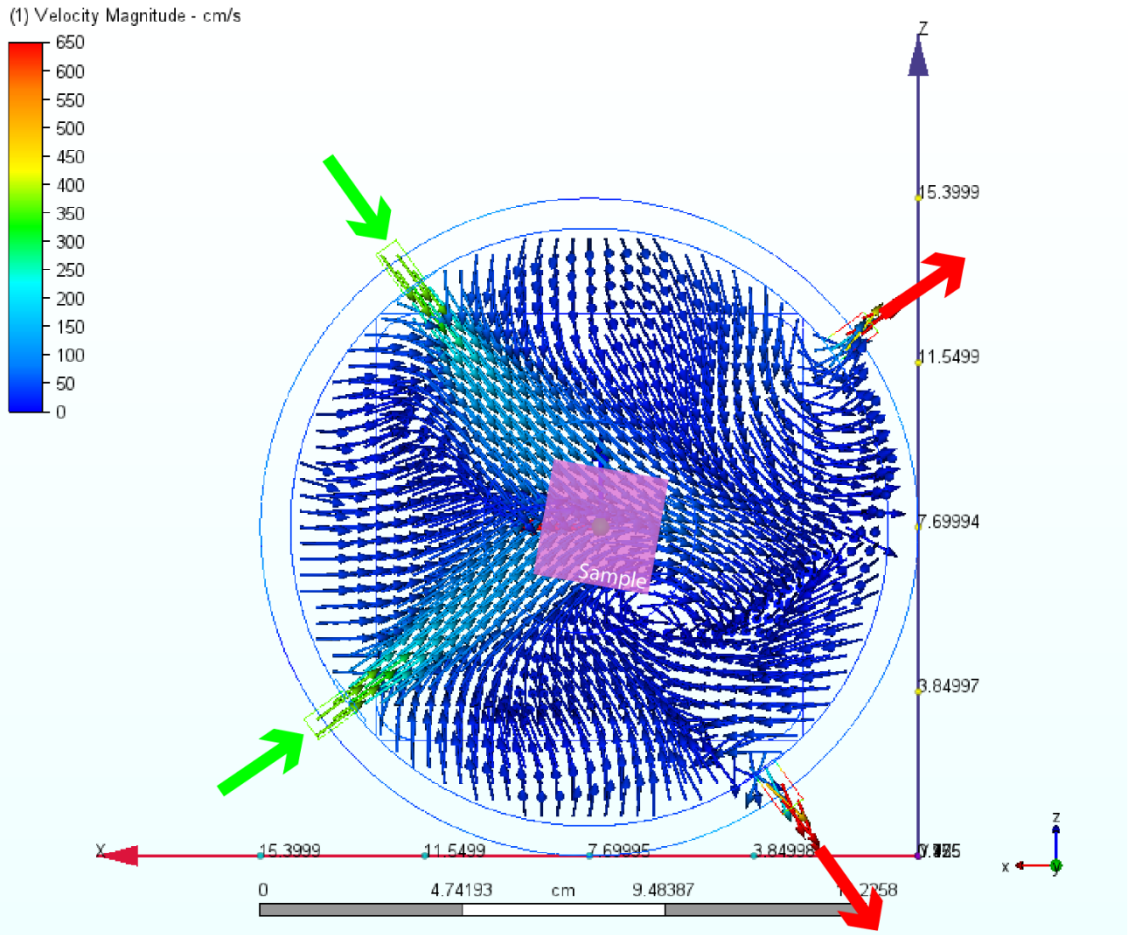

7.5 Distribution of Printed Devices using Flow Control

Boxplot distribution of voltage, current, fill factor and power conversion efficiency achieved by all inkjet-printed devices using the Flow Control technique. Shunted devices were filtered out of these diagrams.

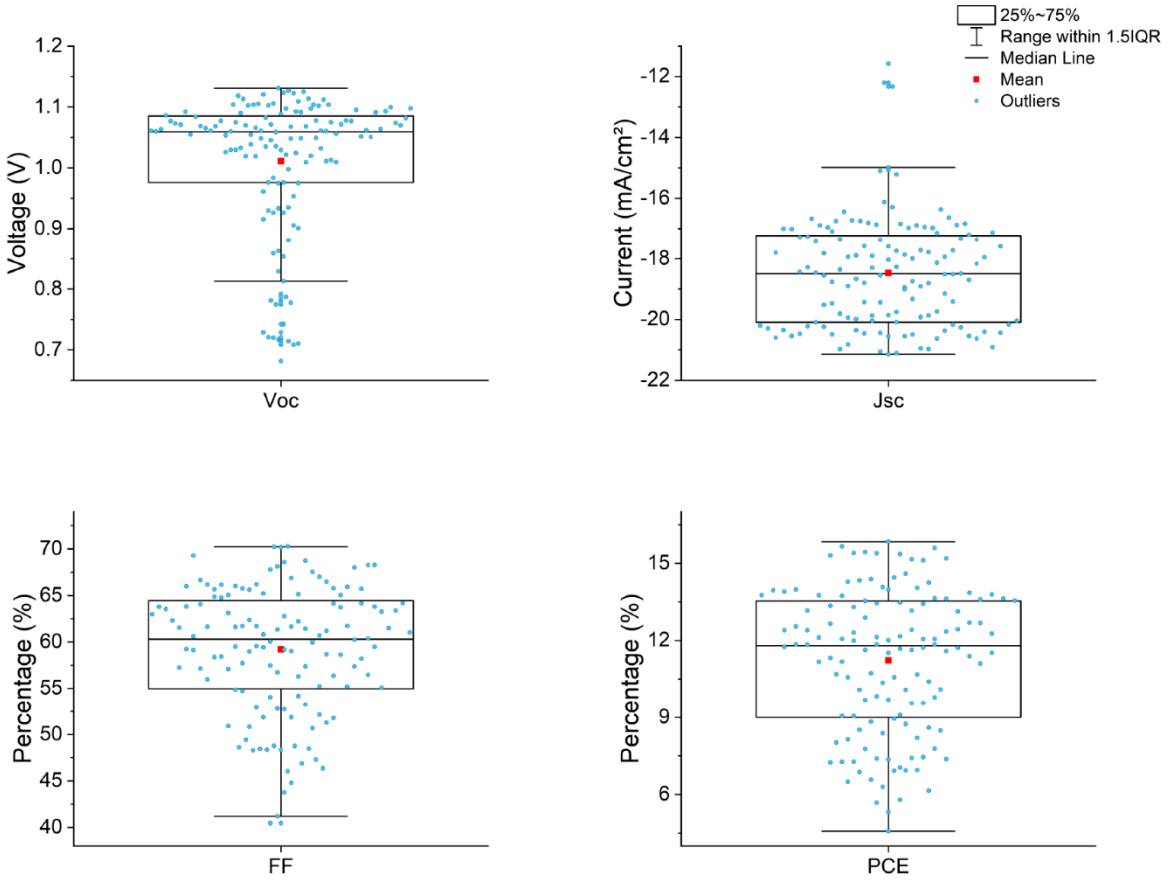

7.6 Flow Control Technique: SEM images

Supporting SEM images showing the crystal size and layer thickness induced by contents of 0, 2, 20 and 50 vol.% of GBL in the perovskite ink (above). Additionally, the effect of delaying the vacuum step process by 10, 40, 70 and 100 seconds (below)

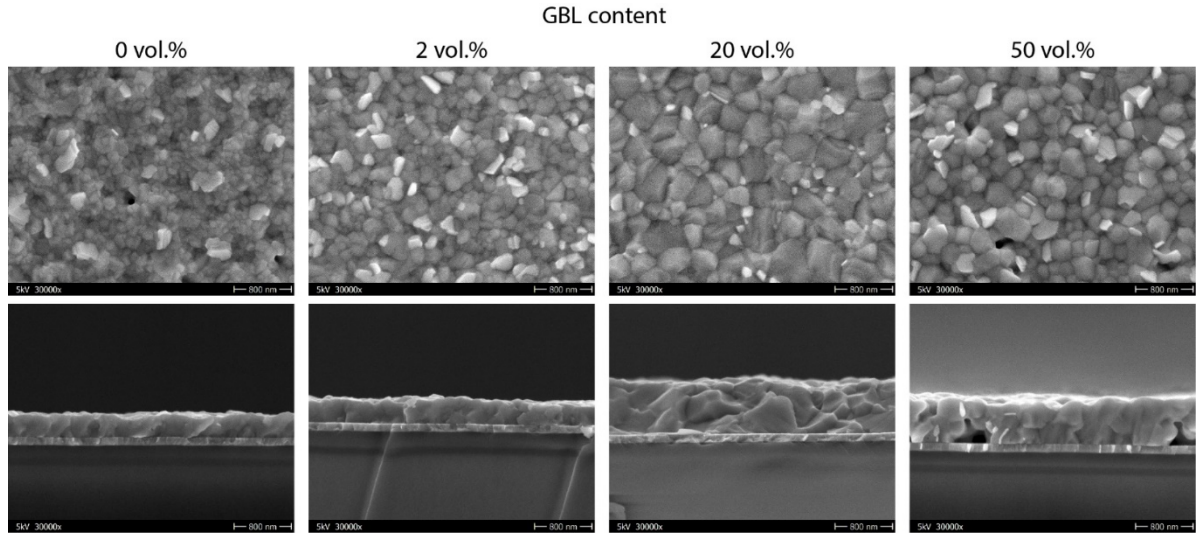

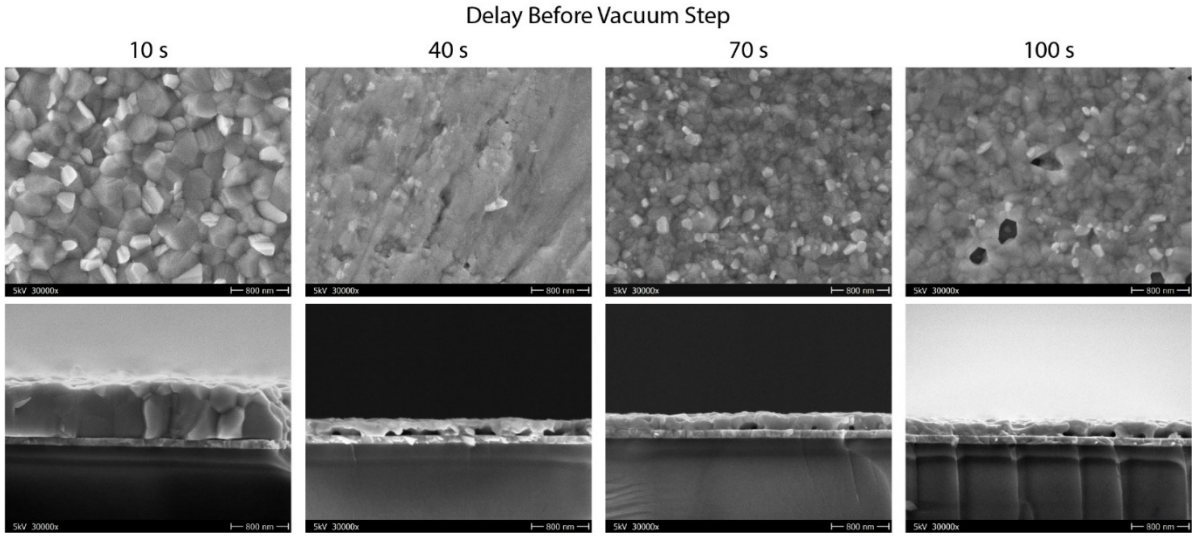

7.7 Python GUI: Data Recorder of Vacuum Process

This code was used to simultaneously record data from three sensors – a microscope, a pressure gauge and a PL spectrometer – during the annealing process of the Flow Control Technique, from Section 4.5. It additionally gathers metadata from the printer LP50 and plots all the gathered data from the sensors.

```
from tkinter import *
from tkinter import ttk
from tkinter import filedialog
from PIL import Image, ImageTk
import cv2
import numpy as np
import matplotlib
import matplotlib.pyplot as plt
matplotlib.use('Agg')
from matplotlib.backends.backend_tkagg import FigureCanvasTkAgg
from matplotlib.figure import Figure
from glob import glob
import time
from datetime import datetime, timedelta
import pandas as pd
import serial
from seabreeze.spectrometers import Spectrometer
import pyautogui
import sys
import os
from scipy import stats
from xml_reader import xml_reader as xr

class Vacuum_GUI:
def __init__(self):
self.root = Tk()
self.mic_intVar = BooleanVar(value=False)
self.pre_intVar = BooleanVar(value=False)
self.PLs_intVar = BooleanVar(value=False)
ttk.Label(self.root,text = "\n   Select available sensors\t\n").grid(row = 0, column = 0)
mic_checkbox = ttk.Checkbutton(self.root, text = "Microscope", variable=self.mic_intVar, onvalue=True, offvalue=False)
pre_checkbox = ttk.Checkbutton(self.root, text = "Pressure", variable=self.pre_intVar, onvalue=True, offvalue=False)
PLs_checkbox = ttk.Checkbutton(self.root, text = "PL spectra", variable=self.PLs_intVar, onvalue=True, offvalue=False)
cont_button = ttk.Button(self.root, text = "Continue",width = 10,command=self.select_sensors)
mic_checkbox.grid(row = 1,column = 0, padx = 10, pady = 3, sticky = "nsew")
pre_checkbox.grid(row = 2,column = 0, padx = 10, pady = 3, sticky = "nsew")
PLs_checkbox.grid(row = 3,column = 0, padx = 10, pady = 3, sticky = "nsew")
cont_button.grid(row = 6,column = 0, padx = 3, pady = 3, sticky = "nsew")

def select_sensors(self):
self.isMic = self.mic_intVar.get()
self.isCam = False
self.isPressure = self.pre_intVar.get()
self.isSpectro = self.PLs_intVar.get()
self.root.withdraw()
self.create_widgets()

def create_widgets(self):
## ~ ~ ~ ~ ~ ~ ~ ~ ~ ~ ~ ~ ~ ~ ~ ~ Main window setup ~ ~ ~ ~ ~ ~ ~ ~ ~ ~ ~ ~ ~ ~ ~ ~ ~ ~ ~ ~
self.master = Toplevel()
self.master.title("Vacuum chamber process")
self.master.geometry ("1280x800+0+0") #Size of Main Window
self.master.rowconfigure(0, weight = 1) #Resizing of Main window will resize each frame individually 1-to-1
self.master.rowconfigure(1, weight = 1)
self.master.columnconfigure(0, weight = 1)
self.master.columnconfigure(1, weight = 1)
self.master.columnconfigure(2, weight = 1)
## Configuration of Styles. They make fonts and buttons look the same
self.style = ttk.Style()
self.style.configure("frameST.TLabelframe", height = 400, width = 100, padding = (30,15), fill="both")
self.style.configure("frameST2.TLabelframe", height = 400, width = 50, padding = (10,10), fill="both")
self.style.configure("txtST.TLabel", foreground = "black", font = ("Arial", 12, "normal"))
self.style.configure("bigST.TLabel", foreground = "black",font = ("Arial", 24, "bold"))
self.style.configure("redST.TLabel", foreground = "red",font = ("Arial", 24, "bold"))
self.style.configure("blueST.TLabel", foreground = "blue",font = ("Arial", 24, "bold"))
self.style.configure("fieldST.TLabel", foreground = "black", font = ("Arial", 14, "bold"), justify = CENTER)
self.style.configure("entryST.TEntry", font = ("Arial", 16, "normal"))
self.style.configure("canvasST.TCanvas", bg = "white", width = 300, height = 200)
self.style.configure("StaStoStyle.TButton", foreground = "blue", font = ("Arial", 14, "bold"),width=5)
self.style.configure("StopStyle.TButton", background = "red", foreground = "black", font = ("Arial", 18, "bold"),width=5)
self.style.map("StaStoStyle.TButton", foreground = [("pressed", "red")])

## ~ ~ ~ ~ ~ ~ ~ ~ ~ ~ ~ ~ ~ ~ ~ ~ Initialization of processes  ~ ~ ~ ~ ~ ~ ~ ~ ~ ~ ~ ~ ~ ~ ~ ~ ~ ~ ~ ~
### Setup cameras
if self.isMic:
self.cap_MIC = cv2.VideoCapture(0)
self.current_image_MIC = None
self.fps_entry = 30  # Initializes frames-per-second
### Setup Spectrometer (OceanOptics Flame)
if self.isSpectro:
```

```
81.  # self.spec = Spectrometer.from_first_available()
82.  self.spec = Spectrometer.from_serial_number(serial="FLMS15932")
83.  self.spec.integration_time_micros(100000)
84.  self.spec_waveL = self.spec.wavelengths()[2:]
85.  self.spec_counts = []
86.  ### Setup pressure sensor
87.  if self.isPressure:
88.  self.pressureSensor = serial.Serial("COM3")
89.  self.pressureSensor.baudrate = 9600
90.  self.pressureSensor.bytesize = 8
91.  self.pressureSensor.parity = 'N'
92.  self.pressureSensor.stopbits = 1
93.  self.pressureArray = []
94.  self.timeElapArray = []
95.  self.plot_ratio = 3/4 #For image 4:3
96.  ### Setup Plots
97.  self.fig_pls = Figure()#figsize=[4,3])
98.  self.ax1 = self.fig_pls.add_subplot(111)
99.  self.fig_pres = Figure()#figsize=[4,3])
100. self.ax2 = self.fig_pres.add_subplot(111)
101. ### running process refers to saving data
102. self.runningProcess = False
103. self.startP = False
104. self.delay = 0
105.
106. ## ~ ~ ~ ~ ~ ~ ~ ~ ~ ~ ~ ~ ~ ~ ~ Frame configurations ~ ~ ~ ~ ~ ~ ~ ~ ~ ~ ~ ~ ~ ~ ~ ~ ~ ~ ~
107. ## - - - - - Pressure frame - - - - -
108. self.pressure_frame = ttk.LabelFrame(self.master)
109. self.pressure_frame.config(style="frameST.TLabelframe",text = "Pressure")
110. self.pressure_frame.grid(row=0,column=0,columnspan=2)
111. self.pres_label = ttk.Label(self.pressure_frame, text = "Current Pressure")
112. self.rate_label = ttk.Label(self.pressure_frame, text = "Current Rate")
113. self.presLive_label = ttk.Label(self.pressure_frame, text = "0.00 E-2 mbar")
114. self.rateLive_label = ttk.Label(self.pressure_frame, text = "0.00 L/s")
115. self.pres_image = FigureCanvasTkAgg(self.fig_pres, master=self.pressure_frame)
116. self.pres_label.config(style = "txtST.TLabel", justify = LEFT, anchor = "sw")
117. self.rate_label.config(style = "txtST.TLabel", justify = RIGHT, anchor = "se")
118. self.presLive_label.config(style = "fieldST.TLabel", justify = CENTER, anchor = "sw")
119. self.rateLive_label.config(style = "fieldST.TLabel", justify = CENTER, anchor = "se")
120. self.pres_image.get_tk_widget().grid(padx = 10, row=0,column=0, columnspan=2)
121. self.pres_label.grid(padx = 10, row=1,column=0)
122. self.rate_label.grid(padx = 10, row=1,column=1)
123. self.presLive_label.grid(padx = 30, row=2,column=0)
124. self.rateLive_label.grid(padx = 30, row=2,column=1)
125.
126. ## - - - - - Microscope frame - - - - -
127. self.microscope_frame = ttk.LabelFrame(self.master)
128. self.microscope_frame.config(style="frameST.TLabelframe",text = "Microscope")
129. self.microscope_frame.grid(row=0,column=1,columnspan=2)
130. framespersecond = StringVar()
131. self.fps_label = ttk.Label(self.microscope_frame, text = "FPS selection")
132. self.ftt_label = ttk.Label(self.microscope_frame, text = "Frames Taken")
133. self.ftt_labelLive = ttk.Label(self.microscope_frame, text = "000") ##ftt=frames total
134. self.fps_entry = ttk.Combobox(self.microscope_frame, textvariable = framespersecond)
135. self.micro_image = Label(self.microscope_frame)
136. self.ftt_label.config(style = "txtST.TLabel", justify = LEFT, anchor = "sw")
137. self.fps_label.config(style = "txtST.TLabel", justify = RIGHT, anchor = "se")
138. self.ftt_labelLive.config(style = "fieldST.TLabel", anchor = "se")
139. self.fps_entry.config(width = 5, values = ("30","20","15","10","6","5","2","1"))
140. self.micro_image.grid(row=0,column=0, columnspan=2)
141. self.ftt_label.grid(padx = 10, row=1,column=1)
142. self.fps_label.grid(padx = 10, row=1,column=0)
143. self.ftt_labelLive.grid(padx = 30, row=2,column=1)
144. self.fps_entry.grid(padx = 30, row=2,column=0)
145.
146. ## - - - - - Photoluminescence (Notebook) frame - - - - -
147. self.PL_frame = ttk.LabelFrame(self.master)
148. self.PL_frame.config(style="frameST.TLabelframe",text = "Photoluminescence")
149. self.PL_frame.grid(row=1,column=0)
150. self.PLNo_image = FigureCanvasTkAgg(self.fig_pls, master=self.PL_frame)
151. self.PL2dButton = BooleanVar()
152. self.PL2D_button = ttk.Checkbutton(self.PL_frame, text="2D View", variable=self.PL2dButton,
153. command=lambda: self.test(self.PL2dButton))
154. self.PLNo_image.get_tk_widget().pack()
155. self.PL2D_button.pack(expand=True)
156.
157. ## - - - - - Config frame - - - - -
158. self.config_frame = ttk.LabelFrame(self.master)
159. self.config_frame.config(style="frameST2.TLabelframe",text = "Config")
160. self.config_frame.grid(row=1,column=1)
161. self.fileLabel = ttk.Label(self.config_frame, style = "txtST.TLabel", text = "Sample Name").grid(row=1,column=0, columnspan=2)
162. self.fileEntry = ttk.Entry(self.config_frame, width = 20)
163. self.histButton = ttk.Button(self.config_frame, text = "History",width = 7, command=self.display_history).grid(row=2,column=1, sticky=E)
164. self.fileEntry.insert(0,'Sample')
165. self.fileEntry.grid(row=2,column=0, columnspan=2,sticky=W)
166. if glob('C:\\Users\\LP50\\Desktop\\Edgar\\'):
167. self.folder_path = 'C:\\Users\\LP50\\Desktop\\Edgar\\'
168. elif glob('F:\\Seafile\\IJPrinting_Edgar-Florian\\'):
169. self.folder_path = 'F:\\Seafile\\IJPrinting_Edgar-Florian\\'
170. else:
171. self.folder_path = 'D:\\vacgui_test\\'
172. self.folderLabel = ttk.Label(self.config_frame,style = "txtST.TLabel", text = "Folder Location").grid(row=3,column=0, columnspan=2)
173. self.folderEntry = ttk.Entry(self.config_frame, width = 27)
174. self.folderEntry.insert(0,self.folder_path)
175. self.folderButton = ttk.Button(self.config_frame, text = "...",width = 3, command=self.browseButton).grid(row=4,column=0)
176. self.folderEntry.grid(row=4,column=1)
177. ttk.Label(self.config_frame, text = "\n").grid(row=5,column=0, columnspan=2)
178. self.startButton = ttk.Button(self.config_frame,command = self.startProcess, text = "Start")
179. self.startButton.config(style = "StaStoStyle.TButton")
180. self.stopButton = ttk.Button(self.config_frame,command = self.stopProcess, text = "Stop")
181. self.stopButton.config(style = "StopStyle.TButton")
```

```
182.  self.startButton.grid(row=6,column=0, columnspan=2)
183.  self.elapsedVar = StringVar()
184.  self.elapsedVar.set("00:00")
185.  self.elaptimLabel = ttk.Label(self.config_frame,style = "txtST.TLabel", text = "\nElapsed Time").grid(row=7,column=0, columnspan=2)
186.  self.elapsedLabel = ttk.Label(self.config_frame,style ="bigST.TLabel", textvariable = self.elapsedVar)
187.  self.elapsedLabel.grid(row=8,column=0, columnspan=2)
188.
189.  ## - - - - - Live variables frame - - - - -
190.  self.LiveVar_frame = ttk.LabelFrame(self.master)
191.  self.LiveVar_frame.config(style="frameST2.TLabelframe",text = "Variables")
192.  self.LiveVar_frame.grid(row=1,column=2)
193.  ttk.Label(self.LiveVar_frame, style = "txtST.TLabel", text = "Printer settings").grid(row=0,column=0,columnspan=4)
194.  ttk.Label(self.LiveVar_frame, style = "txtST.TLabel", text = "Active Nozzles").grid(row=1,column=0)
195.  ttk.Label(self.LiveVar_frame, style = "txtST.TLabel", text = "Print Speed").grid(row=2,column=0)
196.  ttk.Label(self.LiveVar_frame, style = "txtST.TLabel", text = "Quality Factor").grid(row=3,column=0)
197.  ttk.Label(self.LiveVar_frame, style = "txtST.TLabel", text = "Resolution").grid(row=4,column=0)
198.  ttk.Label(self.LiveVar_frame, style = "txtST.TLabel", text = "Printhead Temp").grid(row=1,column=2)
199.  ttk.Label(self.LiveVar_frame, style = "txtST.TLabel", text = "Substrate Temp").grid(row=2,column=2)
200.  ttk.Label(self.LiveVar_frame, style = "txtST.TLabel", text = "Voltage").grid(row=3,column=2)
201.  ttk.Label(self.LiveVar_frame, style = "txtST.TLabel", text = "Swaths").grid(row=4,column=2)
202.  ttk.Label(self.LiveVar_frame, style = "txtST.TLabel", text = "Wait Time").grid(row=5,column=0)
203.  ttk.Label(self.LiveVar_frame, style = "txtST.TLabel", text = "Total Time").grid(row=5,column=2)
204.  self.intVar_waitT = IntVar()
205.  self.intVar_totalT = IntVar()
206.  self.varLabel1 = ttk.Entry(self.LiveVar_frame, width = 5, style = "entryST.TEntry")
207.  self.varLabel2 = ttk.Entry(self.LiveVar_frame, width = 5)
208.  self.varLabel3 = ttk.Entry(self.LiveVar_frame, width = 5, text = "QF")
209.  self.varLabel4 = ttk.Entry(self.LiveVar_frame, width = 5, text = "")
210.  self.varLabel5 = ttk.Entry(self.LiveVar_frame, width = 5, text = "30")
211.  self.varLabel6 = ttk.Entry(self.LiveVar_frame, width = 5, text = "20")
212.  self.varLabel7 = ttk.Entry(self.LiveVar_frame, width = 5, text = "100")
213.  self.varLabel8 = ttk.Entry(self.LiveVar_frame, width = 5, text = "12")
214.  self.varLabelWT = ttk.Entry(self.LiveVar_frame, width = 5, text=self.intVar_waitT)
215.  self.varLabelTT = ttk.Entry(self.LiveVar_frame, width = 5, text=self.intVar_totalT)
216.  self.varLabel1.grid(row=1,column=1)
217.  self.varLabel2.grid(row=2,column=1)
218.  self.varLabel3.grid(row=3,column=1)
219.  self.varLabel4.grid(row=4,column=1)
220.  self.varLabel5.grid(row=1,column=3)
221.  self.varLabel6.grid(row=2,column=3)
222.  self.varLabel7.grid(row=3,column=3)
223.  self.varLabel8.grid(row=4,column=3)
224.  self.varLabelWT.grid(row=5,column=1)
225.  self.varLabelTT.grid(row=5,column=3)
226.  self.repopulate_button = ttk.Button(self.LiveVar_frame, text = u"\u2B6F", width = 3, command=self.repopulate_metafields)
227.  self.repopulate_button.grid(row=6,column=3, sticky=E)
228.  ttk.Label(self.LiveVar_frame, style = "txtST.TLabel", text = "").grid(row=5,column=0, columnspan=4)
229.  ttk.Label(self.LiveVar_frame, style = "txtST.TLabel", text = "Ink Details").grid(row=6,column=0, columnspan=4)
230.  ttk.Label(self.LiveVar_frame, style = "txtST.TLabel", text = "Perovskite").grid(row=7,column=0)
231.  ttk.Label(self.LiveVar_frame, style = "txtST.TLabel", text = "Adds.").grid(row=7,column=2, sticky=E)
232.  ttk.Label(self.LiveVar_frame, style = "txtST.TLabel", text = "Solvents").grid(row=8,column=0)
233.  ttk.Label(self.LiveVar_frame, style = "txtST.TLabel", text = "Ratio").grid(row=8,column=2, sticky=E)
234.  ttk.Label(self.LiveVar_frame, style = "txtST.TLabel", text = "Conc.").grid(row=9,column=2, sticky=E)
235.  ttk.Label(self.LiveVar_frame, style = "txtST.TLabel", text = "Substrate").grid(row=9,column=0)
236.
237.  ttk.Label(self.LiveVar_frame, style = "txtST.TLabel", text = "").grid(row=10,column=0, columnspan=4)
238.  ttk.Label(self.LiveVar_frame, style = "txtST.TLabel", text = "Glovebox Variables").grid(row=11,column=0, columnspan=4)
239.  ttk.Label(self.LiveVar_frame, style = "txtST.TLabel", text = "Temperature").grid(row=12,column=0)
240.  ttk.Label(self.LiveVar_frame, style = "txtST.TLabel", text = "H2O content").grid(row=13,column=0)
241.  ttk.Label(self.LiveVar_frame, style = "txtST.TLabel", text = "O2 content").grid(row=13,column=2)
242.  ttk.Label(self.LiveVar_frame, style = "txtST.TLabel", text = "Comments:").grid(row=14,column=0)
243.  self.varEntry_Pe = ttk.Entry(self.LiveVar_frame, width = 10)
244.  self.varEntry_Ad = ttk.Entry(self.LiveVar_frame, width = 5)
245.  self.varEntry_So = ttk.Entry(self.LiveVar_frame, width = 15)
246.  self.varEntry_Ra = ttk.Entry(self.LiveVar_frame, width = 5)
247.  self.varEntry_Su = ttk.Entry(self.LiveVar_frame, width = 10)
248.  self.varEntry_Co = ttk.Entry(self.LiveVar_frame, width = 5)
249.  self.varEntry_Te = ttk.Entry(self.LiveVar_frame, width = 5)
250.  self.varEntry_Wa = ttk.Entry(self.LiveVar_frame, width = 5)
251.  self.varEntry_Ox = ttk.Entry(self.LiveVar_frame, width = 5)
252.  self.varEntry_cc = ttk.Entry(self.LiveVar_frame, width = 27)
253.  self.varEntry_Pe.grid(row=7,column=1,columnspan=2, sticky=W)
254.  self.varEntry_Ad.grid(row=7,column=3)
255.  self.varEntry_So.grid(row=8,column=1,columnspan=2, sticky=W)
256.  self.varEntry_Ra.grid(row=8,column=3)
257.  self.varEntry_Su.grid(row=9,column=1,columnspan=2, sticky=W)
258.  self.varEntry_Co.grid(row=9,column=3)
259.  self.varEntry_Te.grid(row=12,column=1)
260.  self.varEntry_Wa.grid(row=13,column=1)
261.  self.varEntry_Ox.grid(row=13,column=3)
262.  self.varEntry_cc.grid(row=14,column=1,columnspan=3, sticky=W)
263.
264.  ## Start the program
265.  self.todaydate = datetime.now().strftime("%Y%m%d")
266.  self.datePath = self.folder_path+"\\"+self.todaydate+"\\"
267.  self.master.protocol("WM_DELETE_WINDOW", self.close_window)
268.  self.processes_loop()
269.
270.  ## ~o~o~o~o~o~o~o~o~o Administrative functions o~o~o~o~o~o~o~o~o~
271.  def create_date_folder(self):
272.  #Sample name and folder path
273.  if not os.path.exists(self.datePath):
274.  os.mkdir(self.datePath)
275.  print("created date folder "+self.datePath)
276.  else:
277.  pass
278.  def display_history(self):
279.  ##Create Windows
280.  self.hist = Toplevel()
281.  ## Gather metadata
282.  file_list = glob(self.datePath+'\\*\\*metadata.csv')
```

```
file_names = []
files_df = []
for p in file_list:
file_names.append(p.rsplit("\\",2)[-2])
df = pd.read_csv(p, index_col=0, header=0, parse_dates=True,error_bad_lines=False)
files_df.append(df)
dframe = pd.concat(files_df, axis=1, ignore_index=True)
dframe.columns = file_names
##Fix metadata structure
dframe = dframe.transpose()
dframe["DateTime"] = pd.to_datetime(dframe["DateTime"], format="%d.%m.%Y-%H:%M:%S", errors="ignore")
dframe.sort_values(by="DateTime", inplace=True)
## get relevant metadata
cols_names = ["DateTime","Comments"]
hist_text = ''
done_count = 0
for r, dF in enumerate(dframe.index):
single_text = dF+"\t"
for cn in cols_names:
if cn =="DateTime":
if dframe[cn][dF] + timedelta(minutes=33) < datetime.now():
single_text = "**"+single_text+dframe[cn][dF].strftime('%H:%M:%S') +"\t\t"
done_count += 1
else:
single_text = single_text+dframe[cn][dF].strftime('%H:%M:%S') +"\t\t"
else:
single_text = single_text+ str(dframe[cn][dF]) +"\t"

hist_text = hist_text+single_text+"\n"
hist_text = "%s \nSamples ready: %d/%d" %(hist_text,done_count,len(file_list))

ttk.Label(self.hist, style = "txtST.TLabel", text = hist_text).grid(row=0,column=0)

def create_sample_folder(self, retries=1):
self.sample_name = self.fileEntry.get()
self.full_path = self.datePath+self.sample_name+"\\"
if os.path.exists(self.full_path):
self.full_path =self.full_path[:-1]+"_dup"+str(retries)+"\\"
if os.path.exists(self.full_path):
retries +=1
self.create_sample_folder(retries)
else:
os.mkdir(self.full_path)
print("created duplicated folder "+self.full_path)
else:
os.mkdir(self.full_path)
print("created sample folder "+self.full_path)

def browseButton(self):
self.folder_path = filedialog.askdirectory()
self.folderEntry.delete(0, 'end')
self.folderEntry.insert(0,self.folder_path)
return self.folder_path

def list_measured_samples(self):
all_meas_samples = []
sample_list = glob(self.folder_path+"*")
for sl in sample_list:
nameholder = sl.split("\\")[-1]
all_meas_samples.append(nameholder)

def set_text_metavalues(self):
label_vars = [self.varLabel1,self.varLabel2,self.varLabel3,self.varLabel4,
self.varLabel5,self.varLabel6,self.varLabel7,self.varLabel8]
label_names = ["ActiveNozzles","PrintSpeed","QualityFactor","XResolution",
"PrintHeadTemperature","SubstrateTemperature","AVoltage",
"Swaths"]
for n,lvs in enumerate(label_vars):
lvs["text"] = self.xml_data[label_names[n]]

def get_entry_metavalues(self):
## Save input values from User, related to perovskite ink and Glovebox
user_input_names = ["ActiveNozzles","PrintSpeed","QualityFactor","XResolution",
"PrintHeadTemperature","SubstrateTemperature","AVoltage","Swaths",
"WaitRunTime","TotalRunTime",
"PerovskiteType","PerovskiteSolvents","PerovskiteSolventsRatio",
"GloveboxTemperature(c)","GloveboxH2Ocontent(ppm)","GloveboxO2content(ppm)","Comments",
"Additives","Concentration","Substrate"]
user_input_vars = [self.varLabel1,self.varLabel2,self.varLabel3,self.varLabel4,
self.varLabel5,self.varLabel6,self.varLabel7,self.varLabel8,
self.varLabelWT,self.varLabelTT,
self.varEntry_Pe,self.varEntry_So,self.varEntry_Ra,
self.varEntry_Te,self.varEntry_Wa,self.varEntry_Ox,self.varEntry_cc,
self.varEntry_Ad, self.varEntry_Co, self.varEntry_Su]
for c,uin in enumerate(user_input_names):
self.xml_data[uin] = user_input_vars[c].get()
#add current time and date
now = datetime.now()
self.xml_data["DateTime"]=now.strftime("%d.%m.%Y-%H:%M:%S")

def repopulate_metafields(self):
todaydate = datetime.now().strftime("%Y%m%d")
metafile = sorted(glob(self.folder_path+"\\"+todaydate+"\\*\\*metadata.csv"),key=os.path.getmtime)[-1]
meta_df = pd.read_csv(metafile, header=None, index_col=0, squeeze=True)
user_input_names = ["PerovskiteType","PerovskiteSolvents","PerovskiteSolventsRatio",
"GloveboxTemperature(c)","GloveboxH2Ocontent(ppm)","GloveboxO2content(ppm)","Comments",
"Additives","Concentration","Substrate",
"WaitRunTime","TotalRunTime",
"ActiveNozzles","PrintSpeed","QualityFactor","XResolution",
"PrintHeadTemperature","SubstrateTemperature","AVoltage","Swaths"]
user_input_vars = [self.varEntry_Pe,self.varEntry_So,self.varEntry_Ra,
```

```
384.  self.varEntry_Te,self.varEntry_Wa,self.varEntry_Ox,self.varEntry_cc,
385.  self.varEntry_Ad, self.varEntry_Co, self.varEntry_Su,
386.  self.varLabelWT,self.varLabelTT,
387.  self.varLabel1,self.varLabel2,self.varLabel3,self.varLabel4,
388.  self.varLabel5,self.varLabel6,self.varLabel7,self.varLabel8]
389.  for i, mdi in enumerate(user_input_names):
390.  user_input_vars[i].delete(0, 'end')
391.  user_input_vars[i].insert(0,meta_df[mdi])
392.
393.  ## ~o~o~o~o~o~o~o~o~o Sensor functions o~o~o~o~o~o~o~o~o~
394.  def readSensor_Microscope(self,timeEla):
395.  state_MIC, frame_MIC_raw = self.cap_MIC.read()
396.  hue = cv2.cvtColor(frame_MIC_raw, cv2.COLOR_BGR2HSV)[:,:,0]
397.  gray_MIC = cv2.cvtColor(frame_MIC_raw, cv2.COLOR_BGR2GRAY)
398.  frame_MIC = cv2.cvtColor(frame_MIC_raw, cv2.COLOR_BGR2RGB)
399.  ## resize image from camera (removes black frame of raw data)
400.  y = frame_MIC.shape[0]
401.  x = frame_MIC.shape[1]
402.  d = 60
403.  frame_MIC = frame_MIC[d:y-d,d:x-d]
404.  frame_MIC = cv2.resize(frame_MIC, (0,0), fx=0.8,fy=0.8)
405.  hue_arr = np.asarray(hue).reshape(-1)
406.  hue_arr = hue_arr[hue_arr > 2]
407.  if state_MIC:
408.  self.current_image_MIC = Image.fromarray(frame_MIC)
409.  imgtk_MIC = ImageTk.PhotoImage(image=self.current_image_MIC)
410.  self.micro_image.imgtk = imgtk_MIC
411.  self.micro_image.config(image=imgtk_MIC)
412.  n_bins = 180
413.  self.countsGray, _ = np.histogram(gray_MIC, list(range(n_bins))) ##Useful when spectrometer working
414.  if self.isSpectro:
415.  self.countsHue, _ = np.histogram(hue_arr, list(range(n_bins)))
416.  # print(len(self.countsHue), self.countsHue)
417.  else:
418.  self.countsHue = self.plotting_PLmic(hue_arr)
419.  if self.runningProcess:
420.  timeEla = str(round(timeEla,2)).replace(".","o")
421.  self.ftt_labelLive.config(text=str(self.frame_counter))
422.  self.frame_counter += 1
423.  try:
424.  os.mkdir(self.full_path+"images_drying\\")
425.  except:
426.  pass
427.  cv2.imwrite(self.full_path+"images_drying\\"+self.sample_name+"_"+timeEla+".jpg", frame_MIC_raw)
428.
429.  def readSensor_Spectrometer(self):
430.  s_counts = self.spec.intensities()[2:]
431.  self.plotting_PLspectra(s_counts)
432.  return s_counts
433.
434.  def readSensor_Pressure(self,timeElap):
435.  try:
436.  # pressure_value = float(self.pressureSensor.readline())
437.  self.pressureSensor.write(b"001M^\r") # sending measurement command
438.  spr = self.pressureSensor.read(12)
439.  p_val = float(spr[4:8])/1000
440.  p_exp = int(spr[8:10])-20
441.  pressure_value = p_val*10**p_exp
442.  except:
443.  pressure_value = 0
444.  if self.runningProcess:
445.  self.pressureArray.append(pressure_value)
446.  self.plotting_pressure()
447.  else:
448.  self.presLive_label.config(text = "{:.2f} mbar".format(pressure_value))
449.
450.  def readSensor_Camera(self):
451.  cv2.cvtColor()
452.  state_CAM, self.frame_CAM = self.cap_CAM.read() #Get data from Camera
453.  frame_CAM_s = cv2.cvtColor(self.frame_CAM, cv2.COLOR_BGR2RGB) #Convert color scheme
454.  frame_CAM_s = cv2.resize(frame_CAM_s, (0,0), fx=0.3,fy=0.3) #Resize image
455.  if state_CAM: ##Should be in GUI part, send frame_CAM
456.  self.current_image_CAM = Image.fromarray(frame_CAM_s)
457.  imgtk_CAM = ImageTk.PhotoImage(image=self.current_image_CAM)
458.  self.camera_image.imgtk = imgtk_CAM
459.  self.camera_image.config(image=imgtk_CAM)
460.
461.  def take_CameraPic(self):
462.  #self.folder_path
463.  try:
464.  sample_name = self.sample_combobox.get()
465.  except:
466.  sample_name = self.fileEntry.get()
467.
468.  cv2.imwrite(self.folder_path+sample_name+"\\"+sample_name+"_full_picture.jpg", self.frame_CAM)
469.
470.  ## ~o~o~o~o~o~o~o~o~o plotting functions o~o~o~o~o~o~o~o~o~
471.  def plotting_pressure(self): ## Triggered by sensor
472.  x_time = self.timeElapArray
473.  y_pres = self.pressureArray
474.  ##This should be in GUI, send x_time and y_pres
475.  self.ax2.clear()
476.  self.ax2.set_ylabel("Pressure (mbar)", fontsize=12)
477.  self.ax2.set_xlabel("Time (sec)", fontsize=12)
478.  self.ax2.grid()
479.  self.ax2.set_yscale('log')
480.  self.ax2.scatter(x_time,y_pres)
481.  chamber_volume = 0.25 #Vacuum chamber volume
482.  try:
483.  y_max=1000 #or max(y_pres)
484.  y_min=min(y_pres)
```

```
485.  t_max = x_time[y_pres.index(y_min)]##This might return an array, fix it
486.  except:
487.  y_max=0
488.  y_min=0
489.  t_max = 0
490.  try:
491.  rate = chamber_volume/t_max*np.log(y_max/y_min)#
492.  except:
493.  rate = 0
494.  self.pres_image.draw() #Plotted image
495.  self.presLive_label.config(text = "{:.2f} mbar".format(y_pres[-1]))
496.  self.rateLive_label.config(text = "{:.2f} L/s".format(rate))
497.
498.  def plotting_PLmic(self,arr): ## Triggered by sensor
499.  self.ax1.clear()
500.  self.ax1.set_title ("Color distribution", fontsize=14)
501.  self.ax1.set_ylabel("Counts", fontsize=12)
502.  self.ax1.set_xlabel("Color Hue", fontsize=12)
503.  plt.rcParams['xtick.top'] = True
504.  n_bins = 180
505.  counts,_,_ = self.ax1.hist(arr, n_bins)
506.  self.ax1.text(0.1, 0.9,'Max at {}'.format(np.argmax(counts)), transform=self.ax1.transAxes)
507.  self.ax1.set_aspect(1.0/self.ax1.get_data_ratio()*self.plot_ratio)
508.  self.PLNo_image.draw()
509.  return counts
510.
511.  def plotting_PLspectra(self, y_cnt): ## Triggered by loop
512.  self.ax1.clear()
513.  self.ax1.set_title ("Wavelength", fontsize=14)
514.  self.ax1.set_ylabel("Counts", fontsize=12)
515.  self.ax1.set_xlabel("Wavelength (nm)", fontsize=12)
516.  x_wav = self.spec_waveL
517.  self.ax1.plot(x_wav, y_cnt, 'b-')
518.  self.ax1.text(0.1, 0.9,'Max at {}'.format(round(x_wav[np.argmax(y_cnt)],0)), transform=self.ax1.transAxes)
519.  plt.rcParams['xtick.top'] = True
520.  self.ax1.set_aspect(1.0/self.ax1.get_data_ratio()*self.plot_ratio)
521.  self.PLNo_image.draw()
522.
523.  def make_heatplot(self, data, fileNameStr, dtype): ## Triggered at the End
524.  plt.figure(figsize=[4,3])
525.  if dtype == "gray":
526.  plt.ylabel("Grayscale percentage")
527.  plt.yticks(np.linspace(0,255,8),np.around(np.linspace(0,100,8),decimals=0))
528.  plt.title("Change on Grayscale")
529.  elif dtype == "hue":
530.  plt.ylabel("Hue scale")
531.  plt.yticks(np.linspace(0,180,8),["Orange", "Yellow", "Green", "Turquoise", "Blue", "Purple", "Pink", "Red"])
532.  plt.title("Change on Hue")
533.  else:
534.  plt.ylabel("Wavelength (nm)")
535.  waveLen = len(self.spec_waveL)
536.  PLmin = np.min(self.spec_waveL)
537.  PLmax = np.max(self.spec_waveL)
538.  plt.yticks(np.linspace(0,waveLen,8),np.around(np.linspace(PLmin,PLmax,8),decimals=0))
539.  plt.title("PL spectra")
540.  plt.xlabel("Time(seconds)")
541.  plt.xticks(np.linspace(0,len(data.columns),8),np.around(np.linspace(0, max(data.columns), 8),decimals=2))
542.  plt.pcolor(data)
543.  plt.savefig(fileNameStr+"_heat_plot.png")#,bbox_inches = "tight")   # save the figure to file
544.  plt.close()    # close the figure window
545.
546.  def final_pressure_plot(self): ## Triggered at the End
547.  time = np.array(self.timeElapArray)
548.  pres = np.array(self.pressureArray)
549.  fast_i = 0
550.  long_i = 0
551.  offset = 2
552.  for i,p in enumerate(pres[offset:]):
553.  _, _, r_value, _, _ = stats.linregress(time[:i+offset],np.log(pres[:i+offset]))
554.  if r_value < -0.85:
555.  fast_i = i
556.  long_i=np.argmin(pres)
557.  slope, intercept, r_value, p_value, std_err = stats.linregress(time[:fast_i],np.log(pres[:fast_i]))
558.  line = np.exp(slope*time+intercept)
559.  fig = plt.figure(figsize=[4,3])
560.  ax = fig.add_subplot(1,1,1)
561.  ax.set_xlabel("Time(sec)")
562.  ax.set_ylabel("Pressure(mbar)")
563.  ax.semilogy(time,pres,"ro")
564.  ax.plot(time[:fast_i],line[:fast_i],"-g")
565.  ini_pres = pres[0]
566.  fast_rate = round((ini_pres-pres[fast_i])/time[fast_i],3)
567.  slow_rate = round((ini_pres-pres[long_i])/time[long_i],3)
568.  time_vacuum = round(time[long_i],2)
569.  mini_pres = round(pres[long_i],2)
570.  time_flux = round(time[-1]-time[long_i+offset],2)
571.  pres_flux = round(np.mean(pres[long_i+offset:-offset]),2)
572.  total_time = round(time[-1],2)
573.  ax.text(0.1, 0.7,"{:.2f} mbar/sec".format(fast_rate), transform=ax.transAxes)
574.  ax.text(0.15, 0.3,"{:.2f} mbar/sec".format(slow_rate), transform=ax.transAxes)
575.  ax.text(0.3, 0.1,"{:.2f} seconds".format(time_vacuum), transform=ax.transAxes)
576.  ax.text(0.3, 0.05,"{:.2f} mbar".format(mini_pres), transform=ax.transAxes)
577.  ax.text(0.6, 0.9,"{:.2f} seconds".format(time_flux), transform=ax.transAxes)
578.  ax.text(0.6, 0.95,"{:.2f} mbar".format(pres_flux), transform=ax.transAxes)
579.  fig.savefig(self.full_path+self.sample_name+"_Pressure_plot.png",bbox_inches = "tight")
580.  ## save to dictionary
581.  dict_names = ["PV_StartingPressure(mbar)","PV_FastVacuumRate(mbar/s)","PV_TotalVacumRate(mbar/s)",
582.  "PV_TimeUnderVacuum(s)", "PV_MinimumPressure(mbar)","PV_TimeUnderFlux(s)",
583.  "PV_FluxPressure(mbar)","PV_TotalTime(s)","PV_SlopeInterceptRvalue"]#,"PV_abc{a*exp(x*b)+d}"]
584.  dict_value = [ini_pres,fast_rate,slow_rate,
585.  time_vacuum, mini_pres, time_flux,
```

```
586.    pres_flux, total_time, [round(slope,4),round(intercept,4),round(r_value,4)]]#,*popt]
587.    for p,dns in enumerate(dict_names):
588.    self.xml_data[dns] = dict_value[p]
589.
590.    ## ~o~o~o~o~o~o~o~o~o Operational functions o~o~o~o~o~o~o~o~o~
591.    def solo_mode(self):
592.    time_step = 0.25
593.    delay = self.intVar_waitT.get()
594.    for cdwn in np.arange(delay,0,-time_step):
595.    self.elapsedVar.set("{:.2f} sec".format(cdwn))
596.    self.master.update_idletasks()
597.    time.sleep(time_step)
598.
599.    def startProcess(self):
600.    #Change button to "stop"
601.    print("Start: ",end="")
602.    self.stopButton.grid(row=5,column=0, columnspan=2)
603.    self.startButton.grid_forget()
604.    self.starTime = time.time()
605.    self.delay = float(self.intVar_waitT.get())
606.    self.startP = True
607.    print("1",end="")
608.    self.xml_data = xr.gather_data()
609.    print("2",end="")
610.    self.get_entry_metavalues()
611.    self.create_date_folder()
612.    self.create_sample_folder()
613.    print("3",end="")
614.    #Refreshes dataframes and arrays
615.    if self.isMic:
616.    self.microHue_df = pd.DataFrame()
617.    self.hueGray_df = pd.DataFrame()
618.    self.frame_counter = 0
619.    if self.isSpectro:
620.    self.PLspec_df = pd.DataFrame()
621.    # self.PLspec_df["Wavelength(nm)"] = self.spec_waveL
622.    if self.isPressure:
623.    self.Pressure_DF = pd.DataFrame()
624.    else:
625.    pyautogui.click(35,105)
626.    print("4",end="")
627.    self.timeElapArray =[]
628.    self.pressureArray=[]
629.    print("5",end="")
630.
631.    def stopProcess(self):
632.    #Change button to "start"
633.    self.stopButton.grid_forget()
634.    self.startButton.grid(row=5,column=0, columnspan=2)
635.    self.runningProcess = False
636.    self.list_measured_samples()
637.    ## Save data
638.    file_path = self.full_path+self.sample_name
639.    if self.isMic:
640.    self.microHue_df = self.microHue_df.astype("int64")
641.    self.hueGray_df = self.hueGray_df.astype("int64")
642.    self.microHue_df.to_csv(file_path+"_hue_data.csv",index=False)
643.    self.hueGray_df.to_csv(file_path+"_hueGrayscale_data.csv",index=False)
644.    self.fig_pls.savefig(file_path+"_hue_plot.png")
645.    # print(self.microHue_df)
646.    self.make_heatplot(self.microHue_df,file_path+"_hue","hue")
647.    self.make_heatplot(self.hueGray_df,file_path+"_gray","gray")
648.    if self.isPressure:
649.    self.Pressure_DF["time"]=self.timeElapArray
650.    self.Pressure_DF["pressure"]=self.pressureArray
651.    self.Pressure_DF.to_csv(file_path+"_pressure_data.csv",index=False)
652.    try:
653.    self.final_pressure_plot()
654.    except:
655.    pass
656.    if self.isSpectro:
657.    self.PLspec_df = self.PLspec_df.astype("float64")
658.    self.make_heatplot(self.PLspec_df,file_path+"_PL","PL")
659.    self.PLspec_df.insert(loc=0, column="Wavelength(nm)", value=self.spec_waveL)
660.    self.PLspec_df.to_csv(file_path+"_PL_data.csv",index=False)
661.    metad = pd.DataFrame.from_dict(self.xml_data, orient='index')
662.    metad.to_csv(file_path+"_metadata.csv")
663.    self.elapsedLabel.config(style ="bigST.TLabel")
664.
665.    def processes_loop(self):
666.    if self.startP:
667.    time_elapsed = round(time.time()-self.starTime,2)
668.    time_disp = self.delay-time_elapsed
669.    if time_disp > 0:
670.    # print(self.delay, round(time.time()-self.starTime,2))
671.    self.elapsedVar.set("{:.2f} sec".format(time_disp))
672.    self.master.update_idletasks()
673.    else:
674.    # print("out "+self.delay, round(time.time()-self.starTime,2))
675.    self.starTime = time.time()
676.    self.runningProcess = True
677.    self.startP = False
678.    else:
679.    pass
680.    if self.runningProcess:
681.    time_elapsed = round(time.time()-self.starTime,2)
682.    alt = 3 #Alert time to stop
683.    cdt = 3 #Cool down time
684.    total_time = self.intVar_totalT.get() + cdt
685.    #self.elapsedLabel.set(text=timeEl)
686.    self.timeElapArray.append(time_elapsed)
```

```
687.    if self.isMic:
688.    self.readSensor_Microscope(time_elapsed)###
689.    self.microHue_df[time_elapsed] = self.countsHue #from plotting spectra
690.    self.hueGray_df[time_elapsed] = self.countsGray
691.    if self.isPressure:
692.    self.readSensor_Pressure(time_elapsed)##
693.    if self.isSpectro:
694.    spec_counts = self.readSensor_Spectrometer()
695.    self.PLspec_df[time_elapsed] = spec_counts
696.    self.elapsedVar.set("{:.2f} sec".format(time_elapsed))
697.    if total_time-cdt-alt <time_elapsed:
698.    self.elapsedLabel.config(style ="redST.TLabel")
699.    if total_time-cdt < time_elapsed:
700.    self.elapsedLabel.config(style ="blueST.TLabel")
701.    if total_time < time_elapsed:
702.    self.stopProcess()
703.    self.master.update_idletasks()
704.    else:
705.    if self.isPressure:
706.    self.readSensor_Pressure(0)
```

7.8 Python GUI: Microscope Analysis of Layer Defects

This python code was used to take control of the substrate view of the printer LP50 and take pictures across the surface of a printed sample. Additionally, it analyses the pictures taken, marks the place where defects were found and creates a file that contains the number of defects per picture per sample.

```
from tkinter import *
from tkinter import ttk
from tkinter import messagebox
from tkinter import filedialog
import tkinter as tk
import numpy as np
import pandas as pd
from glob import glob
import matplotlib.pyplot as plt
from PIL import Image, ImageDraw
import pyautogui
import time
from datetime import date
import os
import shutil
import sys
import cv2

class defect_imaging:
def __init__(self, master):
master.title('Substrate defect imager')
windowWidth = master.winfo_reqwidth()
positionRight = int(master.winfo_screenwidth()/2 - windowWidth/2)
master.geometry("+{}+{}".format(positionRight, 0))
master.configure(background = '#FFFFFF')
self.style = ttk.Style()
self.style.configure('TFrame', background = '#FFFFFF')
self.style.configure('TButton', background = '#FFFFFF',font = ('Arial', 10))
self.style.configure('TLabel', background = '#FFFFFF', font = ('Arial', 10))
self.style.configure('TCheckbutton', background = '#FFFFFF', font = ('Arial', 10))
self.style.configure('TRadiobutton', background = '#FFFFFF', font = ('Arial', 10))
self.style.configure('Header.TLabel', font = ('Arial', 18, 'bold'))
self.samples_grid = [7,6]
## ~ ~ ~ ~ ~ ~ ~ ~ ~ ~ ~ ~ ~ ~ ~ Frame configurations ~ ~ ~ ~ ~ ~ ~ ~ ~ ~ ~ ~ ~ ~ ~ ~ ~ ~ ~
## - - - - - Substrates frame - - - - -
self.frame_substrates = ttk.Frame(master)
self.frame_substrates.grid(row=0,column=0)
ttk.Label(self.frame_substrates,background = '#d3d3d3',text = "prefix").grid(row = 0, column = 0,columnspan=2)
self.prefix = tk.StringVar()
self.pre_entry = ttk.Entry(self.frame_substrates, width = 8,background = '#d3d3d3',textvariable=self.prefix)
self.pre_entry.grid(row = 0, column = 1,columnspan=2)
tk.Label(self.frame_substrates, fg="red",bg='#FFFFFF' ,text = ".",font = ("Arial", 16, "bold")
).grid(row=self.samples_grid[1], column=self.samples_grid[0]-2, columnspan=2, sticky="wes")
tk.Label(self.frame_substrates, fg="red",bg='#FFFFFF' ,text = u"\u2190",font = ("Arial", 12, "bold")
).grid(row = self.samples_grid[1]-1, column = self.samples_grid[0]-2, rowspan=2, sticky="swen")
position = []
for i in range(self.samples_grid[1],0,-1):
for j in range(self.samples_grid[0]-1,-1,-1):
position.append([i,j])
self.stringVars = []
self.entries = []
for s,pos in enumerate(position):
stringVar = tk.StringVar()
self.stringVars.append(StringVar)
entry = ttk.Entry(self.frame_substrates, width = 5, font = ('Arial', 10),textvariable=stringVar)
entry.grid(row = pos[0],column = pos[1], padx = 3, pady = 3)
self.entries.append(entry)

## - - - - - Configuration frame - - - - -
self.frame_configuration = ttk.Frame(master)
self.frame_configuration.grid(row=0,column=1, padx = 5)
ttk.Label(self.frame_configuration, text = 'Substrate size (mm):').grid(row = 0, column = 0, padx = 5, sticky = 'nw')
ttk.Label(self.frame_configuration, text = 'Active area (mm):').grid(row = 1, column = 0, padx = 5, sticky = 'nw')
ttk.Label(self.frame_configuration, text = 'Pictures per side:').grid(row = 2, column = 0, padx = 5, sticky = 'nw')
ttk.Label(self.frame_configuration, text = 'Starting Position:').grid(row = 3, column = 0, padx = 5, sticky = 'nw')
self.var_size = tk.DoubleVar()
self.var_area = tk.DoubleVar()
self.var_grid = tk.IntVar()
self.var_radio = IntVar()
self.var_xpos = tk.DoubleVar()
self.var_ypos = tk.DoubleVar()
self.entry_size = ttk.Entry(self.frame_configuration, text=self.var_size, width = 14, justify='center')
```

```
        self.entry_area = ttk.Entry(self.frame_configuration, text=self.var_area, width = 14, justify='center')
        self.entry_grid = ttk.Entry(self.frame_configuration, text=self.var_grid, width = 14, justify='center')
        self.entry_xpos = ttk.Entry(self.frame_configuration, text=self.var_xpos, width = 7, justify='center')
        self.entry_ypos = ttk.Entry(self.frame_configuration, text=self.var_ypos, width = 7, justify='center')
        self.radio_coax = ttk.Radiobutton(self.frame_configuration, text="Coax Light", variable=self.var_radio, value=1)#, command=sel)
        self.radio_ring = ttk.Radiobutton(self.frame_configuration, text="Ring Light", variable=self.var_radio, value=0)#, command=sel)
        self.var_size.set(25.4)
        self.var_area.set(15.0)
        self.var_grid.set(5)
        self.var_radio.set(1)
        self.var_xpos.set(261.253)
        self.var_ypos.set(13.740)
        self.entry_size.grid(row = 0, column = 1, padx = 5, sticky="w")
        self.entry_area.grid(row = 1, column = 1, padx = 5, sticky="w")
        self.entry_grid.grid(row = 2, column = 1, padx = 5, sticky="w")
        self.entry_xpos.grid(row = 3, column = 1, sticky="w")
        self.entry_ypos.grid(row = 3, column = 1, sticky="e")
        self.radio_coax.grid(row = 4, column = 0, padx = 5,columnspan=2)
        self.radio_ring.grid(row = 5, column = 0, padx = 5,columnspan=2)
        self.var_folder = tk.StringVar()
        today_date = date.today().strftime("%Y%m%d")
        self.folder_path = 'C:\\Users\\LP50\\Seafile\\IJPrinting_Edgar-Florian\\'+today_date+"\\"
        self.var_folder.set(self.folder_path)
        self.folderEntry = ttk.Entry(self.frame_configuration, text=self.var_folder, width = 30)
        self.folderButton = ttk.Button(self.frame_configuration, text = "...",width = 3,
                                       command=self.browseButton).grid(row=6,column=0, sticky="w")
        self.folderEntry.grid(row=6,column=0, columnspan=2, sticky="e")
        self.startButton = ttk.Button(self.frame_configuration, text = "Start",width = 10,
                                      command=self.start_process).grid(row=8,column=0,columnspan=2, sticky="nesw")

    def browseButton(self):
        try:
            self.folder_path = filedialog.askdirectory(initialdir=self.folderEntry.get())+"\\"
        except:
            self.folder_path = filedialog.askdirectory()+"\\"
        self.var_folder.set(self.folder_path)

    def check_for_duplicates(self, sample_names):
        ''' Check if given list contains any duplicates '''
        if len(sample_names) == len(set(sample_names)):
            dupes = 0
            return False, dupes
        else:
            dupes = [x for n, x in enumerate(sample_names) if x in sample_names[:n]]
            return True, dupes

    def start_process(self):
        self.subs_size = float(self.entry_size.get())
        self.active_area = float(self.entry_area.get())
        self.grid_num = int(self.entry_grid.get())
        self.samp_prefix = self.pre_entry.get()
        self.position_zero =[float(self.entry_xpos.get()),float(self.entry_ypos.get())]
        print(self.position_zero)
        image_wanted = []
        image_names = []
        for s, stV in enumerate(self.entries):
            if stV.get() != "":
                image_wanted.append(True)
                image_names.append(self.pre_entry.get()+stV.get())
            else:
                image_wanted.append(False)
        duplicated, dup_samps = self.check_for_duplicates(image_names)
        if duplicated:
            messagebox.showerror("Duplicated samples found",
                                 "Samples %s are duplicated\nPlease check again."%(dup_samps))#, bg='#FFFF00' )
        else:
            messagebox.showinfo("Camera Overlay", "Make sure overlay is off (!!)")

            sample_positions = self.sample_grid(image_wanted)

            for s,sp in enumerate(sample_positions):
                steps = self.camera_positions(sp)
                self.mouse_clicker(steps)
                # print(image_names[s],steps)

                images_list = self.getPictures()
                self.relocate_image(images_list, image_names[s])
                print("Sample %s is completed"%(image_names[s]))

    def sample_grid(self, wanted):
        sample_positions = []
        counter = 0
        for j in list(range(self.samples_grid[1])):
            for i in list(range(self.samples_grid[0])):
                if wanted[counter]:
                    sample_positions.append(
                        [round(self.position_zero[0]-i*self.subs_size,3),
                         round(self.position_zero[1]+j*self.subs_size,3)])
                else:
                    pass
                counter += 1
        return sample_positions

    def camera_positions(self, poss):
        x_pos, y_pos = poss
        steps = self.calculate_positions()
        for st in steps:
            st[0] = round(st[0]+x_pos+(self.subs_size-self.active_area)/2,3)
            st[1] = round(st[1]+y_pos+(self.subs_size-self.active_area)/2,3)
        return steps
```

```
    def calculate_positions(self):
        grid_steps = self.grid_num
        step_size = self.active_area/grid_steps
        start_spot = step_size/2
        step_positions = []
        for i in list(range(grid_steps)):
            for j in list(range(grid_steps)):
                step_positions.append([start_spot+i*step_size, start_spot+j*step_size])
        return step_positions

    def mouse_clicker(self, steps):
        ## If problems, move mouse to screen's top-left corner to cancel process
        pyautogui.FAILSAFE= True
        starTime = time.time()
        ## Click on "Printview Tab"
        pyautogui.click(510,950)
        ## Click on "Move Tab"
        pyautogui.click(60,650)
        ## Press "Initialize" button
        for i, sp in enumerate(steps):
            x_pos= sp[0]
            y_pos= sp[1]
            ## Click on "X axis" Field
            pyautogui.click(200,800)
            pyautogui.sleep(0.025)
            ## Write "X position"
            pyautogui.write(str(round(x_pos+185.377,3)))#185.377 is a default offset
            pyautogui.press("enter")
            ## Click on "Y axis" Field
            pyautogui.click(280,800)
            pyautogui.sleep(0.025)
            ## Write "Y position"
            pyautogui.write(str(round(306.679-y_pos,3)))#306.679 is a default offset
            pyautogui.press("enter")
            if i == 0:
                ## Click on "Go To"
                pyautogui.click(65,800)
                pyautogui.sleep(1)
            else:
                ## Click on "Go To"
                pyautogui.click(65,800)
                pyautogui.sleep(0.3)
            ## press "Take picture" button
            pyautogui.click(705,760)
            pyautogui.sleep(0.025)
        ## This is to make it easy to change to a new sample
        ## Click on "Y axis" Field
        print("This took "+str(round(time.time()-starTime,2))+" seconds")

    def getPictures(self):
        numImages = self.grid_num
        totalImages = numImages**2
        folderPath = "C:\\LP50\\"
        fileArr = glob(folderPath+'ScreenCaptures\\'+"PVCapt*.png")
        fileArr.sort(key=os.path.getmtime, reverse=True)
        fileArr = np.asarray(fileArr).astype(np.str_)[:totalImages]
        return fileArr

    def relocate_image(self, imagesList, sample_name):
        if not os.path.exists(self.folder_path+sample_name):
            os.mkdir(self.folder_path+sample_name)
            print(self.folder_path+sample_name+" has been created")
        if self.var_radio.get() == 1:
            defects_path = self.folder_path+sample_name+"\\images_defect_coax\\"
        elif self.var_radio.get() == 0:
            defects_path = self.folder_path+sample_name+"\\images_defect_ring\\"
        else:
            defects_path = self.folder_path+sample_name+"\\images_defect_err\\"
        try:
            os.mkdir(defects_path)
        except:
            pass
        for i,source in enumerate(imagesList[::-1]):
            destination = defects_path+sample_name+"_"+str(i)+".png"
            # shutil.copy(source, destination)
            shutil.move(source, destination)

    ## ~ ~ ~ ~ ~ ~ ~ ~ ~ ~ ~ ~ ~ ~ ~ Anaylsis part  ~ ~ ~ ~ ~ ~ ~ ~ ~ ~ ~ ~ ~ ~ ~ ~ ~ ~
    def open_images(defPath, steps):
        total_i = steps**2
        images_list = sorted(set(glob(defPath+"*.png"))-set(glob(defPath+"*Defects.png")),key=os.path.getmtime)
        img_array = []
        for file in images_list:
            img = cv2.imread(file,1)
            ## resizing of the image, necessary bc not all pictures are the same size (apparently)
            cr = 0
            y, x, _ = img.shape
            img_array.append(img[1:y-cr,1:x-cr])
        return img_array

    def count_defects_coax(images_array, deftype):
        number_contours = []
        average_area = []
        imgContours = []
        ## Open background image to flatten irregular lighting
        bkgd_path = glob(".\\blanks\\background1.png")[0]
        bkgd_img = cv2.imread(bkgd_path,1)
        bkgd = cv2.cvtColor(bkgd_img, cv2.COLOR_RGB2GRAY)
        for i,img in list(enumerate(images_array)):
            ## Open image and set to grayscal
            gray = cv2.cvtColor(img, cv2.COLOR_RGB2GRAY)
```

```
            xsize = gray.shape[1]
            ysize = gray.shape[0]
            ## set to light or dark defects
            if deftype == "light":
                divl = np.array(bkgd[:ysize,:xsize]/gray)
                divl = np.array(divl*255/np.max(divl), dtype=np.uint8)
                thresh = cv2.adaptiveThreshold(divl, 255, cv2.ADAPTIVE_THRESH_GAUSSIAN_C, cv2.THRESH_BINARY_INV, 501, 30)
                # ret,thresh = cv2.threshold(div,50,255,cv2.THRESH_BINARY)
            else:
                divd = np.array(gray/bkgd[:ysize,:xsize])
                divd = np.array(divd*255/np.max(divd), dtype=np.uint8)
                thresh = cv2.adaptiveThreshold(divd, 255, cv2.ADAPTIVE_THRESH_GAUSSIAN_C, cv2.THRESH_BINARY_INV, 201, 40)
                # ret,thresh = cv2.threshold(div,70,255,cv2.THRESH_BINARY_INV)
            ## Find contours/defects on images
            _, contours_list,_ = cv2.findContours(thresh, cv2.RETR_TREE, cv2.CHAIN_APPROX_SIMPLE)
            ## Measure the area of the defects
            area = []
            contours = []
            for cont in contours_list:
                if cv2.contourArea(cont) > 1:# and cv2.contourArea(cont) < 9000:
                    area.append(cv2.contourArea(cont))
                    contours.append(cont)
                else:
                    continue
            ## Color defects depending if light or dark
            if deftype == "light":
                col = (0,255,255)#in yellow
            else:
                col = (255,0,255)#in magenta
            ## Saves contours, and later will be added to a copy of the picture
            imgContours.append(cv2.drawContours(img, contours,-1,col,1))
            if area[:]:
                lenC = len(contours)
                meanV = np.mean(area)
                stdvV = np.std(area)
            else:
                lenC = 0
                meanV = 0
                stdvV = 0
            # print("%i- %i \tdefects with area %.2f+-%.2f"%(i+1,lenC,meanV,stdvV))
            number_contours.append(lenC)
            if  meanV > 5000:
                average_area.append(0)
            else:
                average_area.append(round(meanV,1))
        return number_contours, average_area, imgContours

    def count_defects_ring(images_array):
        number_contours = []
        average_area = []
        imgContours = []
        for i,img in list(enumerate(images_array)):
            ## Open image and set to grayscal
            gray = cv2.cvtColor(img, cv2.COLOR_RGB2GRAY)
            ret,thresh = cv2.threshold(gray,40,255,cv2.THRESH_BINARY)
            ## Find contours/defects on images
            _, contours_list,_ = cv2.findContours(thresh, cv2.RETR_TREE, cv2.CHAIN_APPROX_SIMPLE)
            ## Measure the area of the defects
            area = []
            contours = []
            for cont in contours_list:
                if cv2.contourArea(cont) > 1:# and cv2.contourArea(cont) < 9000:
                    area.append(cv2.contourArea(cont))
                    contours.append(cont)
                else:
                    continue
            ## Color defects depending if light or dark
            col = (0,255,255)#in yellow
            ## Saves contours, and later will be added to a copy of the picture
            imgContours.append(cv2.drawContours(img, contours,-1,col,1))
            if area[:]:
                lenC = len(contours)
                meanV = np.mean(area)
                stdvV = np.std(area)
            else:
                lenC = 0
                meanV = 0
                stdvV = 0
            # print("%i- %i \tdefects with area %.2f+-%.2f"%(i+1,lenC,meanV,stdvV))
            number_contours.append(lenC)
            if  meanV > 5000:
                average_area.append(0)
            else:
                average_area.append(round(meanV,1))
        return number_contours, average_area, imgContours

    def save_contour_image(steps, images, path, sample):
        total_i = steps**2
        for i in list(range(total_i)):
            cv2.imwrite(path+sample+"_"+str(i)+"_wDefects.png", images[i])

                    ## This makes bubble plots
    def image_defects(grid_steps, defs, sample_name, def_path):#defs,fPath,sName):
        if isinstance(defs[0],float):
            typeG = "area"
        else:
            typeG = "counts"
        ## This sets the folder where plot will be saved (one level up)
        def_path = os.path.dirname(os.path.dirname(def_path))
        ## Make a matrix  with the number of places where pictures were taken
        def_matrix = np.zeros([grid_steps,grid_steps])
```

```
            plt.cla()
            ## Make coordinates for the bubble positions
            cell_posit = []
            for i in range(grid_steps):
                for j in range(grid_steps):
                    cell_posit.append((i,j))
            ## Place bubbles on the right coordinate
            for i,d in list(enumerate(cell_posit)):
                def_matrix[d] = defs[i]
                plt.scatter(cell_posit[i][0]+0.5,cell_posit[i][1]+0.5,s=defs[i]/max(defs)*1700, color="c")  ## 1700 to normalize the maximum bubble radius to one square
                plt.text(cell_posit[i][0]+0.5,cell_posit[i][1]+0.5,defs[i],fontsize=8, horizontalalignment='center',
                         verticalalignment='center')
            ## Configuration of plot
            plt.xlim(0, grid_steps)
            plt.ylim(0, grid_steps)
            plt.grid()
            plt.xticks(list(range(grid_steps)),[])
            plt.yticks(list(range(grid_steps)),[])
            plt.gca().set_aspect('equal', adjustable='box')
            plt.xlabel(sample_name+": "+typeG)
            if self.var_radio.get()==1:
                plt.savefig(f"{def_path}\\{sample_name}_defects_coax_bubble_{typeG}",dpi=300,bbox_inches='tight',pad_inches=0)
            else:
                plt.savefig(f"{def_path}\\{sample_name}_defects_ring_bubble_{typeG}",dpi=300,bbox_inches='tight',pad_inches=0)
            plt.close()

        def defects_boxplot(sample_name, data,def_path):
            if isinstance(data[0],float):
                typeG = "area"
            else:
                typeG = "counts"
            def_path = os.path.dirname(os.path.dirname(def_path))
            figBP, axBP = plt.subplots()
            axBP.set_title(sample_name+": "+typeG)
            axBP.boxplot(data)
            try:
                meanV = round(np.mean(data),2)
            except:
                meanV = 0
            plt.text(0.2,0.9,"Mean value = "+str(meanV),fontsize=10,ha='center', va='center', transform=axBP.transAxes)
            if self.var_radio.get()==1:
                plt.savefig(f"{def_path}\\{sample_name}_defects_coax_boxPlot_{typeG}",dpi=300)
            else:
                plt.savefig(f"{def_path}\\{sample_name}_defects_ring_boxPlot_{typeG}",dpi=300)
            plt.close()

        def boxplot_all(names, data, path):
            if isinstance(data[1][0],float):
                typeG = "area"
            else:
                typeG = "counts"
            figaP, axaP = plt.subplots()
            axaP.set_title(f"All samples: {typeG}")
            #Setting y-axis to log leads to outliers
            log_data = []
            for d in data:
                log_data.append(np.ma.log10(d).filled(0)) #np. masked&filled with 0
            axaP.boxplot(log_data)
            axaP.set_yticks(np.arange(0, 5))
            axaP.set_yticklabels(10.0**np.arange(0, 5))
            axaP.set_xticklabels(names)
            axaP.grid(axis="y", linestyle="--")
            plt.xticks(rotation=90)
            if self.var_radio.get()==1:
                plt.savefig(f"{path}\\all_defects_coax_boxPlot_{typeG}",dpi=300)
            else:
                plt.savefig(f"{path}\\all_defects_ring_boxPlot_{typeG}",dpi=300)
            plt.close()

        def save_to_csv_file(samp_name,relocPath,contours_comb,area_comb):
            def_dict = {"Defects_contour" : contours_comb, "Defects_area" : area_comb}
            results = pd.DataFrame.from_dict(def_dict, orient='index')
            if self.var_radio.get()==1:
                results.to_csv(relocPath+samp_name+"_defects_results_coax.csv",header=False)
            else:
                results.to_csv(relocPath+samp_name+"_defects_results_ring.csv",header=False)

        def build_composed_image(path, files):
            img_obj = []
            for f in files:
                img_obj.append(Image.open(f))
            xsize, ysize = img_obj[0].size
            i_size = xsize*1//3
            sp = 1 #spacing between images
            coords = (i_size, ysize//2-i_size//2, 2*i_size-sp , (ysize//2)+(i_size//2)-sp)
            cropp_img = []
            for c in img_obj:
                cropp_img.append(c.crop(coords))
            grid = int(np.sqrt(len(files)))
            composed_image = Image.new('RGB', (i_size*grid, i_size*grid))   #Creates a new/blank image
            positions = []
            for m in list(range(grid)):
                for n in list(range(grid))[::-1]:
                    positions.append((m*i_size, n*i_size))
            #Stitch cropped images together
            for c, ci in enumerate(cropp_img):
                composed_image.paste(ci, positions[c])
            sample_name = path.rsplit('\\',2)[-2]
            end_path = path
            ##Add text with sample name
            font = ImageFont.truetype("arial.ttf", 20)
```

```
475.            ImageDraw.Draw(composed_image).text((0,0),sample_name,(0,0,0),font=font)
476.            #Save image to same folder where original is located
477.            composed_image.save(end_path+sample_name+"_defects_composed.png")
478.
479.    def main():
480.        root = Tk()
481.        feedback = defect_imaging(root)
482.        root.mainloop()
483.
484.    if __name__ == "__main__": main()
```

7.9 AHK Code to Clean Printhead Nozzles

This AHK code was used to automate the cleaning of the nozzles of a Spectra SE printhead on an LP50 printer. Additionally, it creates a sequence where all the nozzles become visible, to see the number of working nozzles.

```
;This loop periodically purges the printhead (useful for unclogging)
;   For unclogging, it is helpful to increase the printhead temperature and reduce the
;   pressure, so a thin layer of warm solvent is present on the nozzles
^u::
noloops = 60
breaking = False
Coordmode, Mouse, Screen
        ;This part sets up the GUI window
        Gui, +AlwaysOnTop
                gui, font, s8, Verdana  ; Set 10-point Verdana.
                Gui, Add, Text, vMyText, This process is designed for the LP50
                Gui, Add, Button, default, Stop
                Gui, Show, x200 y0, LP50:  Automatic running process
        Loop, %noloops% {
                FormatTime, TimeString, , dd.MM. HH:mm:ss
                if breaking = True
                        Reload
                guicontrol, , myText, Flushing: %A_Index%/%noloops%
                ;Go to Controls Tab
                MouseClick, Left, 370, 950
                Sleep, 25
                ;Go to Maintenance Tab
                MouseClick, Left, 230, 120
                Sleep, 25
                ;Press Purge
                MouseClick, Left, 340, 545
                Sleep, 25
                ;Go to Dropview Tab
                MouseClick, Left, 650, 950
                Sleep, 1000*60*2
                }
        return



;This command reloads the code
^r::reload


; This loop allows a quick look to all nozzles
f3::
        Coordmode, Mouse, Screen
        ;Go to DropView Tab
        MouseClick, Left, 640, 950
        Sleep, 50
        Loop, 43    {
                nozzle := (A_Index*3)-1
                ;Choose nozzle
                MouseClick, Left, 440, 810
                Sleep, 50
                Send %nozzle% {Enter}
                Sleep, 100
                ;Choose go to nozzle
                MouseClick, Left, 305, 805
                Sleep, 1500
```

8 List of Publications

The following publications were produced during this doctorate:

- E.R. Nandayapa, K. Hirselandt, C. Boeffel, E.L. Unger, E.J.W. List-Kratochvil, Unraveling Reversible Quenching Processes of O 2, N2, Ar, and H2O in Metal Halide Perovskites at Moderate Photon Flux Densities, Adv. Opt. Mater. (2020) 2001317. https://doi.org/10.1002/adom.202001317.

- B. Wenger, H.J. Snaith, I.H. Sörensen, J. Ripperger, S. Kazim, S. Ahmad, E.R. Nandayapa, C. Boeffel, S. Colodrero, M. Anaya, S.D. Stranks, I. Mora-Seró, T.C.-J. Yang, M. Bräuninger, T. Rissom, T. Aernouts, M. Hadjipanayi, V. Paraskeva, G.E. Georghiou, A.B. Walker, A. Walter, S. Nicolay, Towards unification of perovskite stability and photovoltaic performance assessment, ArXiv. (2020) 1–9. http://arxiv.org/abs/2004.11590.